A MECHANISTIC MODEL OF ENVIRONMENTAL OXYGEN INFLUENCE ON THE DETERMINISTIC EFFECTS TO HUMAN SKIN FROM SPACE RADIATIONS

A Dissertation

by

JOHN FLORES-MCLAUGHLIN

Submitted to the Office of Graduate and Professional Studies of
Texas A&M University
in partial fulfillment of the requirements for the degree of

DOCTOR OF PHILOSOPHY

Chair of Committee,	Leslie A. Braby
Co-Chair of Committee,	John R. Ford
Committee Members,	Steven Riechman
	John W. Poston Sr.
Head of Department,	Yassin A. Hassan

May 2016

Major Subject: Nuclear Engineering

ABSTRACT

During human spaceflight missions, controlled variation of atmospheric pressure and oxygen concentration from a sea-level based normal to hyperoxic levels may occur as part of operational procedure. This activity is of interest because it provides the relevant radiation exposure and dynamic oxygen concentration parameters that may lead to varying radiation sensitivity in the skin and other organs.

Tumor hypoxia has been indicated as a primary factor in the decrease in efficacy of radiation therapy. These oxygen concentration effects have been largely demonstrated with low-LET radiations and to a lesser degree with high-LET primary radiations such as protons and heavy ions common in space exposure.

In order to analyze the variation of oxygen concentration in human skin from spaceflight activities, a mathematical model of oxygen transport through the human cardiorespiratory system with pulmonary and cutaneous intake was implemented. Oxygen concentration was simulated at the various skin layers, from dermis to epidermis. Skin surface radiation doses and spectra from relatively high flux Solar Particle Events (SPEs) were calculated by the PHITS radiation transport code over a range of spacecraft and spacesuit thicknesses in terms of aluminum equivalence. A series of anatomical skin and shielding thicknesses were chosen to encompass the scope of radiation exposure levels as indicated by existing NASA skin phantom studies.

To model the influence of oxygen with radiation exposure, microdosimetric oxygen fixation simulations were implemented using the Monte-Carlo-Damage-Simulation (MCDS) code. From these outputs, occurrence of DNA double strand breaks

(DSBs) and relative biological effect (RBE) from radiation exposure with oxygen concentration dependence was established and correlated to spaceflight activities.

It was determined that minimal but observable oxygen concentration transients occur in skin during environmental oxygen changes in spaceflight. The most significant transients occurred in the thickest epidermal layers with relatively high amounts of diffusion. Accordingly, these thickest epidermal layers also showed the greatest spaceflight induced transients of RBE relative to sea-level based atmosphere exposures.

DEDICATION

This dissertation is dedicated to my wife Ruth and my three children Kaylee, Damian and Amara for their continuous support during my graduate program.

ACKNOWLEDGEMENTS

I would like to thank the National Science Foundation's Bridge to Doctorate Program and the Texas A&M LSAMP program for their financial support early in my graduate career.

I would also like to thank the National Space Biomedical Research Institute's Space Life Sciences program for introducing me to space radiation subject matter.

Finally, I would like to thank my advisory committee and Dr. Stephen Guetersloh for their patience, guidance and knowledge.

TABLE OF CONTENTS

LIST OF FIGURES

LIST OF TABLES

1. INTRODUCTION

1.1 Overview

Continuous and relatively high exposure from energetic ions to spaceflight participants outside the earth's atmosphere is a notable concern during human spaceflight. In addition, operational logistics of this radiation exposure vary with spacecraft shielding materials, thickness and variable atmospheric mediums. This activity is of interest because it provides the relevant radiation exposure and dynamic oxygen concentration parameters that may lead to varying radiation sensitivity in the skin and other organs.

Exposures that could potentially lead to acute or deterministic biological effects are commonly associated with Solar Particles Events (SPEs). Due to the potential of significant deterministic effects from exposure to these particles, planning and countermeasures to mitigate this exposure are a necessary component of spaceflight planning.

The dependence on shielding thickness and material type is well documented as a significant factor in net exposure from SPEs (Lin et al., 2012; Zeitlin, Guetersloh, Heilbronn, & Miller, 2005; Zeitlin, Heilbronn, Miller, & Shavers, 2001). Shielding can modify particle energy spectra thus modifying the absorbed dose, energy distributions, quality factor or other derived weighting factors of these radiations. Factors that may modify these results are of great interest in the effort to optimize spacecraft and habitat design.

Prevailing human spaceflight procedures utilize variation in atmospheric content and pressure for various work functions and individual comfort, including a wide variation of oxygen content. During extravehicular activity (EVA), which requires pressures considerably below one atmosphere, procedures require the change of the oxygen content from the Earth-based normal of 21% to near 100% in order to combat decompression sickness (Thomas, 2006). In addition, hyperbaric exposures have been indicated for treatment of decompression sickness (DCS) or air embolism caused from spaceflight activities (Huntoon, 1996).

In an attempt to simulate these attributes of the spaceflight environment, an anthropomorphic model of the human skin with defined oxygen tension was created based on gas transport and diffusion. In order to simulate oxygen-dependent changes in RBE in this model, the Monte-Carlo-Damage-Simulation (MCDS) (Carlson, Stewart, Semenenko, & Sandison, 2008; Stewart et al., 2011) code, which is validated against cell death and chromosome aberration studies was utilized. This served as a radiation target for simulations with the PHITS radiation transport software. From these simulations transients in Relative Biological Effect (RBE) from SPEs were assessed.

1.2 Description of the Space Radiation Environment

The radiation field that astronauts are exposed to in space is complex compared to that of ground-based radiation workers. It contains photons, electrons, protons, alpha particles, and heavier ions up to very high energies with origins outside our solar system.

The sun emits high fluxes of mostly protons, with some heavy ions and electrons. These radiations may subsequently become trapped in belts by the magnetic field of the Earth and/or cause secondary radiations including neutrons created by interactions with materials of the spacecraft. Ionizing radiation doses to astronauts in space are on the order of 1-3 mSv per day and depending on the time spent in space they may exceed 100 mSv total. It is common occurrence for astronaut exposures to exceed annual (50 mSv) and lifetime dose limits for ground-based radiation workers proposed by the International Commission of Radiation Protection (ICRP).

Galactic Cosmic Radiation (GCR) ion spectra with origins from supernovae and other astronomical events are the most continuously prevalent ionizing radiation exposures. Within the solar system GCR radiation is modulated by radiation and magnetic fields originating from the sun. Within Low Earth Orbit (LEO), the Earth's magnetic field traps low energy protons and electrons resulting in relatively high exposures when spacecraft cross the field lines associated with South Atlantic Anomaly (SAA) and field lines near the magnetic poles. Beyond the protection of earth's magnetic field and physical shielding, higher exposure rates of GCR are possible in addition to the potential of increased exposure from solar radiation. Figure 1 provides an outline of the space radiation spectrum.

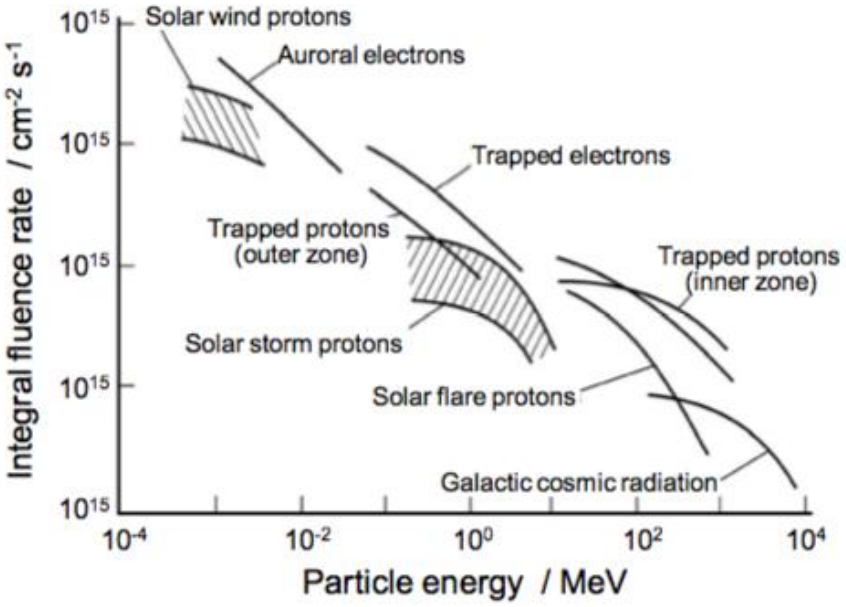

Figure 1. Spectral summary of space radiations (J. W. Wilson, 1978)

The sun continuously emits particle radiation consisting primarily of protons and electrons, the solar wind. This radiation is orders of magnitude lower in kinetic energy (< 3.5 keV) relative to other galactic radiations and may be shielded by micrometers of aluminum or similar shielding. However, occasionally the shock associated with a coronal mass ejection (CME) or the energy released at a solar flare site may accelerate these particles to MeV or GeV energies and they may be classified as Solar Energetic Particles (SEPs). If these energetic particles reach Earth or a location of interest they may be classified as a Solar Particle Event (SPE), this is alternatively called a Solar Proton Event indicating the primary abundance of protons in the particle composition. The National Oceanic and Atmospheric Administration's (NOAA) Space Environment Center (SEC) declares an SPE to be in progress when the exposure rate of particles with

energies above 10 MeV (i.e., space-suit-penetrating) exceeds 10 particles / cm2-sec-ster (directional flux) for more than 15 minutes ("Radiation and the International Space Station: Recommendations to Reduce Risk," 2000).

Unlike GCR, SEPs originate from the Sun and are difficult to predict in intensity and occurrence. In addition, for exposure to occur the accelerated particles must interact with the solar magnetic field lines in a manner to target Earth or an object of interest. The result of this transport across magnetic field lines and primarily Coulombic scattering results in a mostly isotropic particle exposure at 1 AU distance for sizes comparable to a spacecraft. For larger geometries directionality moving away from the solar origin may be established (Dorman & Venkatesan, 1993).

1.3 Variation of the Atmospheric Environment for Human Spaceflight

Variation of atmospheric pressure and content has been a continually evolving aspect of spaceflight. Early U.S. manned space vehicles encompassing both Mercury and Gemini programs atmospheric pressures were planned at 5 psi with 100% oxygen concentration. Nitrogen use was avoided since it brought the risk of decompression sickness and additional weight in design. However, during preliminary tests in the Apollo 1 spacecraft an accidental fire occurred that resulted in the death of three astronauts: Edward White, Gus Grissom and Roger Chaffee. Similarly, On January 28, 1986 the Soviet Union disclosed that cosmonaut Valentin Bondarenko died after a fire in a high-oxygen isolation chamber on March 23, 1961, less than three weeks before the

first Vostok manned space flight. These fires were found to be largely promoted from the high abundance of oxygen and changes to U.S. spacecraft design were made to reduce the risk of fire including decreasing oxygen concentration to 60%. Although the new cabin atmosphere was significantly safer than 100% oxygen, it still contained almost three times the amount of oxygen present in ordinary sea level air (20.9% oxygen). This relatively high content of oxygen was necessary to ensure that the partial pressure of oxygen was maintained at 3 psi. (60% of 5 psi is 3 psi, comparable to 20.9% of 14.7 psi, or 3.07 psi in sea-level air)(Vasquez, Pretorius, & Rimkus, 1987)

These specifications again came under scrutiny under the Apollo-Soyuz Test Project (ASTP). The atmospheric pressure and composition inside the Apollo command module differed from that used inside the Russian Soyuz spacecraft. The Soyuz uses 80 % nitrogen 20 % oxygen environment at a pressure of one full atmosphere (14.7 psi). Transfer between these two atmospheres would require pre-breathing of pure oxygen to purge the blood of dissolved nitrogen. This was avoided by lowering the Soyuz pressure to two-thirds atmospheric pressure. The docking module served mainly as an airlock to raise or lower the pressure between 1/3 (Apollo) and 2/3 atmospheres when moving from one spacecraft to the other. Subsequent U.S. spacecraft have utilized a normal atmospheric environment of 1 atm or14.7 psi with 21% oxygen (Thomas, 2006).

Due to the difficulty in dexterity in pressurized spacesuits both U.S. and Russian programs have traditionally utilized pressures lower than 1 atm for EVA. The U.S. Space Shuttle, Soyuz and the International Space Station (ISS) operate at 1 atm of pressure. Therefore, it is prudent that a pre-breathing procedure to acclimate crewmembers to

lower pressured space suits and to avoid decompression sickness. To perform an EVA from the U.S. Space Shuttle, the cabin pressure was reduced from 14.7 psi to 10.2 psi for approximately 24 hours. In anticipation of further reduced pressure, the crewmembers then pre-breathed pure oxygen for 45 minutes prior to initiating the EVA. For EVAs initiated from the ISS, crewmembers usually begin the pre-breathe protocol by exercising for 10 minutes on a specially designed treadmill for spaceflight while breathing pure oxygen via a mask. After nearly an hour of breathing pure oxygen, the crewmembers will move to the airlock where pressure is lowered to 10.2 psi as similarly done on the shuttle. During depressurization, the crewmembers will breathe pure oxygen for an additional 30 minutes. Afterwards, with the airlock now at 10.2 psi the crewmembers will put on their space suits. With their spacesuits on, the crewmembers will breathe pure oxygen inside the suits for an additional 60 minutes before making final preparations to begin their EVA. This results in a total of 2 hours and 20 minutes of pure oxygen breathing, including the 10 minutes of exercise at the beginning of the procedure. Gradually this time has been extended to 4 hours to reduce risk of complications (RD Vann). Publicly available data to view this process is available from the Environmental and Thermal Operating (ETHOS) display from the ISS (Figure 2).

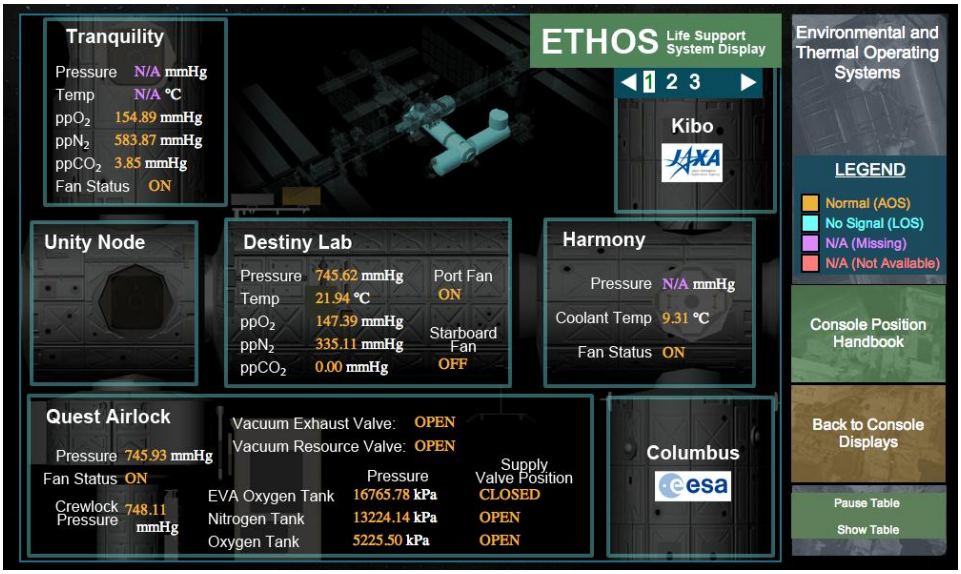

Figure 2. International Space Station ETHOS life support system display (http://spacestationlive.nasa.gov/displays/ethosDisplay1.html).

1.4 Evidence for the Biological Significance of Oxygen Variation

To produce observable deterministic effects to the skin such as erythema, when exposure occurs at earth normal atmospheric pressure and oxygen concentration, doses above 2 Gy are necessary. These radiation exposures during spaceflight are possible from Solar Particle Events (SPEs), which can produce doses that are substantially higher within a period of days (Figure 3). SPEs occur often, and it is difficult to predict their onset, duration and magnitude. Most SPEs result in insignificant crew doses even for light spacecraft or even EVA shielding, and only a small proportion (about 10%) of events lead to significant organ doses of >10 mGy-Eq. There is data to indicate five Earth-bound SPEs where dose and energy spectra exceeded deterministic effect thresholds (1956, 1960, 1972, 1989 x2) (Kim, De Angelis, & Cucinotta, 2011).

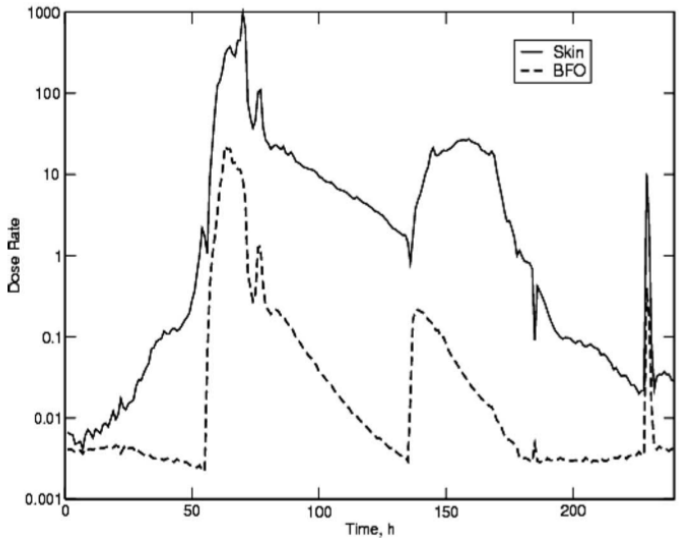

Figure 3. Dose rate (cGy/Hr) from the August 72´SPE with 0.3 gm/cm^2 shielding. Total Skin Dose = 32.15 Gy (S. Hu, Kim, McClellan, & Cucinotta, 2009)

Direct evidence of increased radiosensitivity to the skin in human patients from increased diatomic oxygen pressure has been found (Gray, Conger, Ebert, Hornsey, & Scott, 1953; van den Brenk, Kerr, Richter, & Papworth, 1965). The radiation sensitivity of normal and malignant cells in anoxic condition to low LET radiation varies by factors of 2.5–3 as pO_2 is increased from <1 mmHg (.02 psi) to 25 mmHg (.48 psi) (Hall, 2006). Hypoxia is a common feature of many tumors and a reduction of effectiveness of radiation therapy, which is overcome by increased radiation dosage and/or combination of hyperbaric treatment, oxygen supplementation and/or pharmaceuticals. In addition, erythema has been observed in proton radiotherapy with hypothetical severity apparently determined by oxygen tension (Whaley et al., 2013) (Figure 4.).

Figure 4. Radiotherapy patient exposed to perpendicular proton radiation. The lesser effected center was covered by gas impermeable polyurethane film and acrylate film for the entire exposure duration of 6 weeks (Whaley et al., 2013). It is hypothesized the lesser-effected center resulted from a hypoxic tension.

Clinically observed deterministic effects from charged particle radiation require doses above a threshold. To produce observable deterministic effects to the skin, a minimum of 1-2 Gy is required. Deterministic dose limits from these radiations exist in the form of 30 day and 1 year limits that are imposed to US spaceflight participants to protect the skin, lens, and blood forming organs (ICRP, 2010) from the occurrence of acute health effects such as skin ulceration, moist and dry desquamation, erythema, cataracts, inflammatory tissue responses, gastro-intestinal illness and central nervous system detriment. These doses are unlikely to be exceeded in LEO, but during Lunar-type and Martian-type long duration missions it is possible that these may be exceeded if protections are not in place, most notably from SPEs.

In medical x-ray procedures, deterministic skin injury is usually the result of exceeding exposure thresholds referenced in ICRP 85 (ICRP, 2010) , NCRP 168 (NCRP, 2011) or FDA Guidelines (FDA, 1994) and verified by follow up monitoring of the exposed skin area. The appearance of initial deterministic injury varies between

exposures and individuals resulting in the need for continuous monitoring following a qualifying exposure (Koenig, Mettler, & Wagner, 2001). Deterministic injury most often presents itself as erythema at absorbed skin surface doses above 2 Gy and substantially higher doses can result in the appearance of epilation, ulceration and necrosis (Table 1).

Threshold Skin Entrance Doses for Different Skin Injuries		
Single-Dose Effect	Threshold (Gy)	Onset
Early transient erythema	2	Hours
Main erythema	6	Approximately 10 days
Late erythema	15	Approximately 6–10 wks
Temporary epilation	3	Approximately 3 wks
Permanent epilation	7	Approximately 3 wks
Dry desquamation	14	Approximately 4 wks
Moist desquamation	18	Approximately 4 wks
Secondary ulceration	24	Greater than 6 wks
Ischemic dermal necrosis	18	Greater than 10 wks
Dermal atrophy (1st phase)	10	Greater than 14 wks
Dermal atrophy (2nd phase)	10	Greater than 1 yr
Induration (invasive fibrosis)	10	Unknown
Telangiectasia	10	Greater than 1 yr
Late dermal necrosis	> 12	Greater than 1 yr
Skin cancer	Stochastic	Greater than 5 yrs

Table 1. Dose thresholds for respective skin deterministic effects (Hirshfeld et al., 2004)

2. SIMULATION METHODS

2.1 Outline

A range of radiations and atmospheric exposures are possible during spaceflight. Much of this variation is attributed to operational logistics, such as compression, decompression and change in radiation shielding due to mission activities. In order to determine if oxygen variation and differing incident radiation spectra will change the resultant skin damage, these attributes were identified and applied in an integrative model. A visual representation of the model is presented in Figure 5.

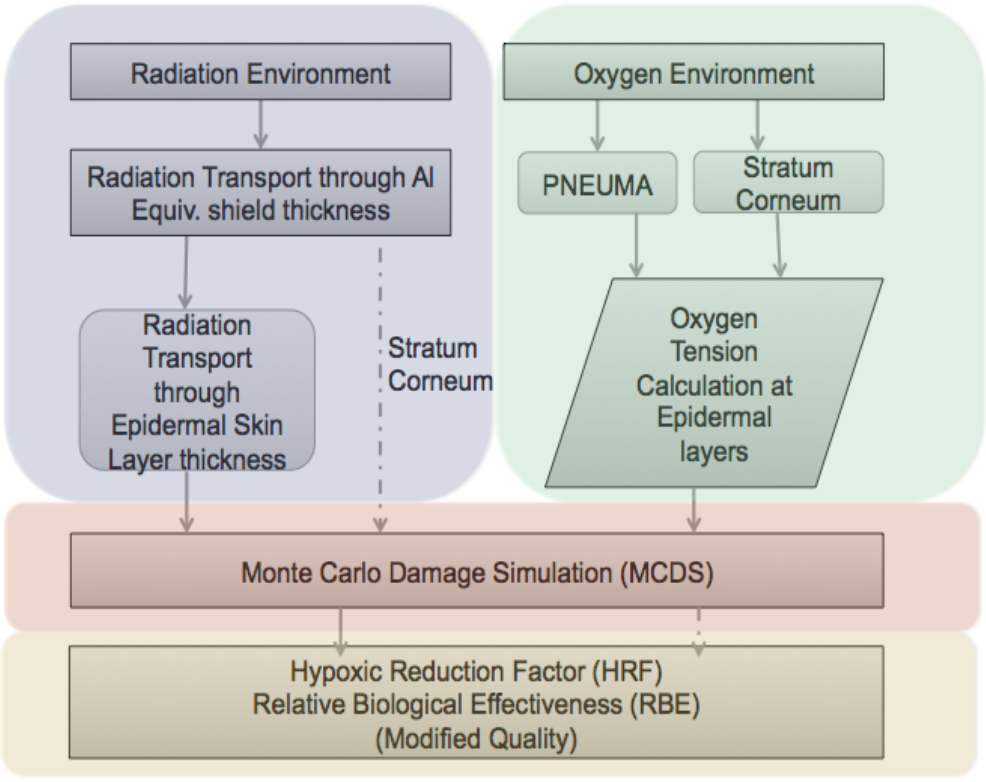

Figure 5. Outline of simulation procedure

As presented in the figure, radiation and oxygen environments were simulated separately and then combined to determine net radiation detriment. In an attempt to simulate deterministic skin attributes in the spaceflight environment, an anthropomorphic model of the human skin with defined oxygen tension was created based on selected gas transport and diffusion models. Oxygen transport is simulated *in vivo* through a cardiorespiratory model called PNEUMA (Hsing-Hua & Khoo, 2002) with oxygen tension boundary conditions found in literature (Wang, Winlove, & Michel, 2003). External oxygen transport was simulated by Fick's diffusion approximations as validated in literature (Stucker et al., 2001).

In order to simulate oxygen-dependent change in RBE in this model, the Monte-Carlo-Damage-Simulation (MCDS) code (Carlson et al., 2008; Stewart et al., 2011) was utilized. MCDS is verified against cell death and chromosome aberration, an indicator of erythema incidence (Peter, 2005). This served as a radiation target for simulations with the PHITS radiation transport software (T. Sato et al., 2013). Variation in radiation shielding encompassing the range of spacecraft operations was utilized in the radiation transport code. From these simulations, optimal modification to oxygen breathing profile and/or operational considerations in order to reduce net deterministic effect from SPEs was assessed.

2.2 Estimation of Incident Solar Particle Spectra

Relatively high-energy particles arrive at Earth orbit first during a SPE and are followed by particles of lower energies. As a result the energy distribution of SPE particles observed at Earth depends on time after onset of the event. The vast majority of these particles are protons, but modern instrumentation has validated the presence of helium, oxygen and iron at orders of magnitude lesser flux. From incident high-energy particles, many target fragments have short ranges, on the order of hundreds of microns or less in water or tissue. Early particle detectors on satellites and spacecraft had limited energy resolution capability. Not until Solar Cycle 23 did new instrumentation make it possible to measure the composition and energy spectra of SEP events over a broad energy interval (<0.1 to >100 MeV/nuc), including all abundant elements from H to Fe (Mewaldt, 2007).

Initially to overcome limitations in data resolution, Malitson and Weber (Malitson & Webber, 1963) suggested an exponential fit to describe the energy spectrum of an SPE based on two integrated flux data points. Using these fits the energy spectrum was often inaccurate and shown to be erroneous at higher energies. A different fitting method using the Weibull function was applied by Xapsos (Xapsos et al., 2000) using the Marquardt–Levenberg nonlinear regression routine. However, subsequent studies (Atwell, Tylka, Dietrich, Badavi, & Rojdev, 2011) have found high variation in individual SPE spectrum. An alternative fitting method called the band function is a combination of two integral power law fits. Multiple studies (Tylka & Dietrich, 2008)

(Atwell, Tylka, Dietrich, & Badavi, 2008) have applied the band function across several SPE spectra with nominal results. Alternatively, Mewaldt (2005, 2007) has found, with the increased data resolution provided in Solar Cycle 23 and new Advanced Composition Explorer (ACE) satellites a direct single or double power law fit is applicable to describe the broad range of SPE spectra.

Accordingly, using the method prescribed by Mewaldt (2005) for energies above 10 MeV, SPE particle spectra may be approximated by a single power law:

$$\frac{d\phi(E)}{dE} = A_o \times E^x \qquad \text{Equation 1}$$

After the onset of the event, the exponent x decreases with time and the contribution by high-energy particles to absorbed dose decreases with time during the event. The constant A_o describes the absolute number of particles and is highly influenced by field irregularities or shock waveforms in the interplanetary medium.

The more-complex double power law may be used to describe broader energy range of SPE spectra. This is primarily useful in examining data when lower energy ranges are available. The spectral indices for the high and low energy particles are notably different within each event with strong time dependency. In its simplest form, a double power law spectrum takes the form:

$$\frac{d\phi(E)}{dE} = A_o \times E^{X_1} \quad [\, E \leq Ec \,] \qquad \text{Equation 2}$$

$$\frac{d\phi(E)}{dE} = B_o \times E^{X_2} \quad [\, E > Ec \,] \qquad \text{Equation 3}$$

Additional respective constants B_o and X_2 are applied to the energy range separated by energy cutoff E_c. Exposure to fluxes above 10 MeV can be transported through limited shielding, such as a spacesuit and induce adverse skin reactions or damage the lens and cornea of the eye. Situations where these lower energies are attenuated may be satisfactorily simulated using a single power law. A sample of power law indices is provided in Figure 6.

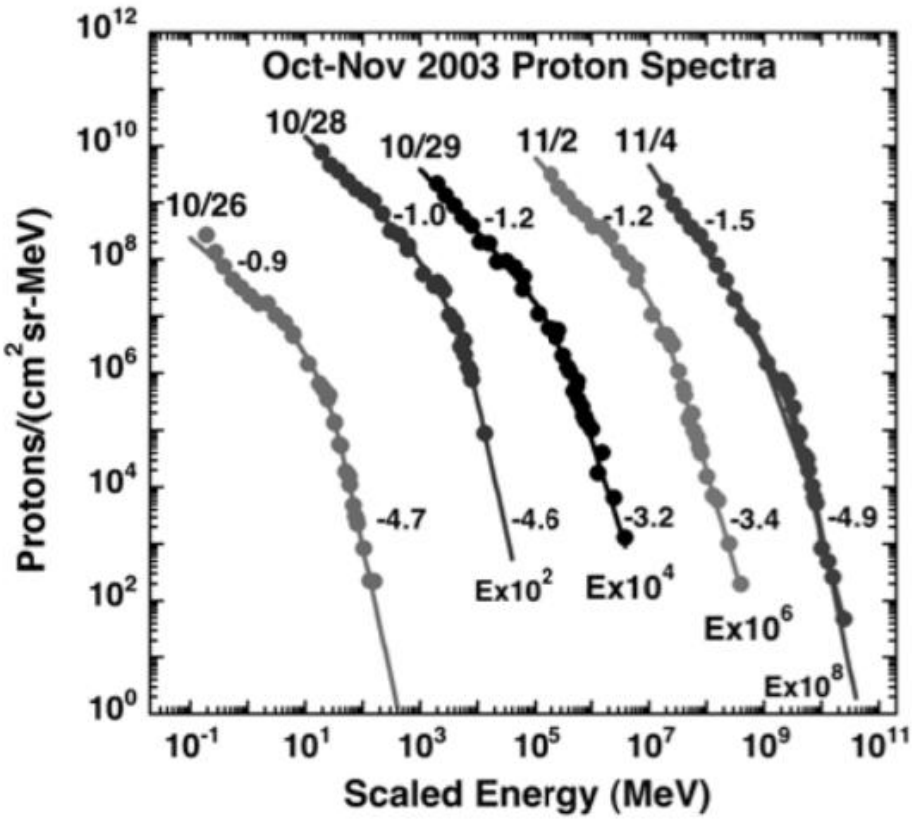

Figure 6. Proton spectra for five events in October / November 2003. Both power law indices are listed (Mewaldt, 2005).

Given the lack of broad justification for a single broad fitting method, differential source spectra from published data sets were utilized directly. The following SPE events, indicative of potential deterministic effects, were simulated based on the data sets shown in Table 2. Graphical representations of these data sets may be found in Appendix A.

SPE Event Date	Data Sources	Integral Fit
February 1956	NASA Langley (Wilson) (J. W. Wilson, 1976)	Piecewise Exponential ϕ=2.52E9 /cm^2
	Webber (Webber, 1963)	Piecewise Power and Exponential ϕ=1E10 /cm^2
November 1960	NASA Langley (Wilson) (J. W. Wilson, 1976)	Piecewise Exponential ϕ=1.8E10 /cm^2
August 1972	NASA Langley (Wilson) (J. W. Wilson, 1976)	Exponential ϕ =1.76E10 /cm^2
	King (King, 1974)	Exponential in Rigidity ϕ =2.33E10 /cm^2
October 1989	NASA Langley (Sauer) (Sauer, 1990)	Double Power Law ϕ =5.21E10 /cm^2
September 1989	NASA Langley (Sauer) (Sauer, 1990)	Double Power Law ϕ =1.41E10 /cm^2

Table 2. Summary of SPE data sources

2.3 Radiation Transport and Incident Radiation to Skin

Incident radiation upon human skin can vary substantially in spaceflight as on Earth, depending on source and shielding. Radiation exposure to skin in NASA radiation skin studies (Kim, George, & Cucinotta, 2006) (S. Hu et al., 2009) during long duration missions is expected to be the most relevant for deterministic effect due to the lack of physical and magnetic shielding from Earth. Typical SPE incident spectra was simulated using proton nuclei for the significance to deterministic effect as indicated by previous

studies(Heinbockel, Slaba, Blattnig, & Tripathi, 2010) (S. Hu et al., 2009; Kim et al., 2011). Additionally, relative particle fluence from other ions is several orders of lesser magnitude (Mewaldt, 2005) (Figure 7).

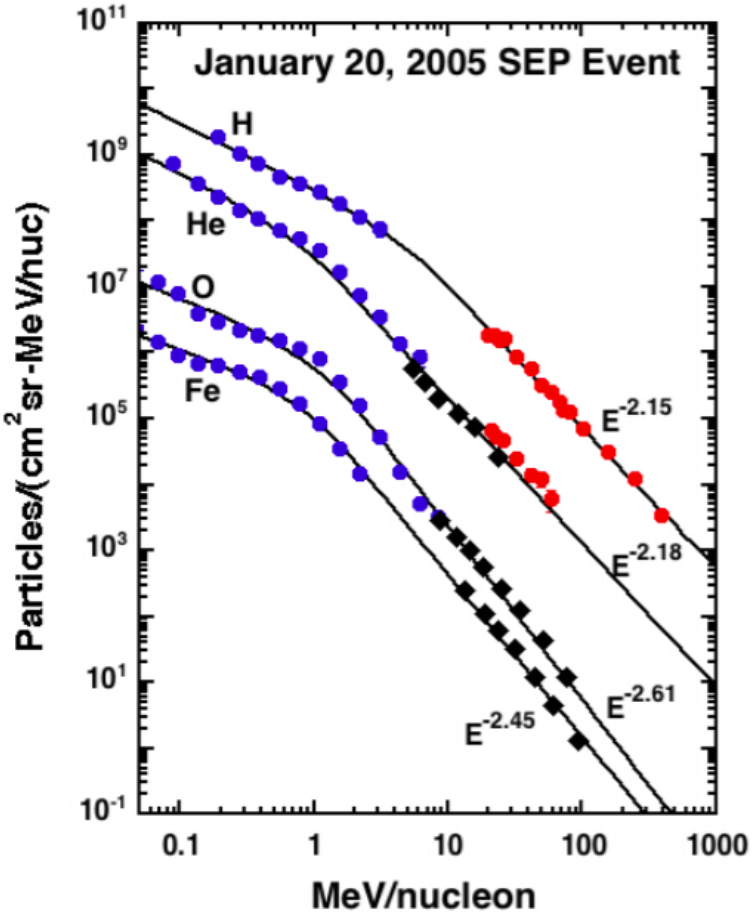

Figure 7. Ion spectra for an SPE in January of 2005. Both power law indices are listed (Mewaldt, 2005).

The Particle and Heavy Ion Transport code System (PHITS) is a Monte Carlo-based radiation transport code, developed by the Japan Atomic Energy Institute (JAERI). PHITS radiation transport software has been chosen for use in this model due to

previous validation in space radiation studies (T. Sato & Niita, 2006; Sihver, Sato, Puchalska, & Reitz, 2010), familiar Monte Carlo N-Particle (MCNP)-like interface and highly customizable end data products. A variety of existing libraries and modules create a single transport code with applicability to a wide range of energies, forms of radiation, and target materials. Figure 8 presents the constituent modules that constitute the full PHITS radiation transport software as well as its structure and applicability.

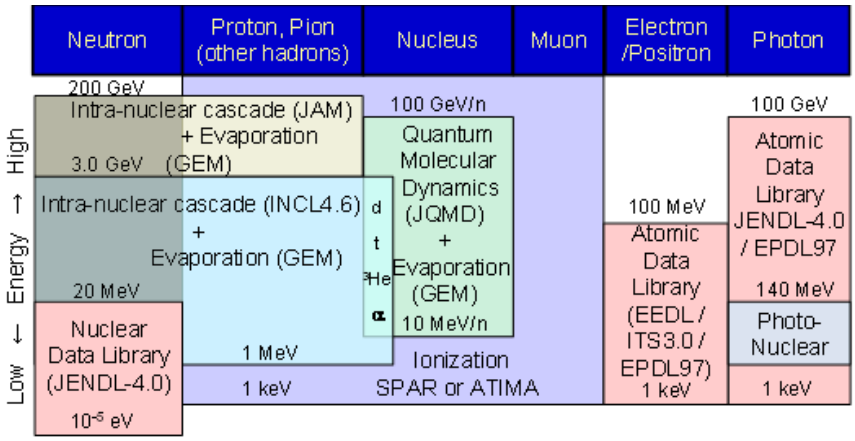

Figure 8. Outline of the PHITS radiation transport code. Image obtained from the PHITS website (http://phits.jaea.go.jp/image/OvMapOfModels.png)

Numerous comparisons of PHITS with other ion transport codes have been published for relevant space environment and proton interaction problems (Aghara, Sriprisan, Singleterry, & Sato, 2015; Lin et al., 2012; Oh & Lee, 2011; Sihver et al., 2008). PHITS results correlate well for both dose equivalent and neutron generation results (Figure 9 and Figure 10) obtained with MCNP and FLUtuierende KAskade (FLUKA) codes. Neutrons are a particularly notable contributor to dose from SPEs but

lack complete attribution for energies less than 100 MeV in the NASA developed High *Z* and Energy TRaNsport (HZETRN) code (Aghara et al., 2015).

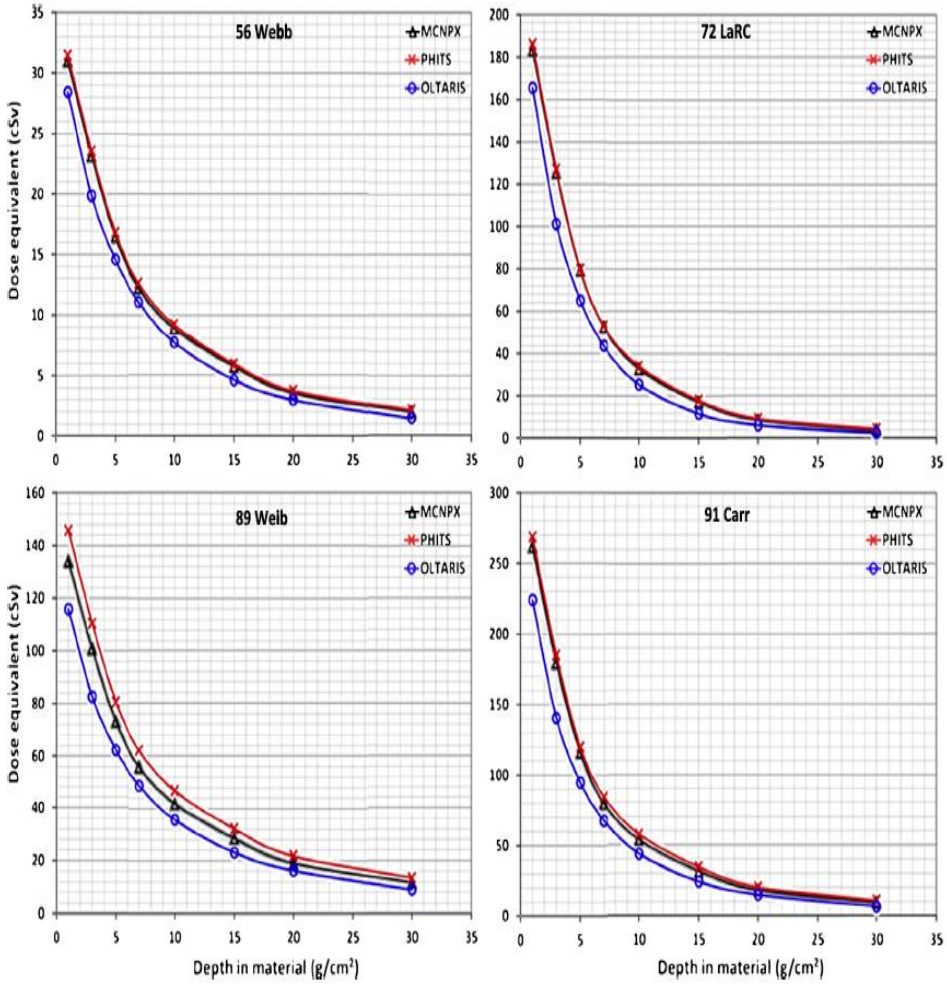

Figure 9. Dose Equivalent calculated by. PHITS, OLTARIS (HZETRN) and MCNPX at various depths of water after 20 gm/cm^2 of aluminum for four (1956, 1972, 1989 and 1859 Carrington) SPE events (Aghara et al., 2015).

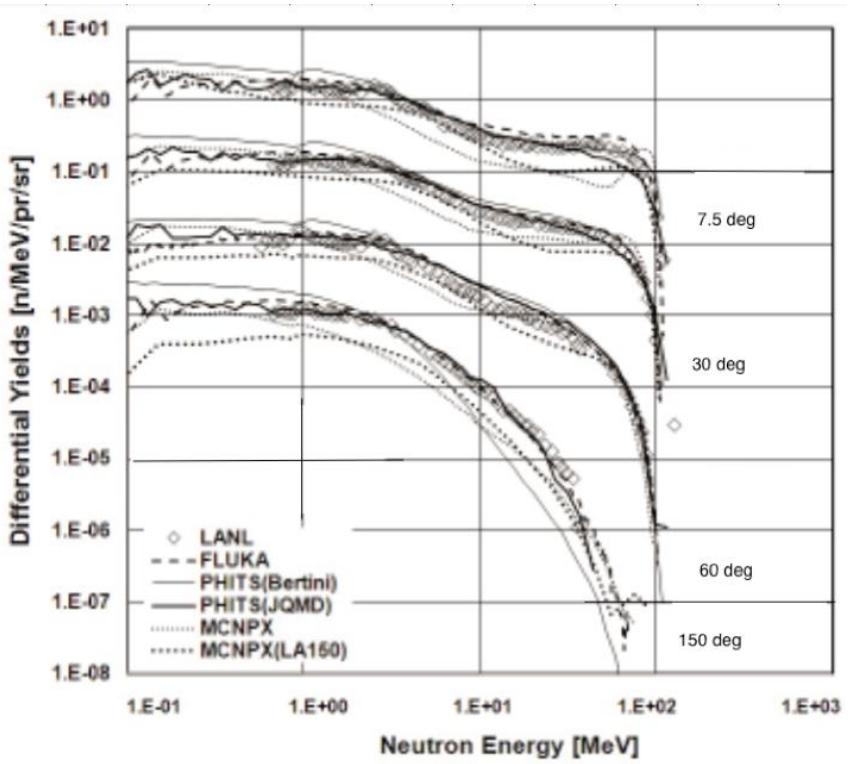

Figure 10. Comparison between FLUKA, PHITS and MCNPX calculated and measured (LANL) differential neutron yield as a function of incident angle from a 4.6 cm aluminum target bombarded by 113 MeV incident protons (Oh & Lee, 2011).

The Extravehicular Mobility Suit (EMU) manufactured for NASA by ILC Dover, is the current design of US EVA suit used aboard the ISS. The Orlan (Eagle) -M suit, produced by NPP Zvezda, is the current Russian EVA suit and had been previously used aboard the Mir Orbital Station. The U.S. EMU suit consists of several layers including a polyurethane-coated nylon pressure layer, a polyester structural restraint layer, and a woven Kevlar®, Teflon®, and Dacron® anti-abrasion outer layer (Thomas, 2006). An estimated translation of this suits thickness to an equivalent Aluminum range based on previous studies (Benton, Benton, & Frank, 2001; Zeitlin et al., 2001) will be applied in this PHITS simulation. The aluminum thicknesses of 0.1 cm (.27 gm/cm2), 1 cm (2.7

gm/cm2), 5cm (13.5 gm/cm2) and 13.5 cm (36.45 gm/cm2) will be used to encompass a range of potential EVA and intravehicle shielding. Particle fluence inclusive of delta ray and fragmentation contributions and the dose corresponding to depth in the skin layers illustrated in Figure 11. will be tallied and applied to the MCDS model.

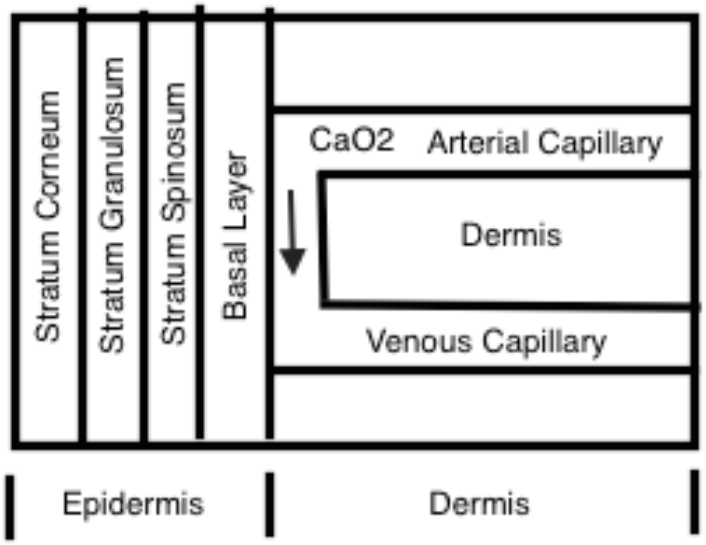

Figure 11. Epidermal components to be simulated. Representation of arterial blood flow and boundary condition for oxygen diffusion in dermal and epidermal layers.

2.4 Atmospheric Oxygen Transport to the Human Skin

The mode of oxygen uptake to human tissue is generally considered to be via the lung and through the vascular system, but cutaneous uptake through the epithelium has been observed to significantly influence oxygen concentration in the skin (Stucker et al., 2001). Oxygen supply of the epidermal and dermal layers is a balance between oxygen transport by the blood and uptake from the atmosphere. The epidermis is avascular or contains no blood vessels and is nourished almost exclusively by diffused oxygen from the surrounding air, however cells in the deeper layers are nourished by diffusion from blood capillaries extending to the upper layers of the dermis. The epidermis is composed of about 95% keratinocytes but also contains melanocytes, Langerhans cells, Merkel cells and inflammatory cells. Although not a direct indicator of inflammation, keratinocytes can modulate the immune system including providing cytokine stimulus of cutaneous inflammation via Langerhans cell activation via Interleukin-1 beta (IL-1β) secretion or Tumor Necrosis Factor alpha (TNFα) (Banno, Gazel, & Blumenberg, 2004). This is a notable endpoint due to the strong atmospheric influence and variability of epidermal oxygen tension.

Cutaneous diffusion of oxygen occurs at varying levels in different locations. Oxygen diffusion in human anatomy is at highest rates through the eyelids (.10 mm) (necessary for the cornea, which does not have a oxygen providing blood supply) and lowest through the thickest palms and soles (1.5 mm). These skin thicknesses were detailed as the target of the radiation transport model.

The common medical assumption is that inspired atmospheric oxygen (P_IO_2) is saturated with water vapor at body temperature is applied (Patm - 47 mmHg), resulting in an inspired oxygen pressure (P_IO_2) of around 150 mmHg. Inspired oxygen diffuses through the alveolar wall in the lungs then becomes bound to hemoglobin in addition to dissolving into plasma. Numerous factors determine the value of alveolar pressure of oxygen and carbon dioxide: pressure of the outside air (P_{atm}), partial pressures of inspired oxygen (P_IO_2) and carbon dioxide (P_ICO_2), rate of oxygen consumption, carbon dioxide production, and the rates of alveolar gas exchange. The average alveolar partial pressures for O_2 (P_AO_2) and CO_2 (P_ACO_2) are about 100 mmHg (2.03 psi) and 40 mmHg (.77 psi), respectively. Equilibrium is readily met for CO_2 between alveolar and arterial interfaces and therefore arterial CO2 (P_aCO_2) may be considered 40 mmHg as well.

For dry air at sea level, the partial pressures for oxygen (PO_2) and carbon dioxide (PCO_2) are about 160 mmHg (3.09 psi) and 0.3 mmHg (.006 psi), respectively. The alveolar O_2 partial pressure (P_AO_2) is not routinely measured but may be calculated from blood and gas measurements (such as pulse oximetry) using the standard alveolar gas equation (Equation 4).

$$P_AO_2 = P_IO_2 - {}^{P_ACO_2}/_{RQ} + F \qquad \text{Equation 4}$$

where R is the Respiratory Quotient (normally about 0.8 and approaching 1 for an all glucose diet), P_AO_2 is the alveolar partial pressure of O_2, P_IO_2 is the inspired partial

pressure of O_2, P_ACO_2 is the alveolar partial pressure of CO_2 and F is the correction factor (usually less than 2 mmHg (.04 psi)).

At the alveoli-arterial interface, the partial pressure of oxygen is relatively high, and oxygen binds readily to hemoglobin that is present. As the blood circulates to other body tissues where the partial pressure of oxygen is lower, oxygen is released into the tissue due to the lower concentration of oxygen present from metabolic consumption. In spaceflight, the most significant factor influencing oxygen-hemoglobin binding is atmospheric carbon dioxide, which varies depending on spaceflight activities and filtering specifications. Carbon dioxide decreases the amount of oxygen that is available for binding for a given pO_2. There is an additional environmental consideration due to temperature, but this is considered minimal compared to carbon dioxide influence (Fournier, 2007).

The contribution of oxygen-hemoglobin binding is best illustrated by the oxygen-hemoglobin saturation curve (Figure 12). The oxygen-hemoglobin saturation curve relates oxygen saturation (SO_2) and partial pressure of oxygen in the blood (pO_2).

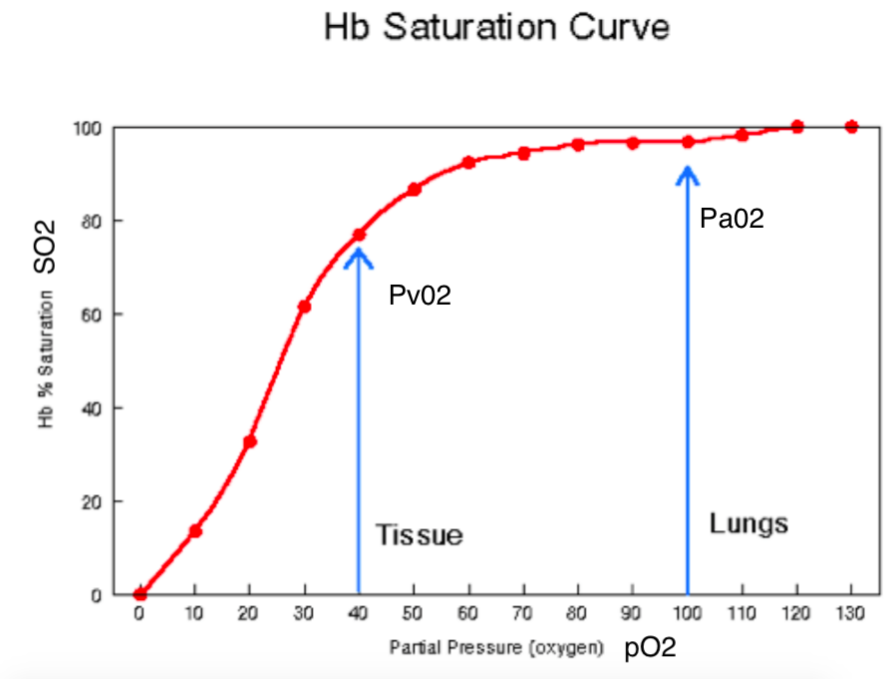

Figure 12. Oxyhemoglobin saturation curve. Image obtained from Austin Community College (http://www.austincc.edu/emeyerth/hbsat.gif).

Utilizing the alveolar gas equation as an input for lung respiration, the oxygen tension boundary condition found in literature (Wang et al., 2003) and a comprehensive cardiorespiratory model, PNEUMA (Hsing-Hua & Khoo, 2002), oxygen tension was simulated across a range of epidermal thickness. The chosen respiratory model depicts numerous breathing cycles, inclusive of the rapid transients of spaceflight operations. The model is depicted in Figure 13.

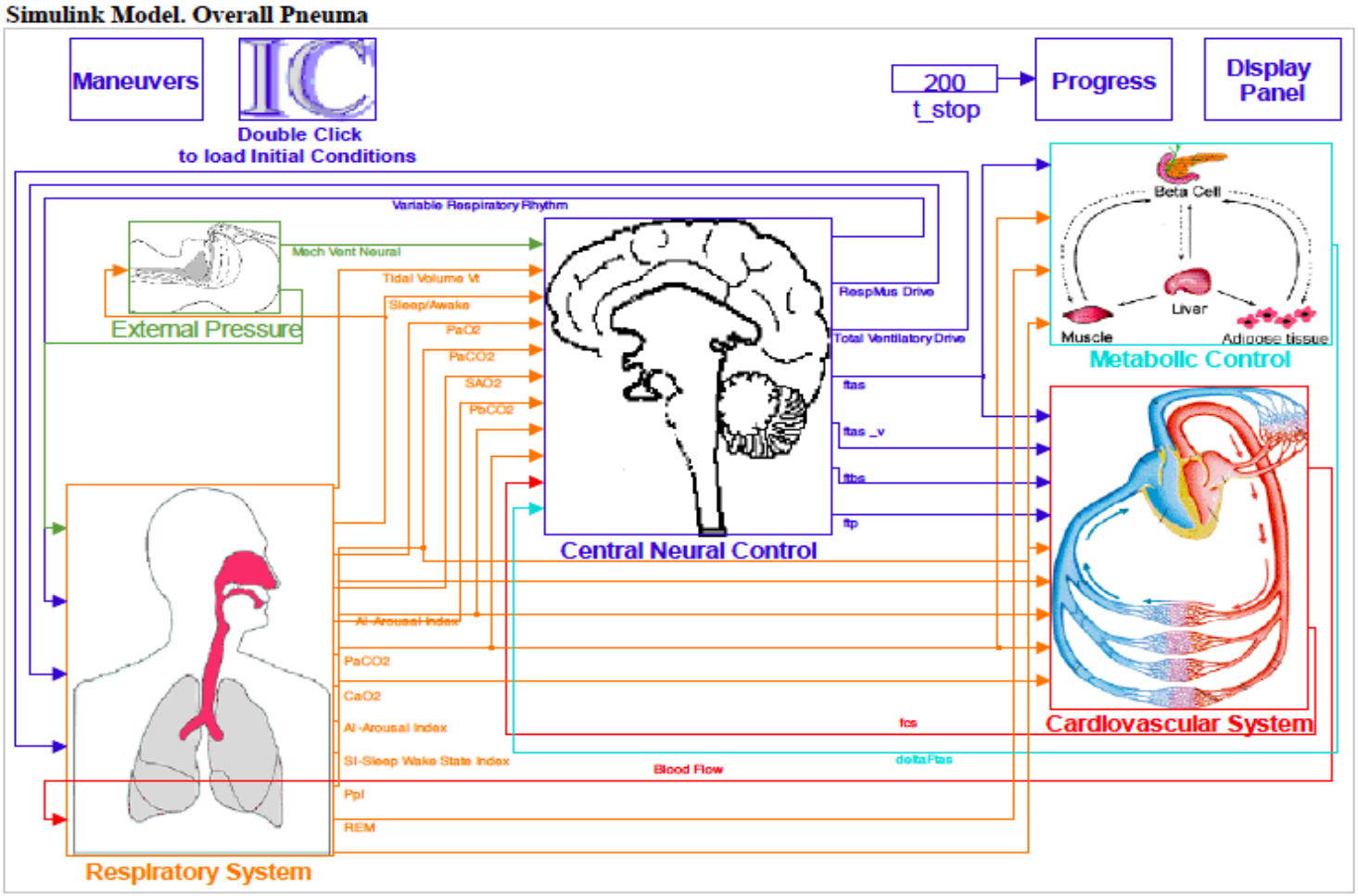

Figure 13. Cardiorespiratory model, PNEUMA (Hsing-Hua & Khoo, 2002)

The PNEUMA oxygen transport model has been benchmarked for hypercapnia, hypoxia, periodic breathing and moderate exercise with realistic trends against many alternatives (Cheng, Ivanova, Fan, & Khoo, 2010; Mananas et al., 2003). These situations encompass a range of breathing activities encountered in spaceflight. The model is divided into interconnected differential equations with sections for the alveolar space, body tissue, and central nervous system feedback mechanisms. Oxygen consumption and carbon dioxide production inclusive of the respiratory quotient as found in the alveolar-gas equation may be applied to input and outputs of this model. Inputs and output variables in the lung of this model are provided in Figure 14 and 15.

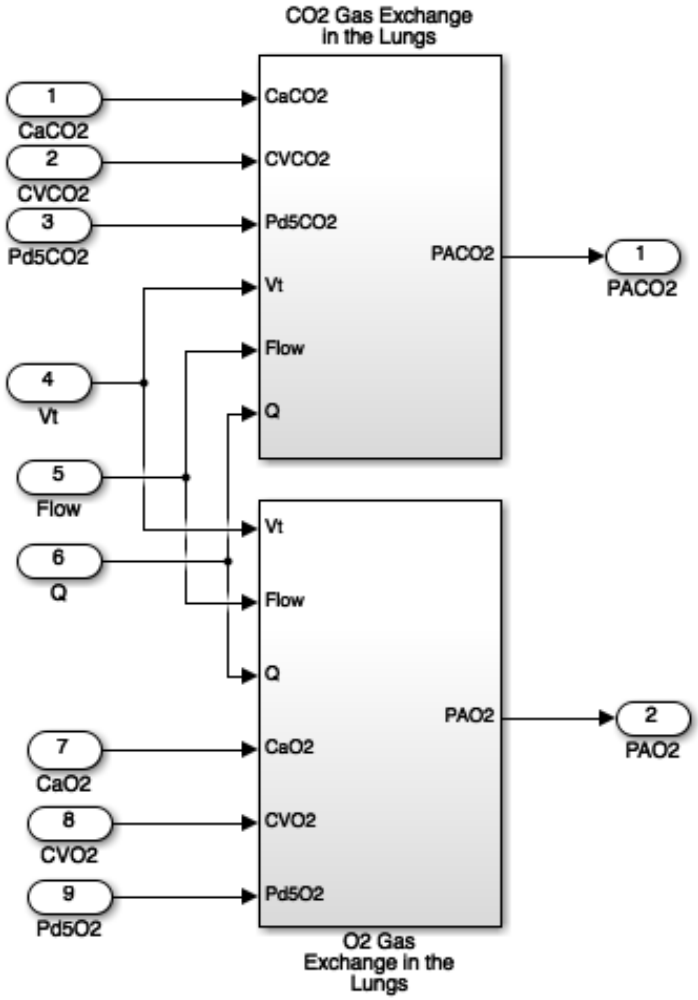

Figure 14. PNEUMA arterial and alveolar partial pressures associated with gas exchange in the lungs (Hsing-Hua & Khoo, 2002)

In order to account for skin oxygen tension in epidermal layers, external boundary conditions of measured epidermis tension values were taken from literature (Evans & Naylor, 1967; Roszinski & Schmeller, 1995) (Wang et al., 2003) and internal dermal oxygen tension acquired from the cardiovascular models (Hsing-Hua & Khoo, 2002) (Harada, Kubo, Mori, & Sato, 2005) were obtained and applied to the time dependent Fick's Second Law (Equation 5)

$$D\left(\frac{\partial^2 CO_2}{\partial x^2}\right) = \frac{\partial CaO_2}{\partial t} \qquad \text{Equation 5}$$

where Oxygen concentration CO_2 is expressed, as a function of linear distance X across the epidermis and C_aO_2 is the arterial concentration of oxygen (ml O_2/100ml).

The diffusion approximation provides that there is no oxygen flux at partial pressure equilibrium and experiments have validated this assumption. A minimum intracutaneous pO_2 of 51 mmHg has been recorded for exposed skin (Evans & Naylor, 1967; Roszinski & Schmeller, 1995). Other measurements with covered skin have pO_2 range from 8 to 35 mmHg or 1.1 to 4.6 % of 1 atm (Wang et al., 2003).

The arterial concentration of oxygen (C_aO_2) is a standardized physiological quantity that reflects the volumetric amount of oxygen in tissue from dissolved oxygen and oxygen bound to hemoglobin (oxyhemoglobin) and is calculated in Equation 6. This arterial concentration will be provided by PNEUMA for various respiratory trials and propagated across the epidermis as represented in Figure 11.

$$C_aO_2\left[\frac{ml\ O_2}{100\ ml\ blood}\right]$$

$$= \left(Hb\left[\frac{gm\ Hb}{100\ ml\ blood}\right] x\ 1.34\left[\frac{ml\ O_2}{gm\ Hb}\right] x\ S_a O_2\ [\%] \right)$$

$$+ \left(P_aO_2[mmHg\ ]\ x\ .003\left[\frac{ml\ O_2}{100\ ml\ blood * mmHg}\right] \right)$$

Equation 6

where Hb is the grams of Hemoglobin per 100ml of blood (usually 12-16), S_aO_2 is the percent arterial oxygen saturation of hemoglobin and P_aO_2 is the arterial oxygen tension. From this relationship it can be discerned, except for cases of anemia or hyperbaric oxygen treatment, that oxyhemoglobin is the most significant contributor of oxygen content in the blood and oxygen delivery to tissues.

The arterial concentration of oxygen (C_aO_2) is strictly a volumetric percent quantification of oxygen in blood. In order to provide inputs for oxygen concentration gradients and metabolic consumption a mass density or molar quantification is necessary. A single hemoglobin molecule contains four oxygen-bonding sites (Figure 16). Oxygen saturation, SO_2 describes the percent of these binding sights occupied by oxygen and is approximately 100% in healthy individuals while in the arteries (S_aO_2) and decreasing as oxygen is deposited into tissues and blood enters the venous system.

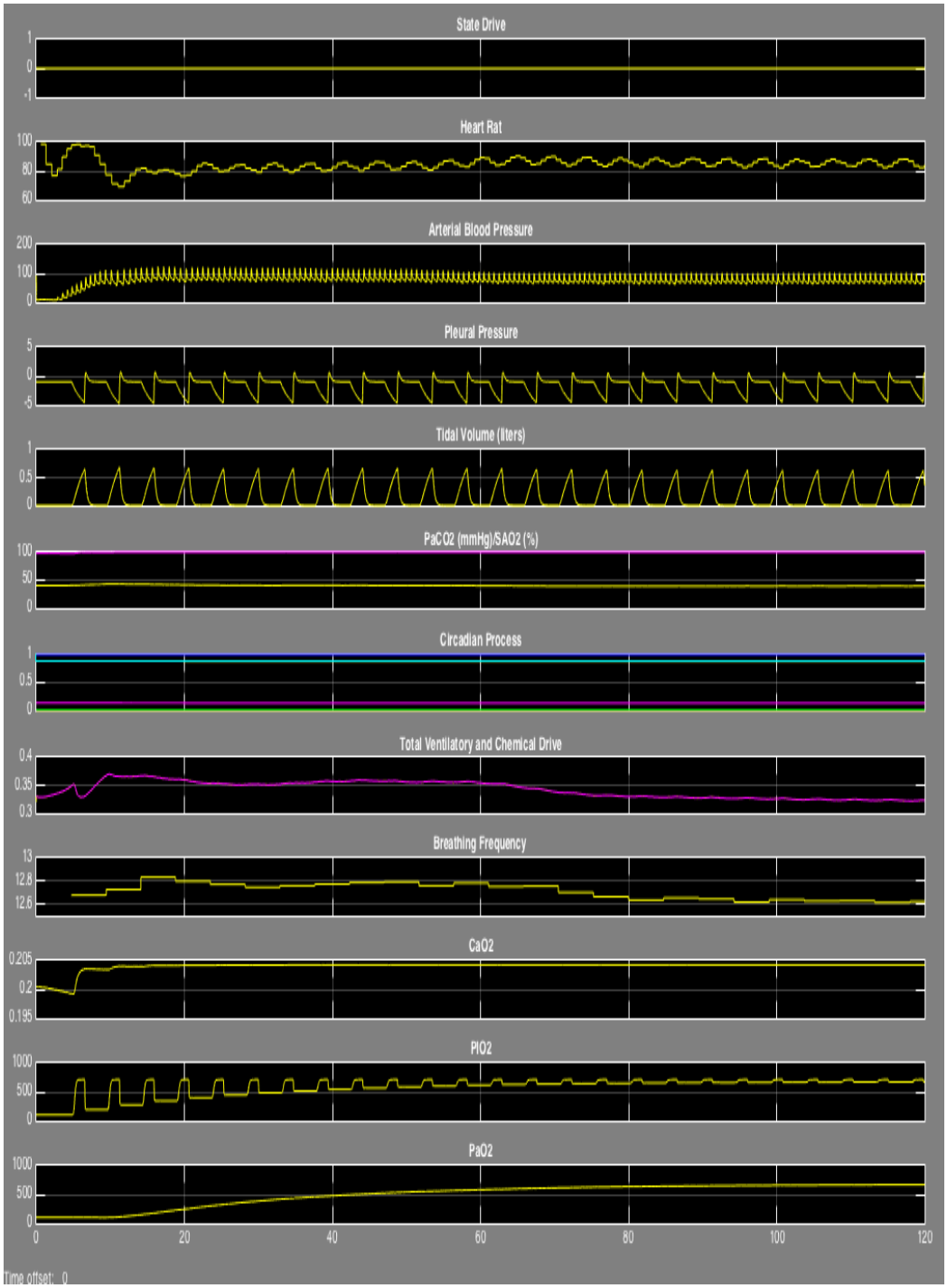

Figure 15. PNEUMA outputs from 100% oxygen breathing at 1 atmosphere (760 mmHg) at t=0. (Pressure of inspired oxygen P_iO_2 713mmHg)

Using the previously described hemoglobin density Hb, arterial oxygen saturation S_aO_2, and hemoglobin binding sights the molar density of oxygen may be obtained in hematocrit (packed red blood cell volume). In order to determine the molar density of oxygen in plasma, Henry's Law may be applied (Equation 7). Summing both the hematocrit and plasma oxygen molar density components will provide total oxygen molar density.

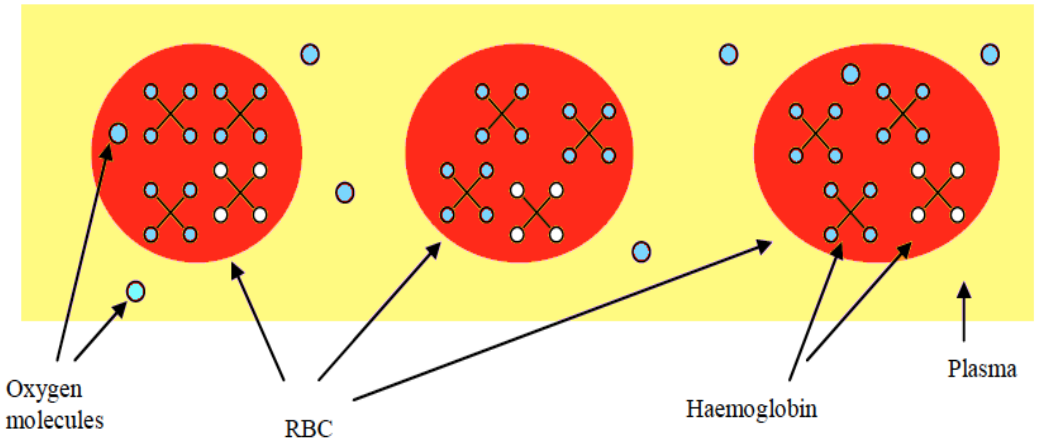

Figure 16. Visual depiction of oxygen-hemoglobin binding on red blood cells in plasma.

$$C_p = \propto * P_{O_2} \qquad \text{Equation 7}$$

where C_p is the concentration of oxygen, α is the solubility coefficient and P_{O2} is the partial pressure of oxygen.

2.5 Oxygen Dependence Simulation

The exact mechanism of cell death and inflammation due to radiation exposure is still an area of active investigation. A large body of evidence supports the initiation and processing of double-stranded breaks (DSB) in nuclear DNA as a primary factor in reproductive cell death (Carlson et al., 2008), although other interactions may be significant including that of non-targeted effects (NTE). In skin exposure, NTE manifest in deterministic fashion in response to cell death; ionizing radiation leads to accumulation of lymphocytes and macrophages in the layers of the skin and eventually leads to the development of erythematous skin changes (Peter, 2005).

There are several hypotheses which try to explain the Oxygen Enhancement Ratio (OER) in cellular processes in more detail (Masunaga et al., 2009; Michael & Prise, 1996; Stuglik, 1995; Ward, 1994) but to date there is no consistent theory that could explain the oxygen effect on a specific physical basis. In order to correlate the response of a biological system to radiation as a function of the oxygen partial pressure pO_2, a correlation termed relative radiosensitivity (RR) was developed by Alper (Alper & Howard-Flanders, 1956). Utilizing this correlation, the survival of cells irradiated under varying oxygen concentrations are well approximated by a modified linear-quadratic (LQ) cell survival model (Stewart et al., 2011), i.e., the fraction S of the cells surviving absorbed dose D is shown in Equation 8. Here, α and β characterize intrinsic cellular radiation sensitivity dependent on oxygen and G is the dose protraction factor.

$$S = e^{(-\alpha*D - \beta*G*D^2)} \qquad \text{Equation 8}$$

In the linear-quadratic model, two components of cell injury are present. The linear α component is responsible for the initial shoulder on the cell survival curve and is caused by general single detriment repairable damage to the DNA. The quadratic β component represents multiple detriments to the DNA with a G protraction or repair factor. The linear component is proportional to the dose, whereas the quadratic component is proportional to the dose squared.

Early-responding tissues and tumors have a relatively larger alpha component and a larger α/β ratio; late-responding tissues have smaller α/β ratios (Halperin, Perez, & Brady, 2008). Values of α/β for early onset erythema vary from 8-11 Gy and for desquamation 11-12 Gy. These features are incorporated into the correlation of deterministic effect in this model.

Methods to correlate DNA DSB probability with radiation track structure exist with reliable verification (Costes et al., 2007; Hauptner et al., 2006). Predicted trends in the DSB induction are consistent with estimates derived from measured data for DSB induction and cell survival curves (Carlson et al., 2008; Stewart et al., 2011).

A comprehensive microdosimetric transport software package, Monte-Carlo Damage Simulation (MCDS) (Stewart et al., 2011) simulates incident ion track structure and utilizes oxygen fixation as an indicator of DNA radicals removed through the chemical repair processes. In this procedure, the relative radiosensitivity (RR) equation

developed by Alper and Howard-Flanders (Alper & Howard-Flanders, 1956) is modified for use in the oxygen fixation DNA repair mechanism. This enables a direct correlation of oxygen dependence and DSB incidence with cell survival curves. A sample output of MCDS OER for trials of varying LET versus baseline experimentation is shown on Figure 17.

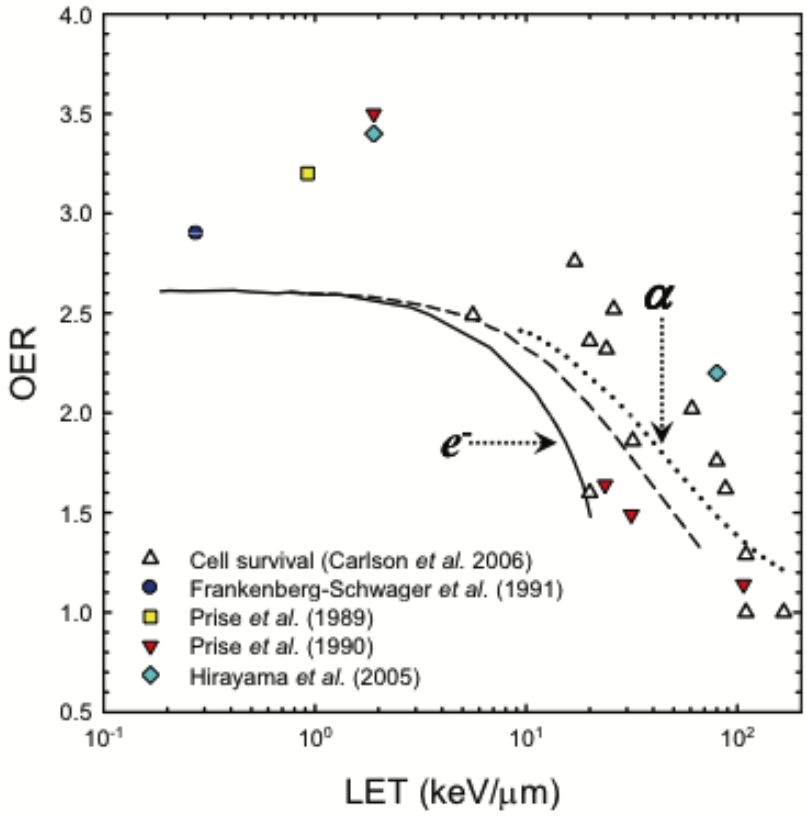

Figure 17. MCDS simulations of OER vs LET by particles type (Stewart et al., 2011).

3. RESULTS AND DISCUSSION

3.1 Solar Particle Transport and Energy Deposition in Matter

As the primary source particle in SPEs, protons directly contribute the largest portion of SPE dose to the skin. Secondary interaction and fragmentation may result in significant exposure contribution depending on variables inclusive of energy and material thickness. For the estimation of proton dose alone, the Bethe stopping power Formula in Equation 9 may be utilized. Variable values are provided for a water target.

$$L = .307\ (Z_t\ \rho/A_t)\ (Z_p^2/\beta^2)\ (\ln(2\ m_e\ \beta^2/(I\ (1 - \beta^2))) - \beta^2) \qquad \text{Equation 9}$$

Z_t – Atomic Number of the Target Material: 10

A_t – Mass Number of the Target Material: 18

m_e – Electron Mass: .511 MeV

I – Mean Excitation Potential: 74.9x10-6 MeV

ρ – Target Material Density: 1 gm/cm3

Z_p – Atomic Number of Incident Particle: 1

β – (particle velocity)/(speed of light)

Significant exposure to neutrons may result from nuclear interactions that increase with the amount of material utilized for shielding (Table 3). Additionally, fragmentation is a notable occurrence for high-energy interaction on target surfaces. At

aluminum thicknesses greater than 5 cm, neutrons may comprise 5% or more of the total particle flux. These attributes with the variability of radiation quality, make accounting for particle types prudent for making accurate estimates of dose and resultant biological effect.

PHITS August 1972 SPE	King Parameterization	
Thickness of Aluminum (cm) (density = 2.7 gm/cm^3)	Particle	% of Fluence PHITS Transport Calculation
0.1	Proton	97.11
	Neutron	2.70
	d,t,3He,4He	0.19
1	Proton	96.40
	Neutron	3.46
	d,t,3He,4He	0.14
5	Proton	95.22
	Neutron	4.70
	d,t,3He,4He	0.08
13.5	Proton	93.90
	Neutron	6.03
	d,t,3He,4He	0.07

Table 3. Total particle flux percent for the August 1972 SPE transported by PHITS vs. aluminum thicknesses of 0.1, 1, 5 and 13.5 cm (density = 2.7 gm/cm^3)

PHITS provides dose and flux tallies normalized to the particle source or source flux, if applicable, in units of (MeV/Source) for t-deposit and (1/cm^2/Source) for t-track and t-cross. T-cross is used exclusively for flux or current crossing a surface, while t-track is sum of track lengths (cm) that intersect a defined volume. Since the flux t-cross tally is evaluated with weight of 1/cos θ, the result is equivalent to that obtained from the [t-track] tally for an extremely thin region. This assumption is useful for simulating

transport through thin layers of skin or shielding. However for purposes of extendibility macroscopic volumes are assumed as a baseline assumption, therefore the t-track tally is used for flux attribution within material volumes.

This normalized output is useful to examine the relevance of energy distribution for deposition and transport through matter. Spectra weighted towards higher energy, such as the 1956 SPE distribution (J. W. Wilson, 1976) result in greater energy deposition at increasing depth (Figure 18).

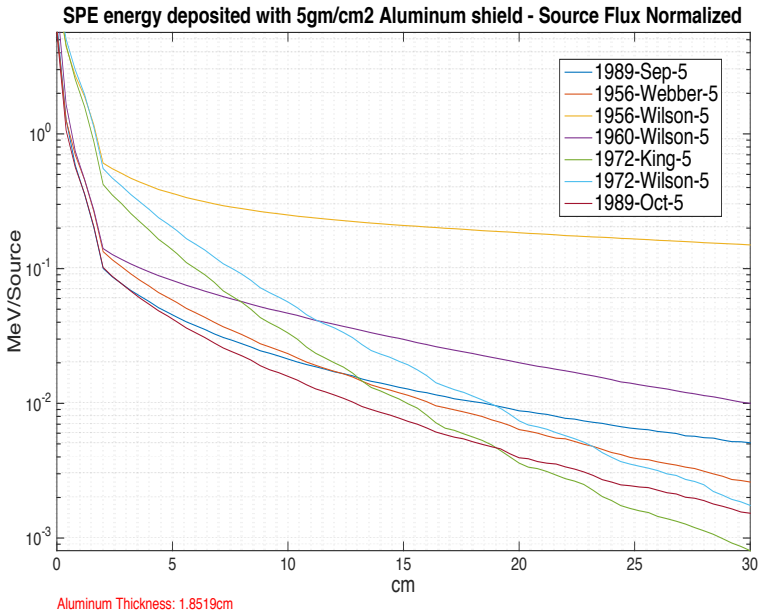

Figure 18. Flux normalized energy deposited as a function of depth with 5 gm/cm^2 of aluminum equivalent shielding from 1956, 1960, 1972, and 1989 SPEs. Energy absorbed is represented in aluminum for z < = 1.85 and water for z > 1.85 cm.

In order to correctly represent the total absorbed dose of a respective SPE, these PHITS outputs must be scaled to their respective particle flux (Table 4). A script was written in MATLAB® in order to properly attribute and generate data for comparison

(Appendix B.1). The units of MeV/Source are weighted by source flux with resultant units of MeV/cm^2.

SPE Event Date	Data Source	Total Source Particle Flux cm-2
February 1956	NASA Langley (Wilson)	ϕ=2.52E+09
	Webber	ϕ=1.01E+10
November 1960	NASA Langley (Wilson)	ϕ=1.79E+10
August 1972	NASA Langley (Wilson)	ϕ=1.76E+10
	King	ϕ=2.33E+10
October 1989	NASA Langley (Sauer)	ϕ=5.21E+10
September 1989	NASA Langley (Sauer)	ϕ=1.41E+10

Table 4. Total particle flux for selected SPE data sets

From the five SPEs simulated, total dose for a range of shielding thicknesses indicate the August 1972 event to be of most concern for the selected shield thicknesses and consideration of dermis and epidermis dimensions (Figure 19). This is despite a higher overall flux is attributed to the October 1989 event. Prior publications have verified this result (Figure 20).

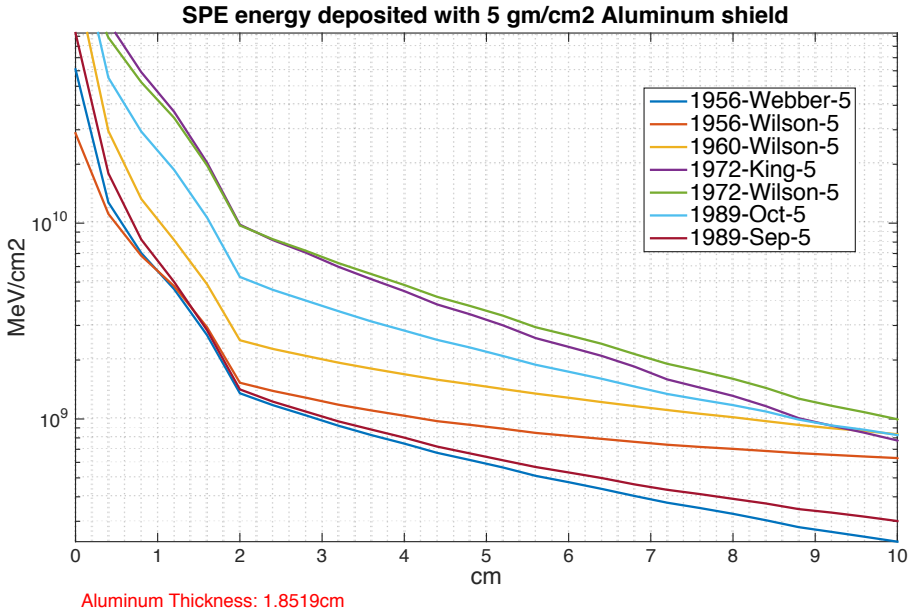

Figure 19. Energy deposited as a function of depth with 5 gm/cm^2 of aluminum equivalent shielding from 1956, 1960, 1972, and 1989 SPEs. Energy absorbed is represented in aluminum for z < = 1.85 and water for z > 1.85 cm.

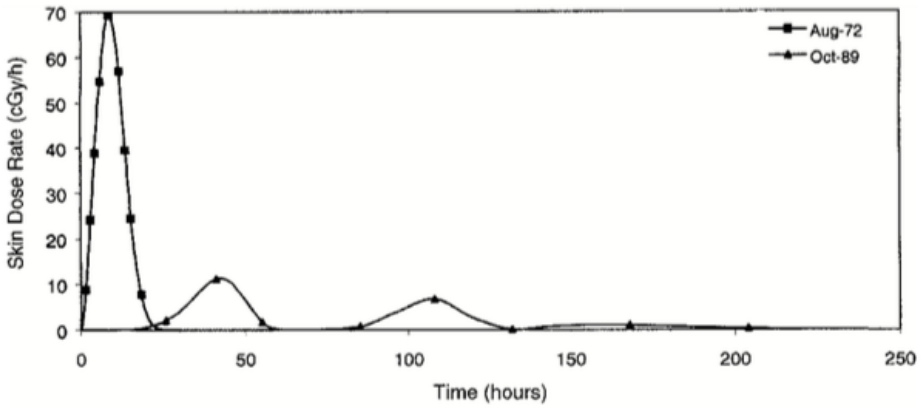

Figure 20. Comparison of the predicted skin dose rates for the August 1972 and October 1989 SPEs as a function of time since event onset and behind 2 g/cm2 aluminum shielding (Parsons & Townsend, 2000).

Comparing the energy spectrums from the August 1972 and October 1989 SPE differential spectrums, it can be discerned that the August 1972 event has significantly greater flux component from energies 30 MeV to 150 MeV. This difference in energetic flux is most pronounced in the data reported by (King, 1974) (Figure 21).

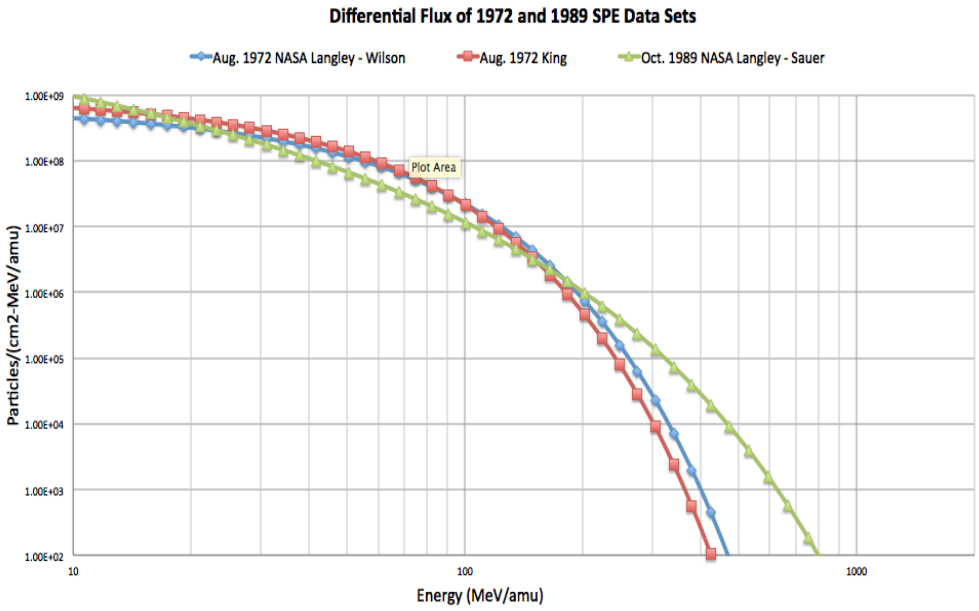

Figure 21. Comparison of energy differential particle fluence for the August 1972 and October 1989 SPEs (King, 1974; Sauer, 1990; J. W. Wilson, 1976)

However, due to the lesser amount of flux at energies above 150 MeV from the August 1972 SPE, energy deposition decreases below that of other SPE at several centimeters of depth (Figure 22 - 5 gm/cm^2). It should also be noted that as the thickness of the aluminum shield increases, a decrease in flux and energy deposition from August 1972 SPEs below that of other SPEs occurs (Figure 23 - 12.9 gm/cm^2 and Figure 24 - 0.2

gm/cm^2). This is physically explained by the reduction in greater penetrating higher energy flux from the increase in aluminum shielding.

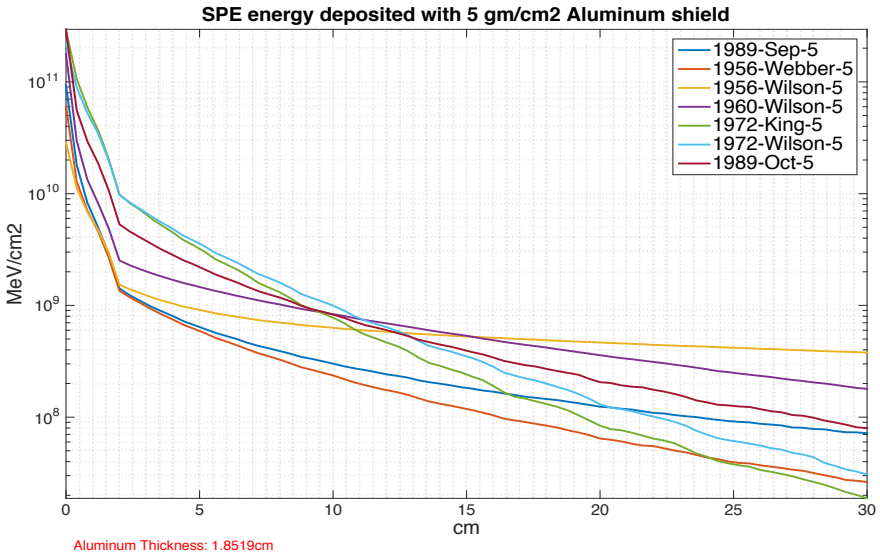

Figure 22. Energy deposited as a function of depth with 5 gm/cm^2 of aluminum equivalent shielding from 1956, 1960, 1972, and 1989 SPEs. Energy absorbed is represented in aluminum for z < = 1.85 and water for z > 1.85 cm.

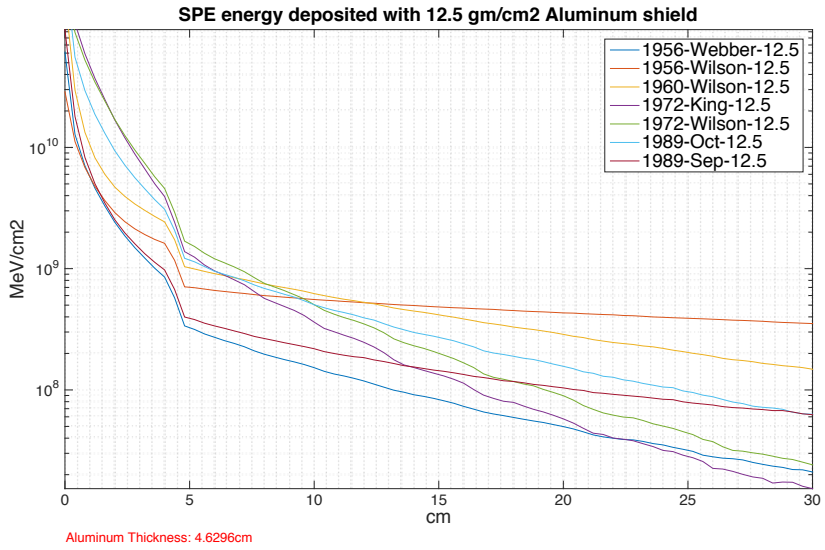

Figure 23. Energy deposited as a function of depth with 12.5 gm/cm^2 of aluminum equivalent shielding from 1956, 1960, 1972, and 1989 SPEs. Energy absorbed is represented in aluminum for z < = 4.62 cm and water for z > 4.26 cm.

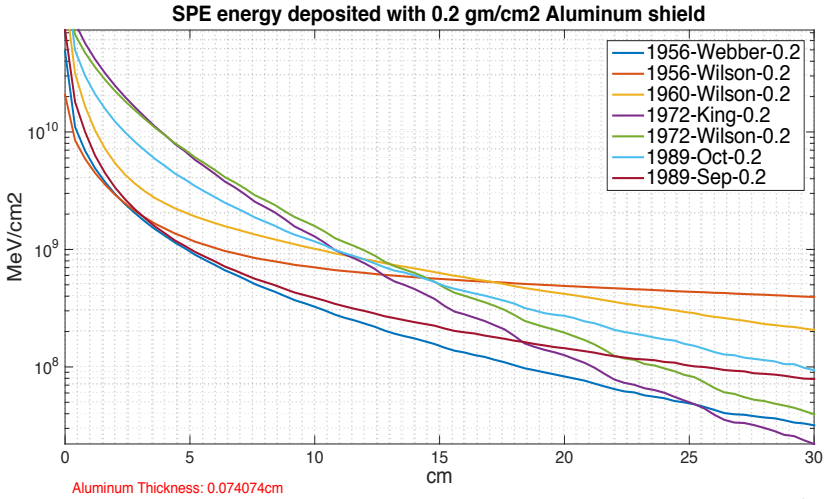

Figure 24. Energy deposited as a function of depth with 0.2 gm/cm^2 of aluminum equivalent shielding from 1956, 1960, 1972, and 1989 SPEs. Energy absorbed is represented in aluminum for z < = 0.07 and water for z > 0.07 cm.

For the selected shield thicknesses and consideration of dermal and epidermal dimensions, the energy deposited by SPEs like August 1972 and October 1989 SPEs are most indicated to initiate deterministic effect to the skin. Therefore, these specific datasets will be utilized for MCDS simulation.

3.2 Particle Flux Incident on Skin

The MCDS code is a Monte Carlo and microdosimetric simulation that attributes energy deposition within a cellular volume from incident particle energy fluence. Therefore, it is prudent that incident flux is utilized to allow for the microdosimetric calculations. Future revisions of this work may seek to integrate the microdosimetric capabilities of PHITS with the [t-sed] tally.

Incident fluxes on skin were estimated from PHITS with aluminum shields of 0.1, 1, 5 and 13.5 cm at a density of 2.7 g/cm^3. For the U.S. EMU, aluminum equivalent thicknesses of 0.1 and 5 cm are most descriptive of EMU shielding (Zeitlin et al., 2001) while thicknesses greater than 1 cm are common in spacecraft. Expectedly, proton fluxes decreased as shielding increased. This result may be viewed in Figures 25, 26, 27 and 28.

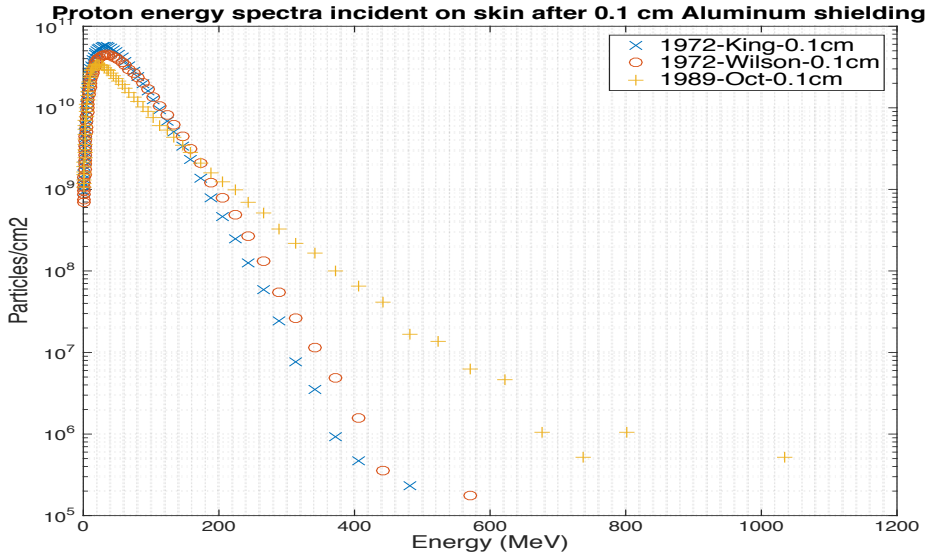

Figure 25. Proton flux as a function of energy behind 0.1 cm (0.27 gm/cm^2) of aluminum equivalent shielding for 1972, and 1989 SPEs.

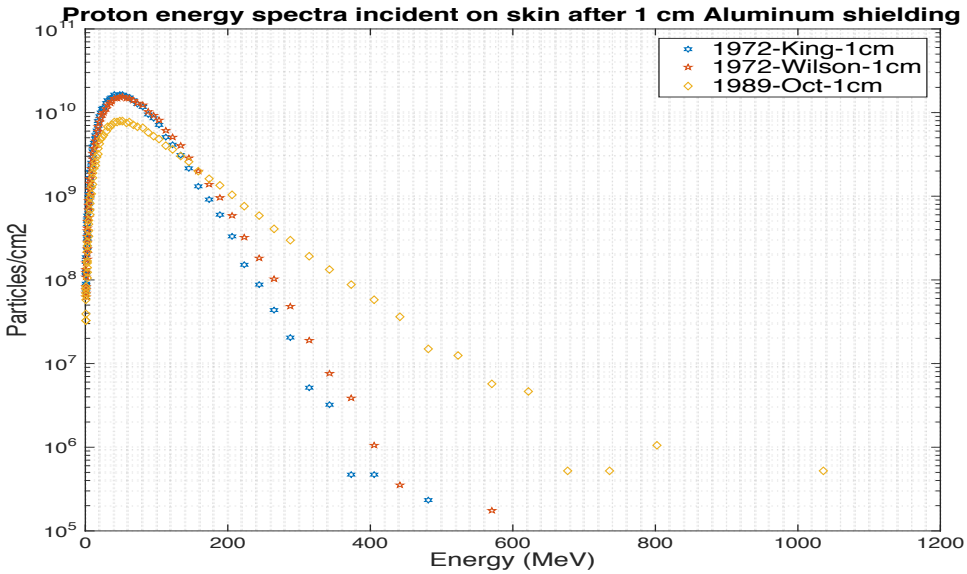

Figure 26. Proton flux as a function of energy behind 1 cm (2.7 gm/cm^2) of aluminum equivalent shielding for 1972, and 1989 SPEs.

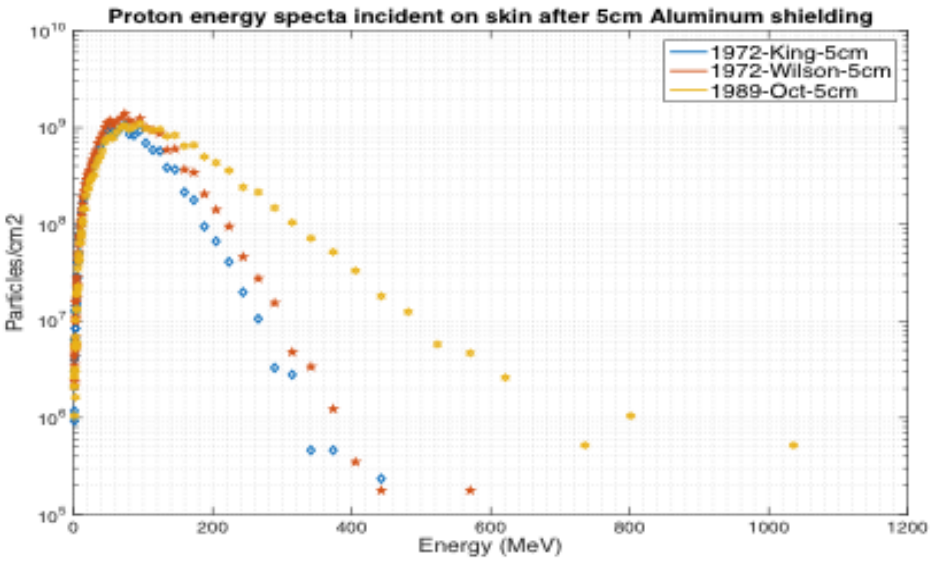

Figure 27. Proton flux as a function of energy behind 5 cm (13.5 gm/cm^2) of aluminum equivalent shielding for 1972, and 1989 SPEs.

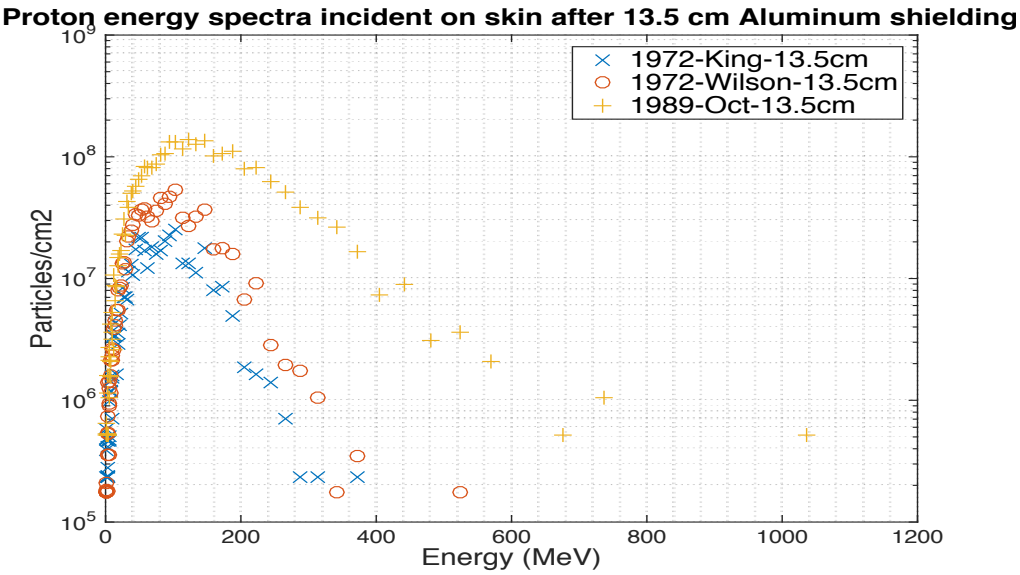

Figure 28. Proton flux as a function of energy behind 13.5 cm (36.5 gm/cm^2) of aluminum equivalent shielding for 1972, and 1989 SPEs.

The 1972 SPE events maintain a higher flux distribution below 150 MeV however, as shielding increases beyond 5 cm standard aluminum equivalent thickness, the 1989 SPE event indicates higher overall flux. This decrease in the 1972 SPE proton flux is associated with significant dose attribution from proton energies less than 150 MeV. This is notable since to the typical thickness of EVA shielding is less than 5 cm.

This proton interaction in aluminum equivalent shielding also gives rise to a number of secondary interactions and particles most notably neutrons, electrons and alpha particles. Neutron generation is shown in Figures 29, 30, 31 and 32. Neutrons interact primarily with recoil collisions or absorption and the resultant localized energy deposition can be much higher than the incident proton spectra as well as give rise to even more secondary particles.

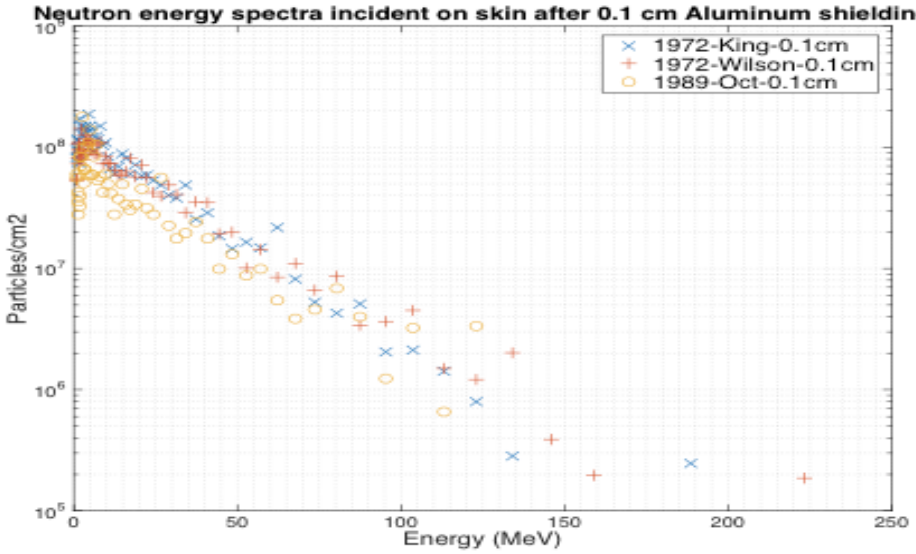

Figure 29. Neutron flux as a function of energy behind 0.1 cm (0.27 gm/cm^2) of aluminum equivalent shielding for 1972, and 1989 SPEs.

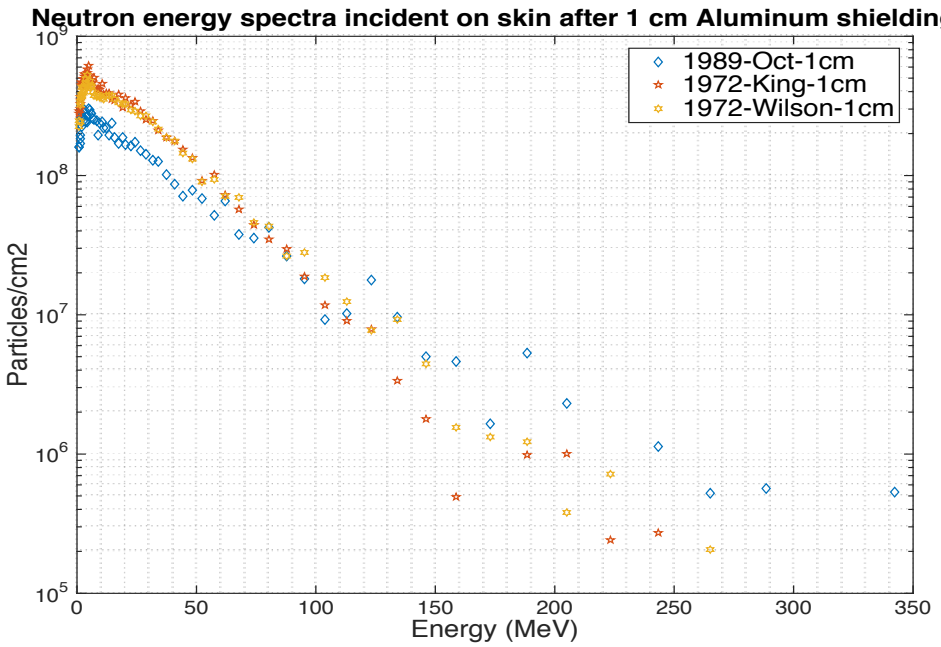

Figure 30. Neutron flux as a function of energy behind 1 cm (2.7 gm/cm^2) of aluminum equivalent shielding for 1972, and 1989 SPEs.

It can be readily discerned that a minor increase of shielding from 0.1 cm to 1cm results in a significant increase of neutron flux across much of the lower energy range up to 150 MeV. The lower weighted energy of the neutrons is significant since this is indicates a higher likelihood of localized energy deposition in the surrounding media. This energy deposition can be observed in Figures 31 and 32.

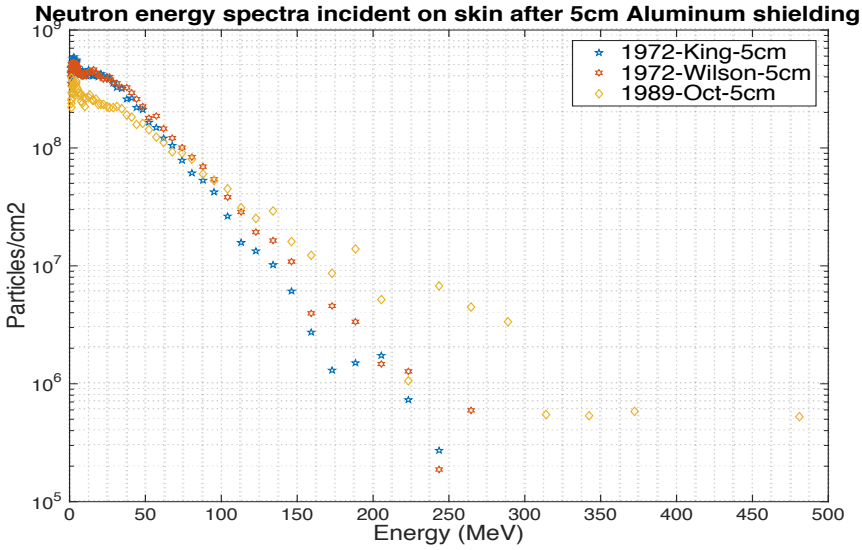

Figure 31. Neutron flux as a function of energy behind 5 cm (13.5 gm/cm^2) of aluminum equivalent shielding for 1972, and 1989 SPEs.

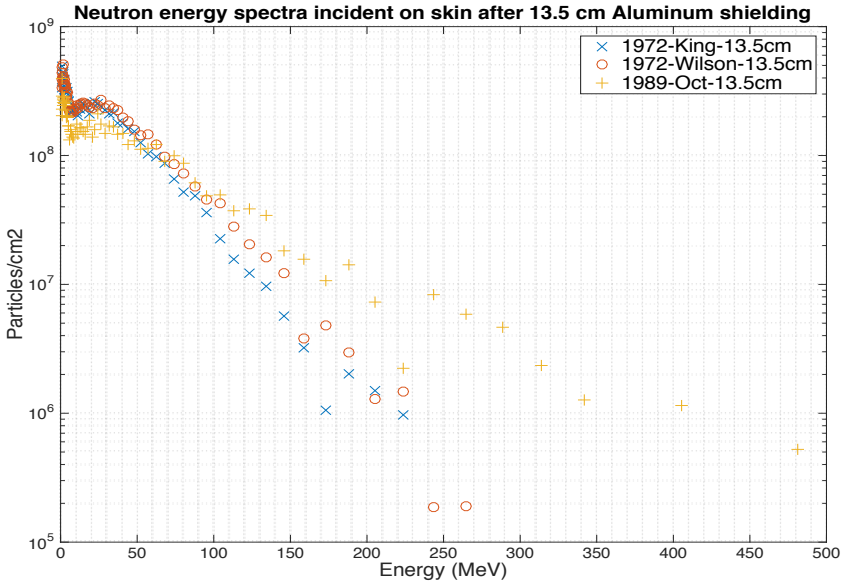

Figure 32. Neutron flux as a function of energy behind 13.5 cm (36.5 gm/cm^2) of aluminum equivalent shielding for 1972, and 1989 SPEs.

Further increases in shielding drastically remove low energy neutrons as they are generated in the aluminum shielding. The resultant energy deposition can be discerned via electron flux and to a lesser extent from nuclear interaction that produces alpha particles. This resultant increase in electron flux inclusive of delta ray contribution as shielding thickness increases can be seen in Figures 33, 34 and 35.

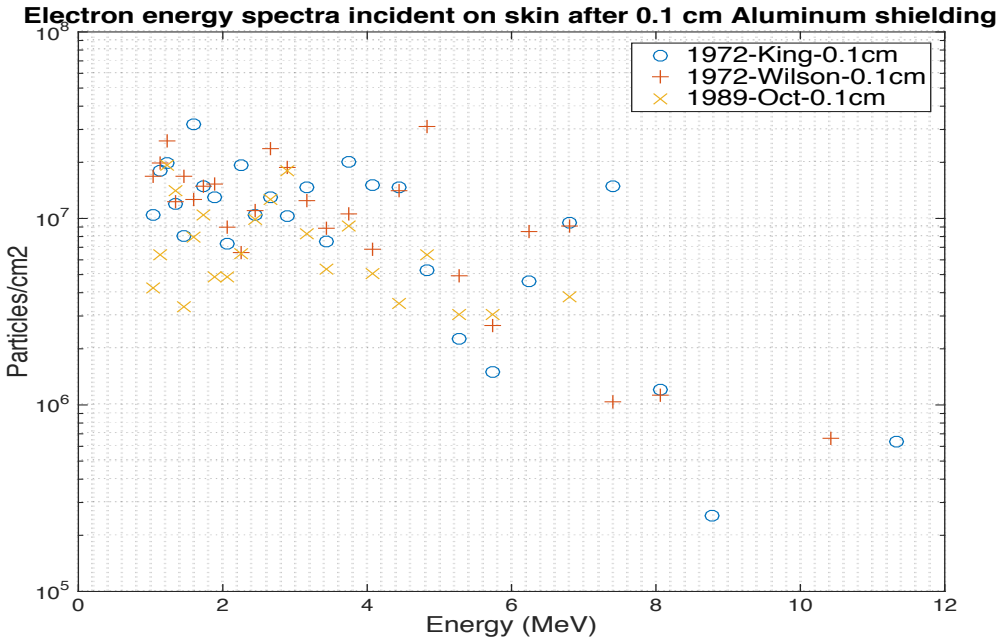

Figure 33. Electron flux as a function of energy behind 0.1 cm (0.27 gm/cm^2) of aluminum equivalent shielding for 1972, and 1989 SPEs.

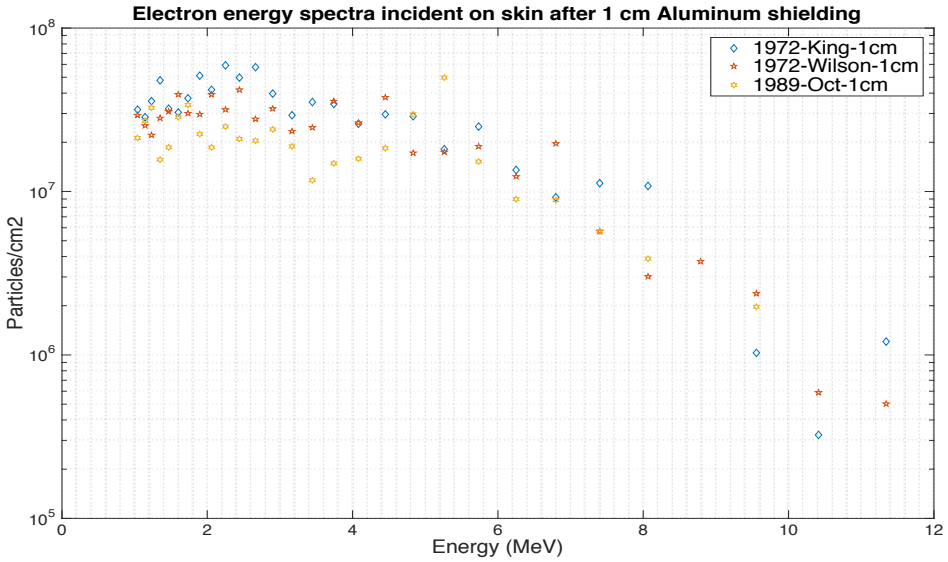

Figure 34. Electron flux as a function of energy behind 1 cm (2.7 gm/cm^2) of aluminum equivalent shielding for 1972, and 1989 SPEs.

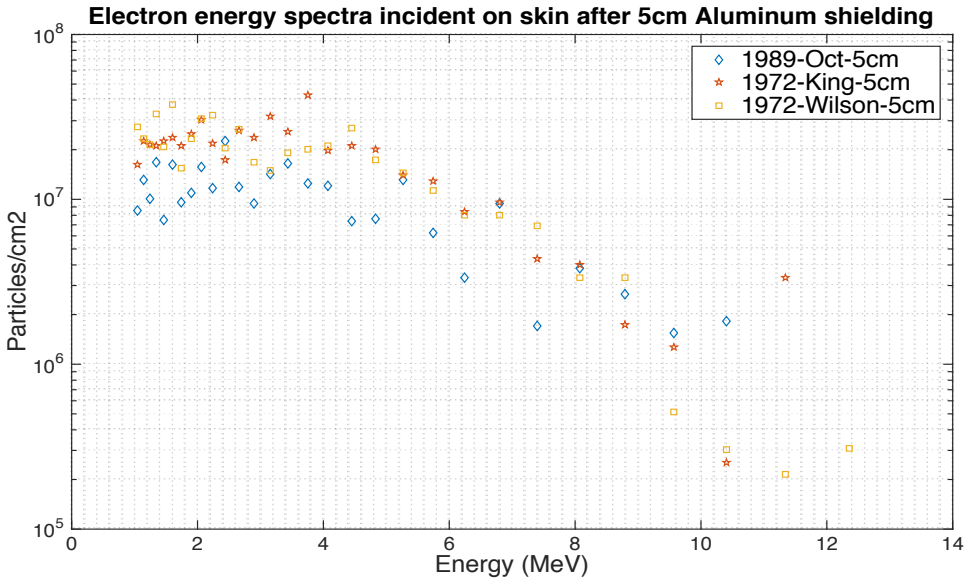

Figure 35. Electron flux as a function of energy behind 5 cm (13.5 gm/cm^2) of aluminum equivalent shielding for 1972, and 1989 SPEs.

In Figure 35 the electron flux at 5 cm shielding thickness appears to have reduced slightly from that of 1 cm shielding thickness. This is indicative of reduction of primary incident flux and overall reduction in energy deposition. Similarly, the generation of alpha particle flux from pathways such as high-energy fragmentation on the shielding surface and subsequent nuclear interaction such as from neutron absorption substantially decreases as shielding thickness increases. Alpha fluxes are shown in Figures 36 and 37.

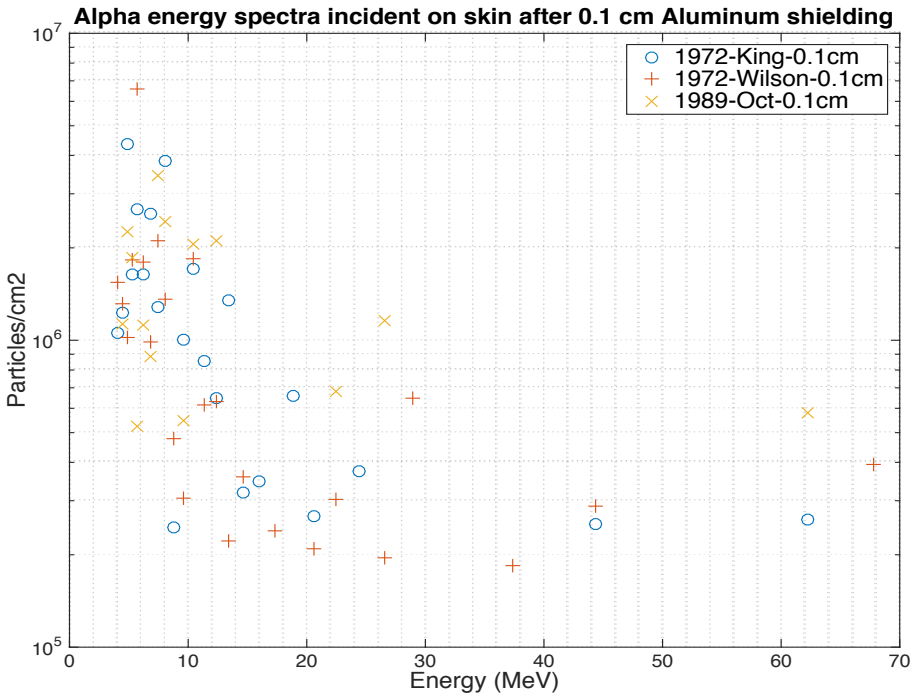

Figure 36. Alpha paticle flux as a function of energy behind 0.1 cm (0.27 gm/cm^2) of aluminum equivalent shielding for 1972, and 1989 SPEs.

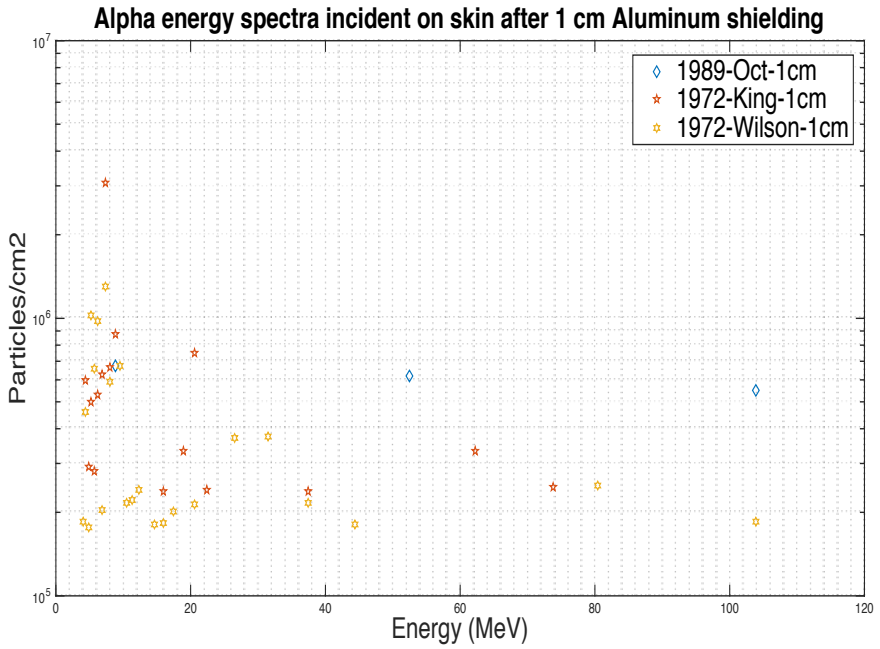

Figure 37. Alpha particle flux as a function of energy behind 1 cm (2.7 gm/cm^2) of aluminum equivalent shielding for 1972, and 1989 SPEs.

These respective particle fluxes of all simulating shielding thicknesses are applied to the MCDS model with a dependent oxygen concentration based on the proceeding physiological simulation.

3.3 Oxygen Tension in Epidermal Layers

Oxygen tensions in epidermal layers were simulated for three skin thicknesses: thin, average and thick to encompass the full range of epidermal diffusion.

Epidermal Size	Thickness	Anatomy
Thin	0.005 cm	Eyelids
Average	0.01 cm	Shoulder, Forearm
Thick	.15 cm	Palm, soles

Table 5. Epidermal simulation thicknesses

It is assumed the stratum corneum has a constant thickness of 15 µm and stratum basal, stratum spinosum and stratum granulosom layers evenly divide the remainder thickness. Under normal conditions the upper skin layers are supplied exclusively by the diffusion of oxygen from the atmosphere.

The application of Fick's First Law yields oxygen flux, J and partial pressure of O_2 at position x in a single directional gradient under the steady state assumption Equation 10 and 11.

$$J = K\left(\frac{\partial PO_2}{\partial x}\right) \qquad \text{Equation 10}$$

$$PO_2(x) = \frac{J*x}{K} + c_1 \qquad \text{Equation 11}$$

The oxygen permeabilities, K may be assumed from literature as 3.7 x 10^{-7} (ml O_2) / (m min Torr) in the stratum corneum and 1.3 x 10^{-6} (ml O_2) / (m min Torr) in viable tissue (Huch & Lubbers, 1981). While the permeability coefficient is proportional to the diffusion coefficient, it is traditionally independent of certain quantities, such as thickness, x which is significant due to the oxygen consumption and diffusion dynamic

through tissue layers. In order to maintain standardized units a diffusion constant, D is used in lieu of permeability constant (Table 6).

In compliance with Fick's First Law there is no oxygen flux, J between the upper layer PO_2 and the skin tissue below the point at which the minimum oxygen tension is reached. Tissue beneath this minimum is exclusively provided oxygen by the cardiovascular system. This necessitates numerous boundary conditions to accommodate skin layers and direction of oxygen transients. The boundary conditions for elimination of oxygen flux, flux continuums between stratum corneum, stratum granulosum, stratum spinosum and basal layer are presented in Equation 12,13,14, 15 and 16.

$$\frac{\partial J}{\partial x} = 0 \ @ \ \min_x PO_2(x) \qquad \text{Equation 12}$$

$$J_{stratum\ corneum}(x_1) = J_{stratum\ granulosum}(x_1) \qquad \text{Equation 13}$$

$$J_{stratum\ corneum}(x_2) = J_{stratum\ granulosum}(x_2) \qquad \text{Equation 14}$$

$$J_{stratum\ granulosum}(x_3) = J_{stratum\ spinosum}(x_3) \qquad \text{Equation 15}$$

$$J_{stratum\ spinosum}(x_4) = J_{basal\ layer}(x_4) \qquad \text{Equation 16}$$

As oxygen diffuses across a thickness x, concentration (or partial pressure) will change unless continuous gradient is maintained. For the transients associated with space travel, this necessitates tracking of changes in this gradient as a function of time.

The time dependent Fick's Second Law may be arranged to equate volumetric oxygen consumption across layers as a function of time, V resulting in an Inhomogeneous second-order Partial Differential Equation (PDE). This may used to

simulate oxygen tension through the stratum corneum, viable epidermis and viable tissue.

$$\frac{\partial C}{\partial t} = D\left(\frac{\partial^2 C}{\partial x^2}\right) - V \qquad \text{Equation 17}$$

where the concentration of oxygen is C (ml O_2/100ml)

Average oxygen consumption, V has been measured and published in literature (Table 6). However, in the dead skin layer, or stratum corneum there is no oxygen consumption (V = 0) and this results in a homogenous differential equation.

Variable	Value
V – Living Epidermis	1990 ml O2 m^{-3} min^{-1} (1)
V – Stratum Corneum	0
V – Dermal Tissue	1470 ml O2 m^{-3} min^{-1} (1)
D - Epidermis	1 x 10^{-6} cm^2 s^{-1} (2)
D - Stratum Papillare Tissue (Dermis)	1.5 x 10^{-5} cm^2 s^{-1} (2)
C_o – Epidermal Oxygen Solubility	8.9 nmol ml^{-1} kPa^{-1} (3)
C_o – Epidermis (Normoxic) at surface	189.85 nmol ml^{-1} ; 0.18995 mM (3)

Table 6. Constants utilized in the oxygen diffusion simulation. 1) (Evans & Naylor, 1967) 2) (Grossmann, 1982; Talbot, Neuman, Saidel, & Jacobsen, 1996) 3) (Siggaard-Andersen, Wimberley, Göthgen, & Siggaard-Andersen, 1984; Talbot et al., 1996)

Solving this equation for oxygen concentration under the steady state assumption as a function of depth C(x) in a single oxygen gradient yields (Equation 18):

$$C(x) = \left({}^{V}/_{2D}\right) x^2 + C_1 x + C_2 \qquad \text{Equation 18}$$

A minimum intracutaneous pO_2 of 51 mmHg has been recorded to exposed skin (Evans & Naylor, 1967; Roszinski & Schmeller, 1995). Other measurements with covered skin have pO_2 range from 8 to 35 mmHg or 1.1 to 4.6 % of 1 atm (Wang et al., 2003). The resulting constants c_1 and c_2 may be solved by boundary condition associated with epidermal and dermal layers.

This description is problematic in that it assumes constant consumption, Vi throughout the cellular volume. Experimentation has confirmed that oxygen consumption is dependent on oxygen concentration in living cells due to adaptive metabolic processes (Bingmann & Kolde, 1982). To better account for this effect Michaelis–Menten kinetics with origin in enzyme reaction rates was utilized in all cell layers accept for the stratum corneum, whereas no consumption is assumed.

Michaelis-Menten kinetics relates the reaction rate, V_o to C, the concentration of a substance. This correlation has multiple uses for biochemical processes and is a component of oxygen fixation hypothesis within the MCDS code. Substituting the reaction rate, V (Equation 19) in the time-dependent differential equation for these kinetics results in second-order non-linear PDE presented in Equation 20.

$$V(t) = \frac{V_o * C(x,t)}{Ko + C(x,t)} \quad \text{Equation 19}$$

$$\frac{\partial C}{\partial t} = D\left(\frac{\partial^2 C}{\partial x^2}\right) - \frac{Vo * C(x,t)}{Ko + C(x,t)} \quad \text{Equation 20}$$

where V_o is the maximum rate of oxygen consumption and K_o is the concentration of oxygen at one-half maximum rate. In order to define constants V_o and M published values as measured in literature were utilized (Table 7)

Variable	Value
V_o	.059 nmol/ml-s
K_o	.075 nmol/ml

Table 7. Oxygen consumption parameters as applied to Michaelis-Menten kinetics (McGoron, Nair, & Schubert, 1997; Ohara, 1951)

Normoxic and hyperoxic induction simulations provided by PNEUMA and pre-defined constants (Appendix C) results in minimally different steady state arterial oxygen content, C_aO_2. However, this transient is significant enough to shift the oxygen concentration in skin by an observable amount. Converting CaO_2, a volumetric quantity into molar density for oxygen gradient equations requires a density conversion for blood as well as molar density for oxygen for both hemoglobin and dissolved oxygen contributions. Fortunately, the density of blood has negligible dependence from oxygen and carbon dioxide content. In order to standardize output a constant hemoglobin concentration will be utilized.

A blood density of 1060 kg /m^3 (1.060 gm/cm^3) (Shmukler, 2004) and the molecular weight of hemoglobin is established as 64450 g/mol with minimal variation (Van Beekvelt, Colier, Wevers, & Van Engelen, 2001). The hemoglobin density in blood is chosen as 150 g/L based on ranges for males of 140 to 180 g/L and for females of 120 to 160 g/L (Billett, 1990). The resultant hemoglobin concentration based on these values is 2.3 mM (millimol / L).

Concentration of dissolved oxygen can be calculated using Henry's Law (Equation 7). Where Cp is the concentration of oxygen, α is the solubility coefficient and P_{O2} is the partial pressure of oxygen. The solubility constant has been published in literature (Valabrègue, Aubert, Burger, Bittoun, & Costalat, 2003) as 1.39 x 10^{-3} mM/mmHg. The resultant range of arterial oxygen concentration is presented in Figures 38 and 39.

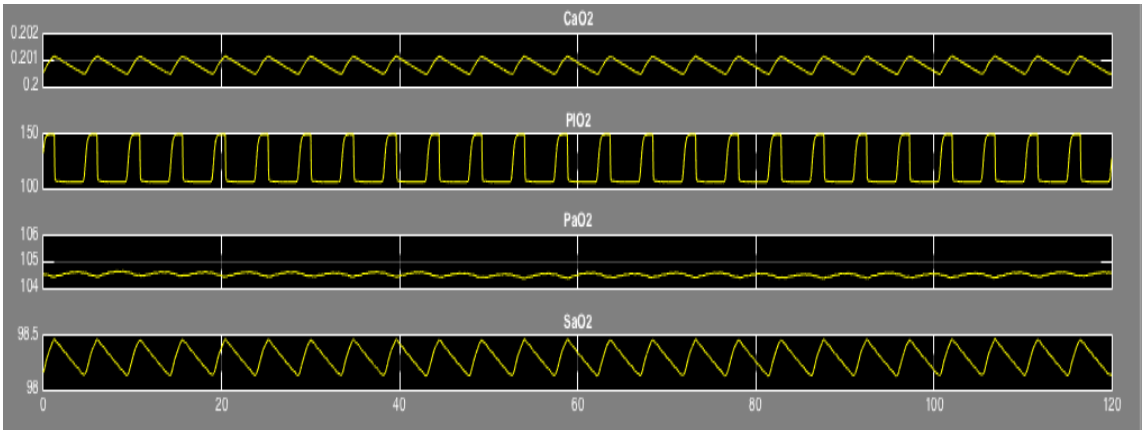

Figure 38. Normoxic breathing at 1 atmosphere (760 mmHg) at t=0. (Pressure of inspired oxygen P_iO_2 150 mmHg). Steady state C_aO_2 is 20.1% (20.1 ml O_2/100ml), S_aO_2 is 98.25% and P_aO_2 is 104.5 mmHg. The resultant oxygen concentration is (2.3 mM x 4 x .9825 + 104.5 mmHg x $1.39x10^{-3}$ mM/mmHg) 9.18 mM

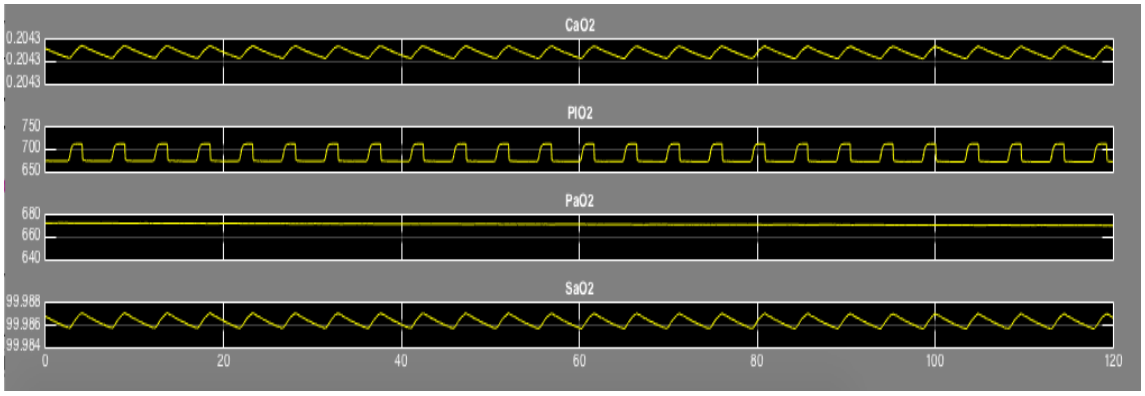

Figure 39. Hyperoxic (100% O_2) breathing at 1 atmosphere (760 mmHg) at t=0. (Pressure of inspired oxygen P_iO_2 713 mmHg). Steady State C_aO_2 is 20.4% (20.4 ml O_2/100ml), S_aO_2 is 99.985% and P_aO_2 is 670 mmHg. The resultant oxygen concentration is (2.3 mmHg x 4 x .99985 + 670 mmHg x $1.39x10^{-3}$ mM/mmHg) 10.13 mM

The oxygen concentration from these simulations may be utilized in a boundary condition (Equation 21) at the basal layer and dermis, coincident with the arterial capillary blood supply. Utilizing the boundary conditions within the epidermis

(Equations 11-15) and oxygen diffusion and consumption relation (Equation 19) an overall oxygen transient gradient may be obtained.

$$C(x_5, dermis) = 9.18 \text{ mM to } 10.13 \text{ mM} \qquad \text{Equation 21}$$

As expected, the presence of hemoglobin allows for a much greater concentration of oxygen versus that from the partial pressure of oxygen dissolved in tissue. In the macroscopic scenario, this results in a reserve of oxygen greater than metabolic requirements for a human at-rest (Lundsgaard, 1919).

The introduction of Michaelis-Menten kinetics into the diffusion approximation results in a non-linear piecewise second-order PDE and a substantial increase in complexity in obtaining a unique analytical solution. Similar solutions have been published in literature (Bassom, Ilchmann, & Voß, 1997) for uniform geometry and without broad applicability. Due to this complexity a numerical solution is pursued for the defined scenarios.

Oxygen concentration gradients were obtained via numerical approximation with Mathematica software with the supplied boundary conditions. An example of this code may be found in Appendix B.3.

Simulations for both thin (.005 cm) and medium (.01 cm) skin thicknesses indicate little variation in the oxygen transient (Figures 40 and 42). It is observed that with the lack of oxygen consumption in the stratum corneum, oxygen concentration transients progress slightly faster. For both simulations a steady state is reached within

seconds. The most significant difference between thin and medium skin thicknesses may be found between the top layers of skin (Figure 41 and 43).

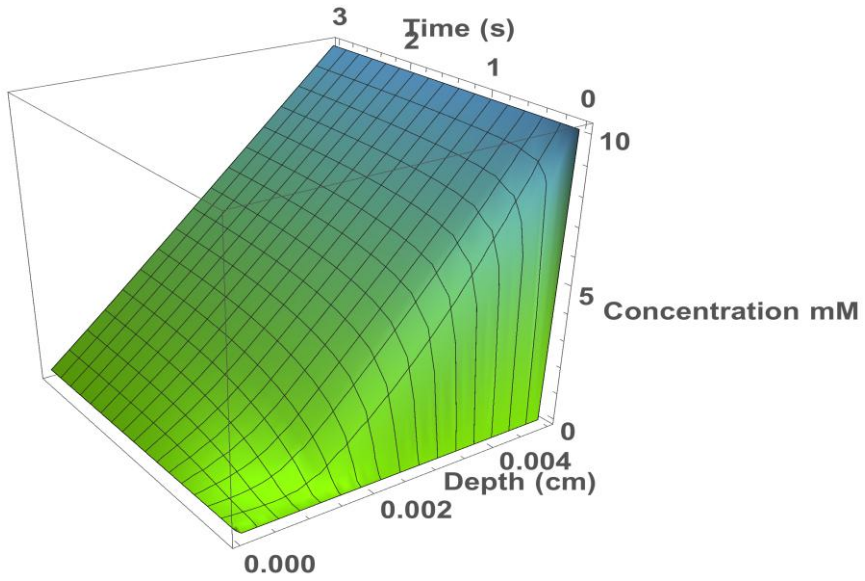

Figure 40. Oxygen concentration gradient from a thin skin surface with 100% oxygen breathing at 1 atmosphere (760 mmHg) from t=0. (Pressure of inspired oxygen P_iO_2 713mmHg)

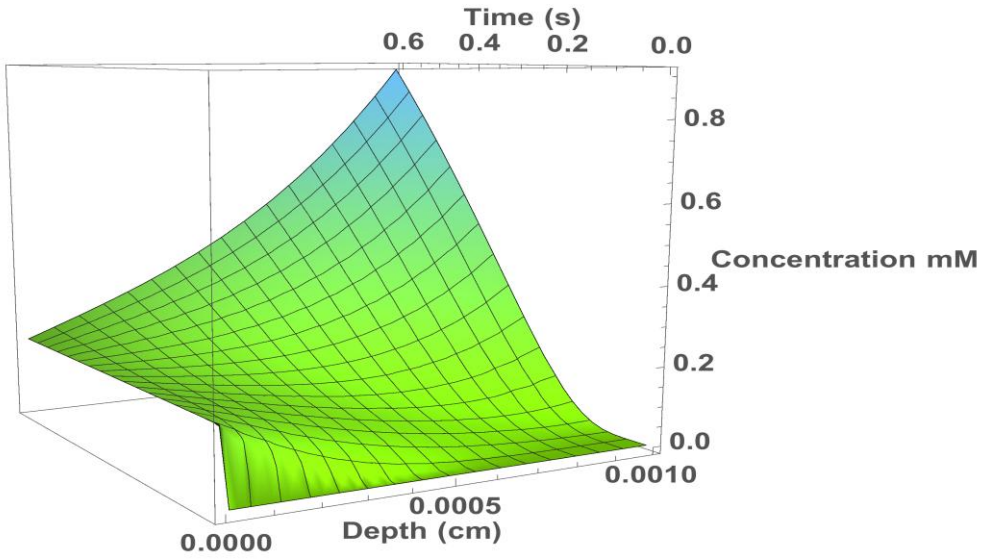

Figure 41. Detailed view of the oxygen concentration gradient from a thin skin surface with 100% oxygen breathing at 1 atmosphere (760 mmHg) from t=0. (Pressure of inspired oxygen P_iO_2 713mmHg)

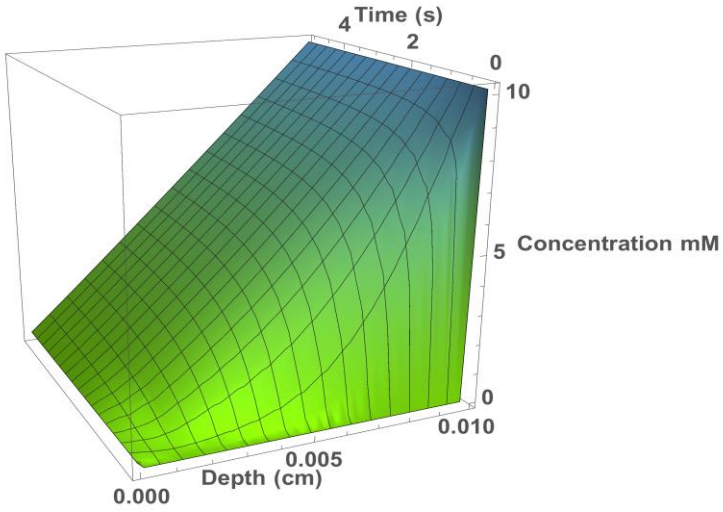

Figure 42. Oxygen concentration gradient from a medium thickness skin surface with 100% oxygen breathing at 1 atmosphere (760 mmHg) from t=0. (Pressure of inspired oxygen P_iO_2 713mmHg)

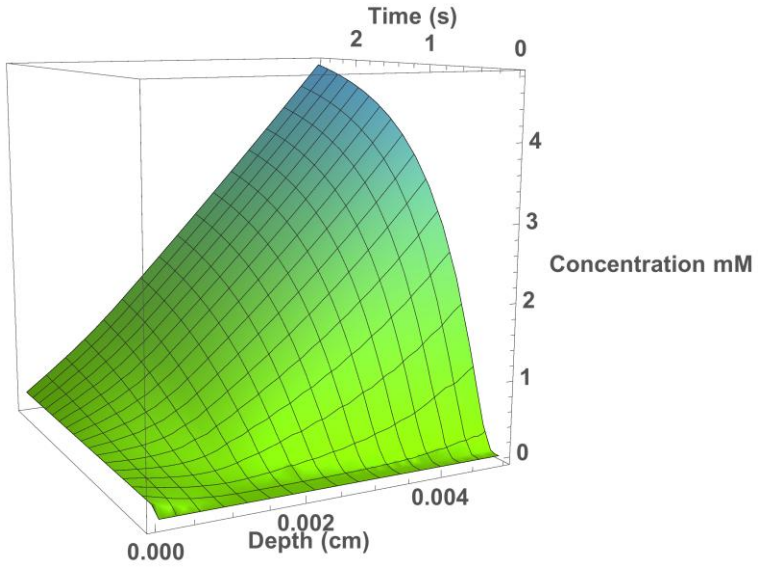

Figure 43. Detailed view of the oxygen concentration gradient from a medium thickness skin surface with 100% oxygen breathing at 1 atmosphere (760 mmHg) from t=0. (Pressure of inspired oxygen P_iO_2 713mmHg)

Consideration of the thickest epidermal layers, such as the soles and palms can be observed to yield a significantly different oxygen concentration gradient. In can be concluded in this anatomy that the significance of oxygen diffusion may be greater due to the greater diffusion distance from the arterial capillary oxygen supply. Boundary condition transients are not observed to reach a steady state until several minutes have elapsed (Figure 44 and 45).

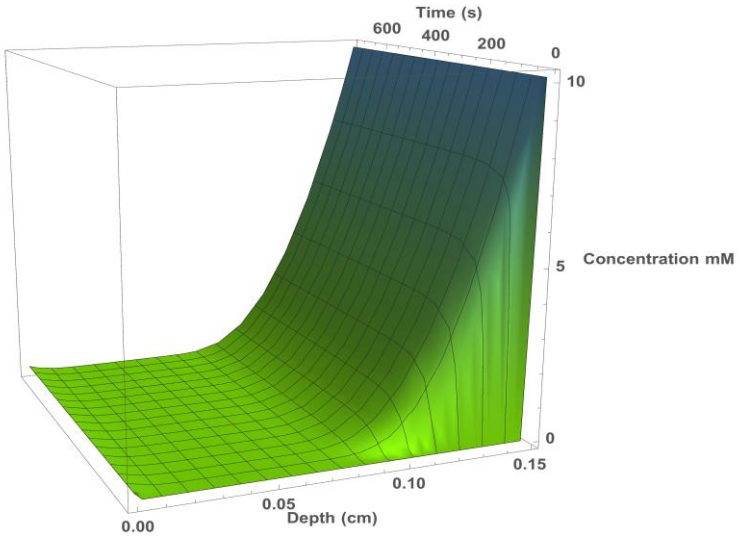

Figure 44. Oxygen tension gradient from a thick skin surface with 100% oxygen breathing at 1 atmosphere (760 mmHg) from t=0. (Pressure of inspired oxygen P_iO_2 713mmHg)

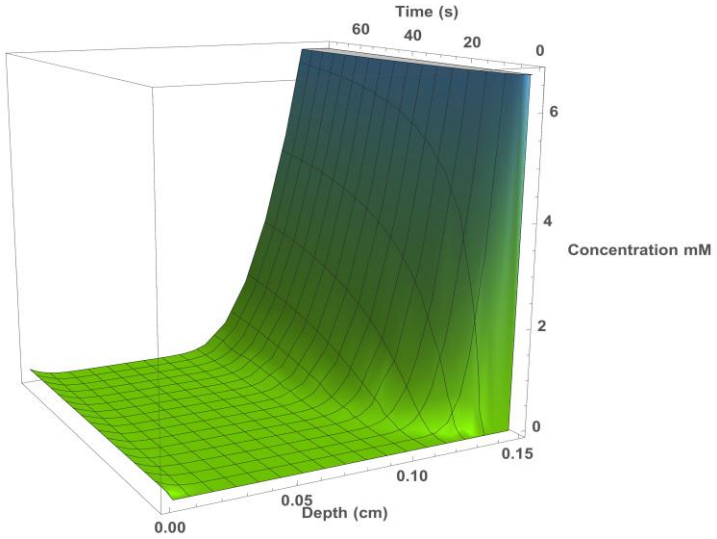

Figure 45. Detailed view of the oxygen tension gradient from a thick skin surface with 100% oxygen breathing at 1 atmosphere (760 mmHg) from t=0. (Pressure of inspired oxygen P_iO_2 713mmHg)

The relatively greater oxygen concentration in deeper skin layers is associated with the high oxygen carrying capacity of hemoglobin. This concentration is about 3-4 times the amount of oxygen required for a resting metabolic state(Lundsgaard, 1919). It additionally enables some brief metabolic exertion prior to the cardiovascular system accommodating a change in oxygen consumption.

The resultant steady-state curves are established in a few seconds for thin and medium epidermal thicknesses and several minutes for thick epidermal thicknesses. The curves are provided in Figure 46.

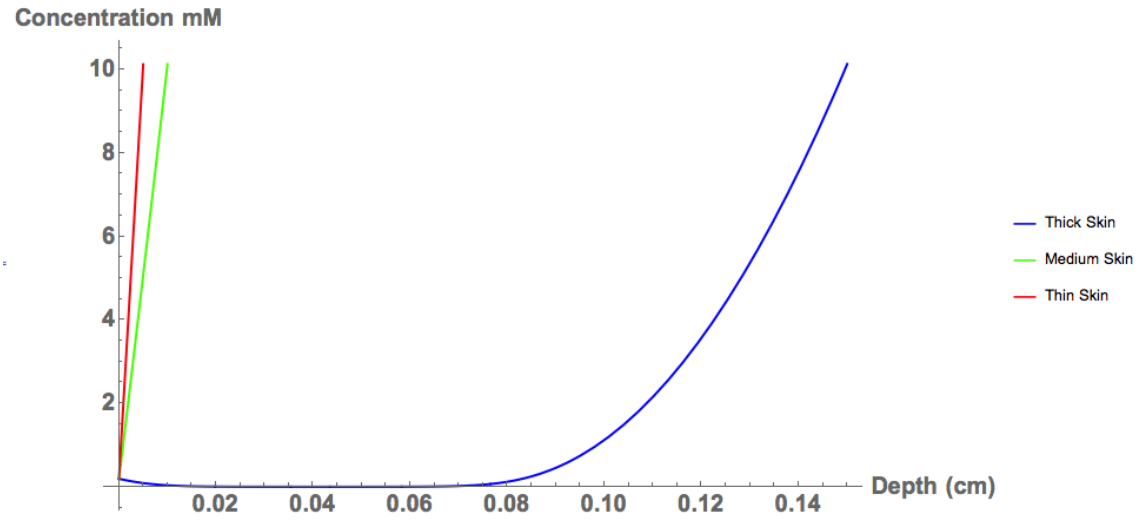

Figure 46. Steady-state oxygen concentration gradient from a thin, thick and thick skin surfaces at 100% oxygen breathing at 1 atmosphere (760 mmHg).

In order to demonstrate the transient from a normoxic environment to a hyperoxic environment as associated with EVA activity the following simulation is provided with a transition from normoxic to hyperoxic environment at t = 540s (Figure 47). This results in a slight increase in concentration values that are more pronounced in the layers of skin closer to the blood oxygen supply.

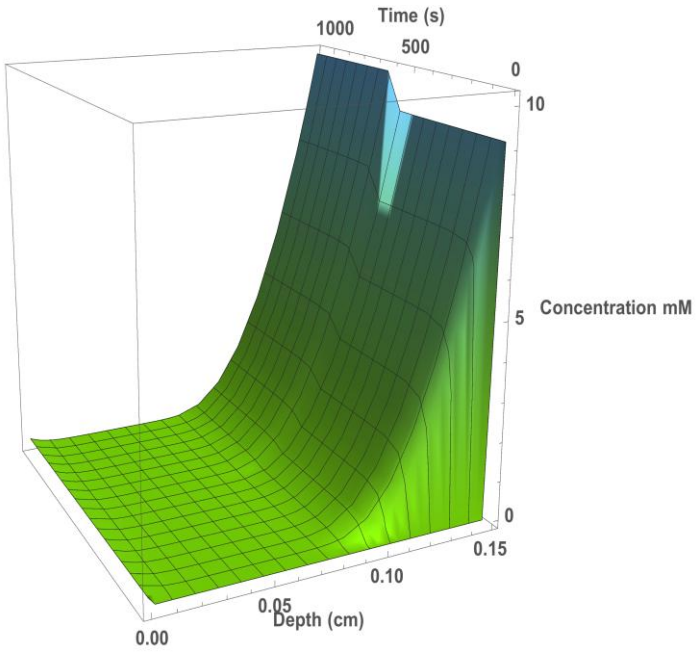

Figure 47. Oxygen concentration gradient from a thick skin surfaces with initial 21% oxygen breathing at 1 atmosphere with a transition to 100% oxygen breathing (760 mmHg, P_IO_2 713 mmHg) at t > 540s.

In order to demonstrate broader application of this diffusion model, an example of terminating arterial blood supply is provided in Figure 48. It can be readily observed

that the removal of hemoglobin bound oxygen supply results in a substantial decrease in oxygen concentration.

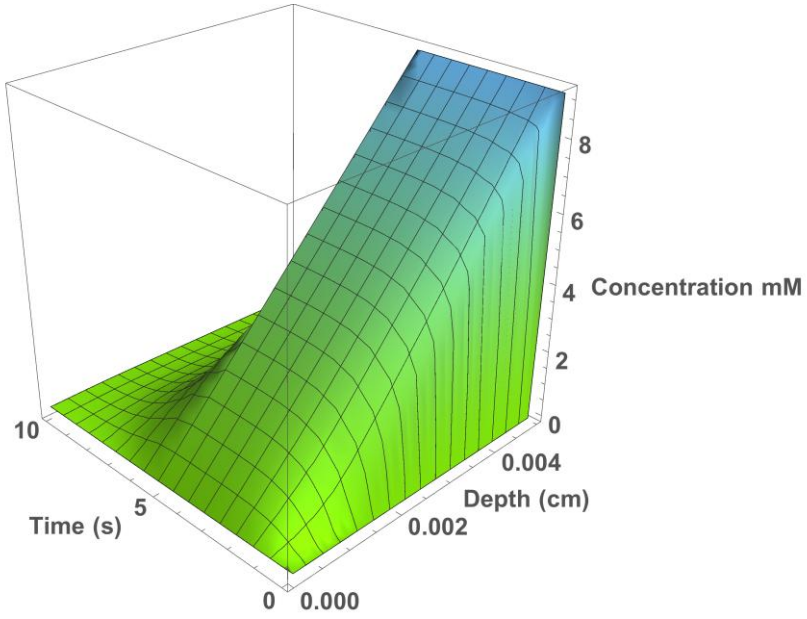

Figure 48. Oxygen concentration gradient from a thin skin surfaces at 21% oxygen breathing at 1 atmosphere (760 mmHg) with a termination of arterial blood oxygen at t > 5 s.

To properly relate the oxygen concentration or solubility in tissue to the MCDS code a correlation is needed in atmospheric content. Using Henry's law again for tissue and associated solubility constant (Table 6) instead of plasma as calculated previously will yield an equivalent atmospheric pressure for tissue. This relationship utilized with the preceding oxygen concentration simulations can be used to reveal that the partial pressure of oxygen in tissue.

4. SUMMARY AND CONCLUSIONS

4.1 Hypoxic Reduction Factor and Resultant Biological Effect

Due to the intended comparison of the RBE for hypoxic versus normoxic tissue, the output of the MCDS code defines and provides a Hypoxic Reduction Factor (HRF) in lieu of OER. OER has been used extensively as a scaling factor with variable oxygen concentrations against a hypoxic condition that may produce trends counter to those associated with a normoxic test environment. The HRF is defined as the ratio of the absorbed dose required to produce biological effect under hypoxic conditions to the absorbed dose required to produce the same effect under normoxic (21% O2 @ 1 atm) conditions. MCDS defines the HRF by Double Strand Break (DSB) induction and can be expressed as a ratio of doses or as ratio of DSB yields

$$HRF_{DSB} = {}^{D_{O_2}}\!/_{D_{Normoxic}} = {}^{\sum DSB_{Normoxic}}\!/_{\sum DSB_{O_2}} \qquad \text{Equation 22}$$

MCDS does not provide for the alteration of normoxic oxygen tension, limiting application for hyperoxic simulation. This is particularly relevant for the skin epidermis that is normally hypoxic and EVA preparation activities where inspired oxygen (P_IO_2) may approach 713 mmHg (100%) at 1 atm. To account for this Relative Biological Effect (RBE) a baseline $HRF_{Skin\text{-}Normoxic}$ trend is produced that is representative of the

oxygen tension profile in the epidermis under atmospheric normoxic conditions (21% O_2, 1 atm). Another HRF can be produced for the representative epidermal oxygen tension profile under atmospheric transient $HRF_{O2\ Skin\text{-}Transient}$ (i.e. 100% O_2, 1 atm). The resultant $RBE_{Skin\text{-}Transient}$ may be produced by dividing the $HRF_{O2\ Skin\text{-}Transient}$ by $HRF_{Skin\text{-}Normoxic}$ as shown in Equation 22.

$$RBE_{Skin-Transient} = \frac{\mathrm{HRF_{O2\ Skin-Transient}}}{\mathrm{HRF_{Skin-Normoxic}}} \qquad \text{Equation 23}$$

The resulting flux averaged HRFs for all SPEs and shielding vs environmental oxygen partial pressure is presented in Figure 49.

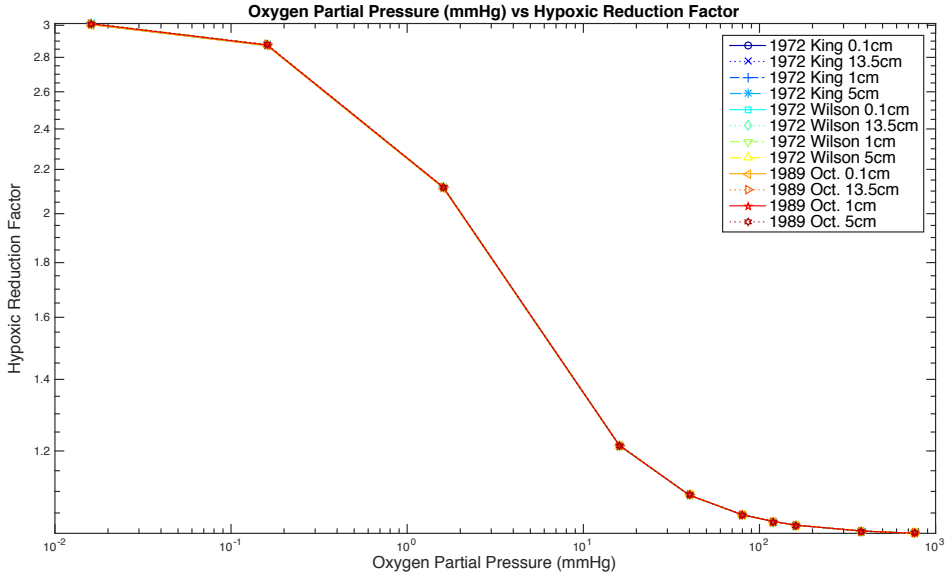

Figure 49. Flux-averaged HRFs for all SPEs and shielding thicknesses versus oxygen partial pressure present in tissue.

The resulting averaged HRFs for all simulated runs resulted in only minimal differences between all SPEs and vehicle shielding. As expected, a strong dependence on oxygen content is present. Under further examination slight differences due to SPE and shielding amount may be found (Figure 50 and 51). This is largely due to the continuous weighting towards proton flux despite significant contributions from secondary radiations including particle fragments and delta rays.

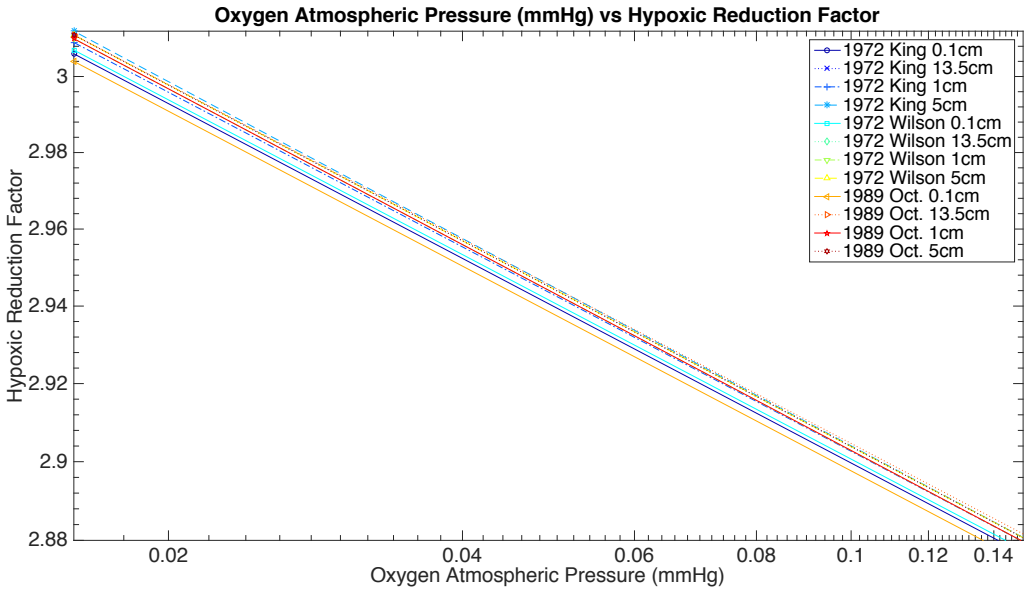

Figure 50. Exploded view of flux-averaged HRFs for all SPEs and shielding thicknesses versus oxygen partial pressure.

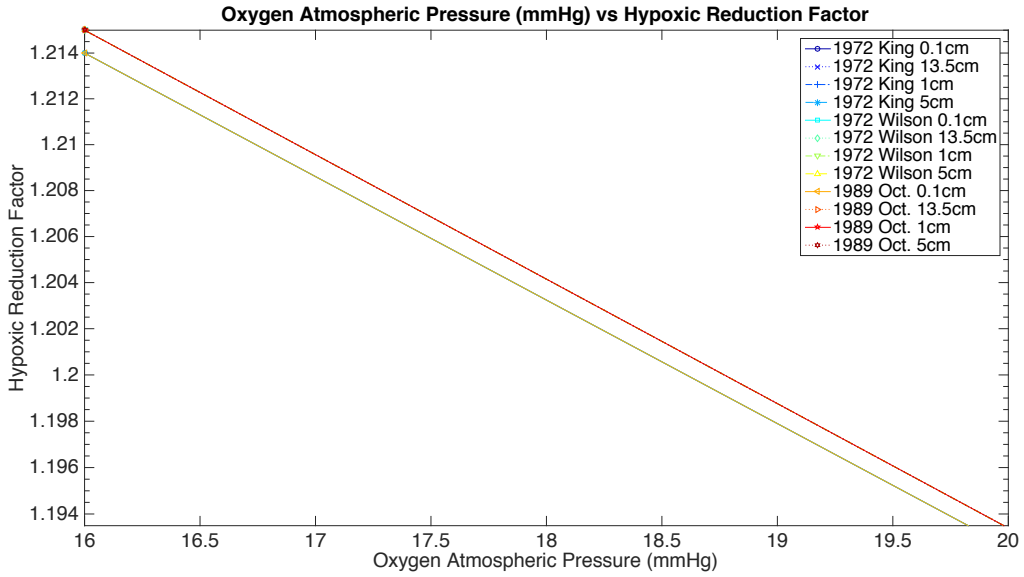

Figure 51. Exploded view of flux-averaged HRFs for all SPEs and shielding thicknesses versus oxygen partial pressure.

The MCDS code utilizes atmospheric oxygen content as correlated to *in vitro* cellular studies and not tissue concentration directly. Taking into account the preceding section on oxygen concentration to tissue and correlating this to equivalent atmospheric oxygen pressure simply using Henry's Law a correlation can be made.

In the normoxic environment simulation (21% O_2 at 1 atmosphere), thin and medium epidermal skin thicknesses produce HRFs near unity that ranges between .91 and 1.02 (Figure 52). The stratum corneum, which has no oxygen consumption and is composed of non-proliferating cells, shows a significant hypoxia driven HRF up to 1.02. Conversely, the interior epidermis produces HRFs slightly less than 1 indicating more oxygen abundance than at a normoxic atmospheric. With the exception of the stratum

corneum, this is indicative that hemoglobin arterial supply provides more oxygen concentration in these tissues than a standard *in vitro* normoxic cell culture. Proper significance of the HRF in the stratum corneum, which has largely negligible susceptibility to DSB detriment, needs more radiobiology studies that perhaps tie in bystander effects and incorporate immune system response.

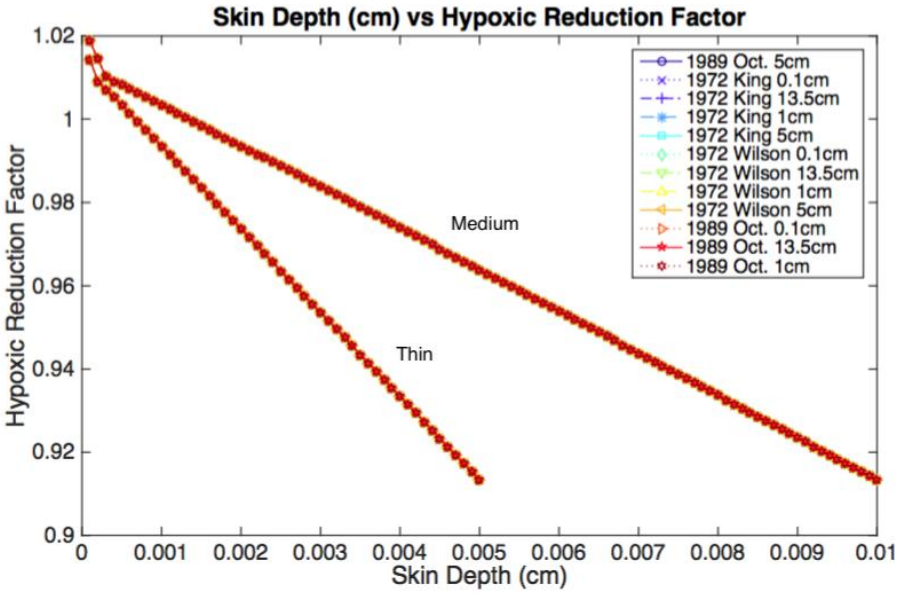

Figure 52. HRF gradient for thin and medium thickness epidermal skin under normoxic (21% O_2 at 1 atmosphere) conditions.

The thick epidermal layers provide a significantly different normoxic HRF trend (Figure 53). The much greater diffusion depth associated with these thick layers creates a significant hypoxia away from atmospheric and arterial oxygen supply. As expected, the HRFs near the atmosphere (stratum corneum) and arterial supply (basal layer) are

near unity. However, a strong hypoxia remains in the stratum spinosum and stratum granulosom.

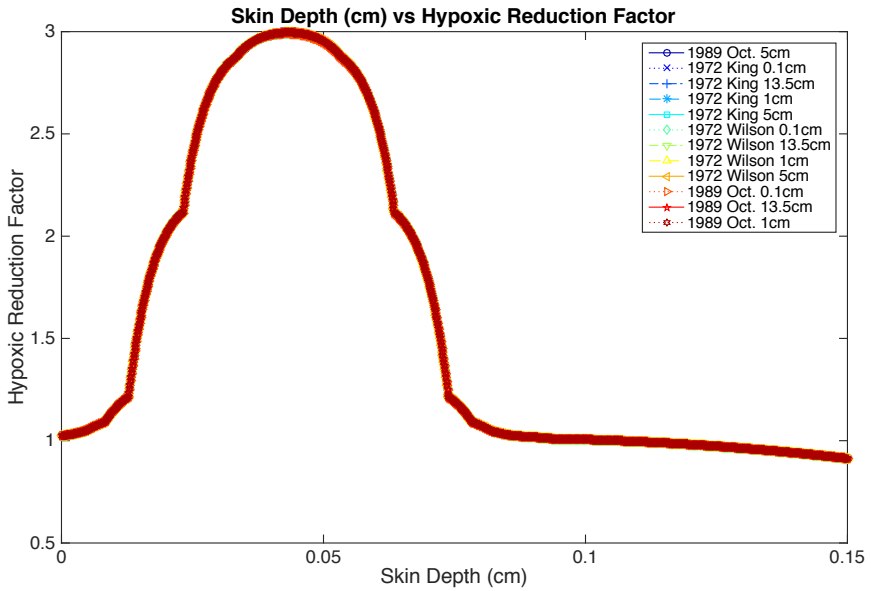

Figure 53. HRF gradient for thick epidermal skin under normoxic (21% O_2 at 1 atmosphere) conditions.

Hyperoxic simulations (100% O_2 at 1 atmosphere) provide similar trends yet at slightly lesser magnitudes of HRF (Figures 54). It is significant to note that this difference is very pronounced in the normally hypoxic stratum spinosum and stratum granulosom thick epidermal sizes (Figure 55).

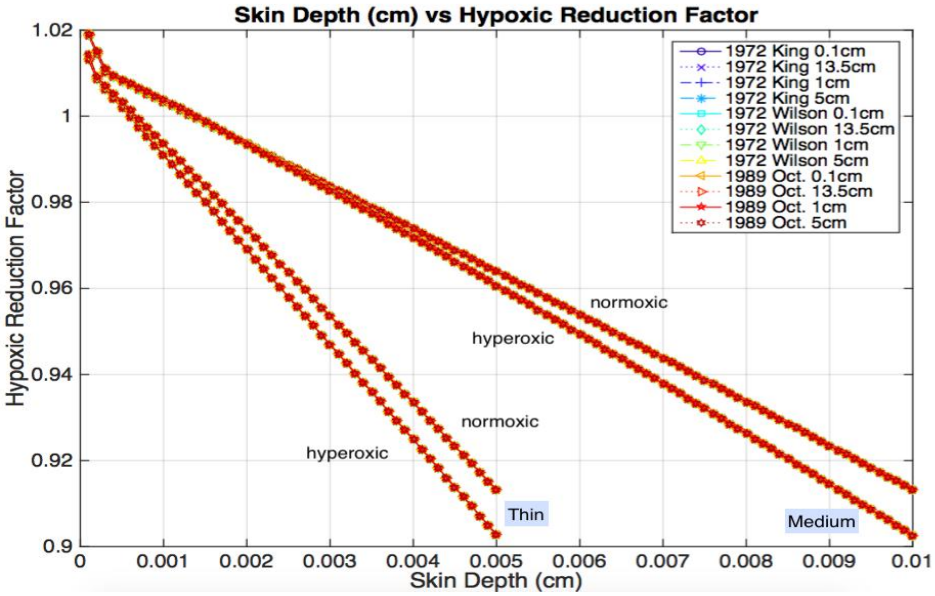

Figure 54. HRF comparison gradient between normoxic and hyperoxic conditions for thin and medium thickness epidermal skin.

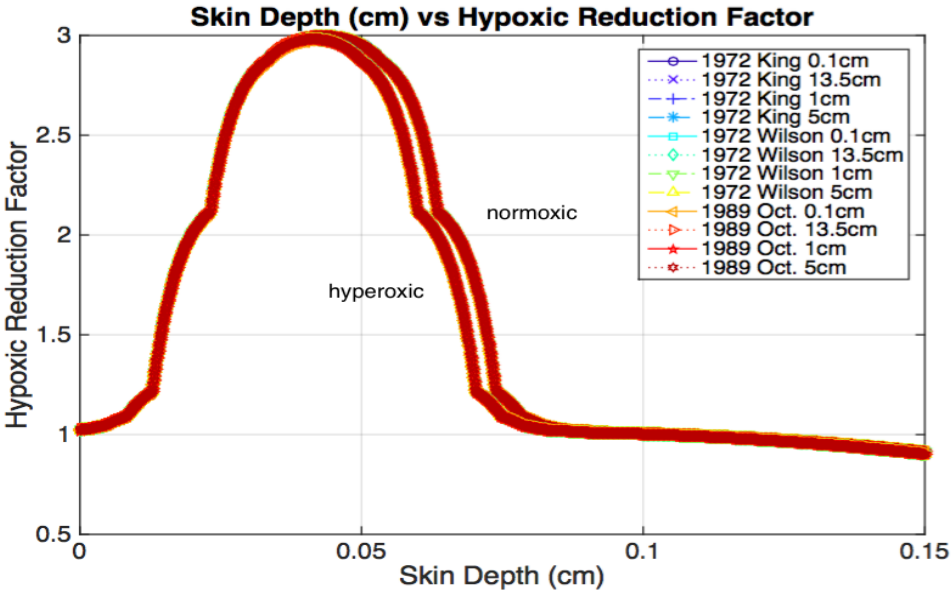

Figure 55. HRF comparison gradient between normoxic and hyperoxic conditions for thick epidermal skin.

The previously defined $RBE_{skin\text{-}transient}$ provides a method for quantification of this change in RBE. For thin epidermal skin simulations, $RBE_{skin\text{-}transient}$ is below 1 and decreases down to .988 near the arterial blood supply. In medium epidermal skin thicknesses, $RBE_{skin\text{-}transient}$ is above 1 in the stratum corneum but decreases below 1 towards .98 near the arterial blood supply (Figure 56). Overall, the smaller thicknesses in the thin and medium sized epidermal simulation do not allow for high amount diffusion and thus limit the effect any environmental oxygen transient.

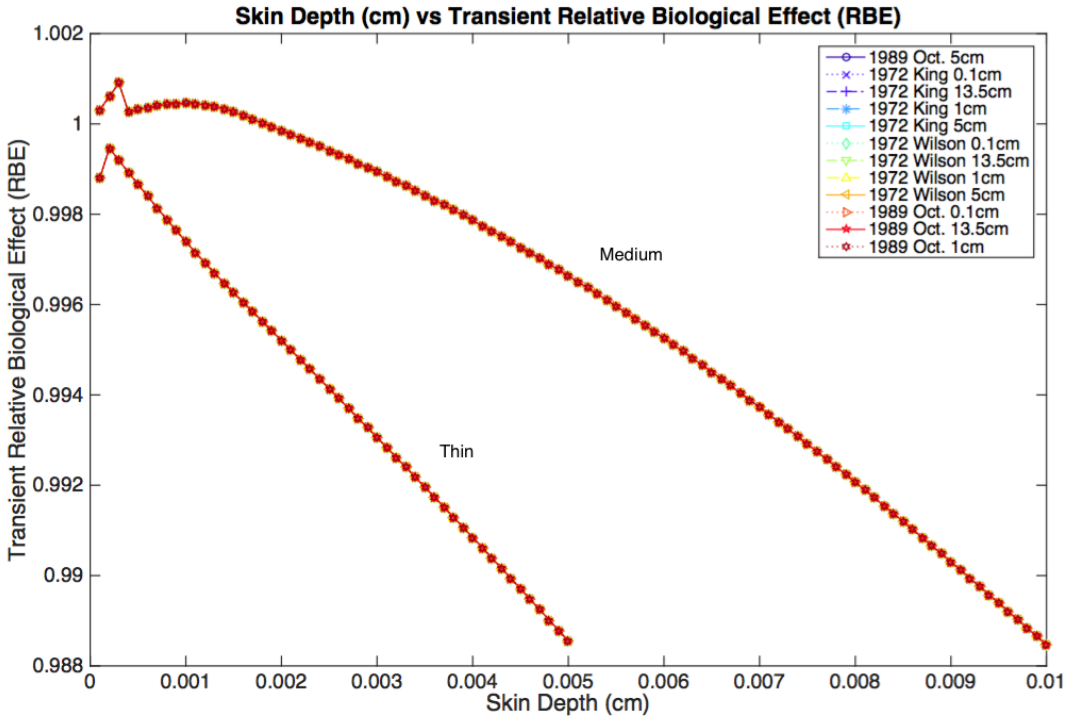

Figure 56. Transient Relative Biological Effect ($RBE_{skin\text{-}transient}$) for thin and medium thickness epidermal skin.

In the thick epidermal simulation diffusion is significant as previously indicated hypoxic trends illustrate. The $RBE_{skin\text{-}transient}$ has its greatest significance in these hypoxic regions of the stratum spinosum and stratum granulosom (Figure 57).

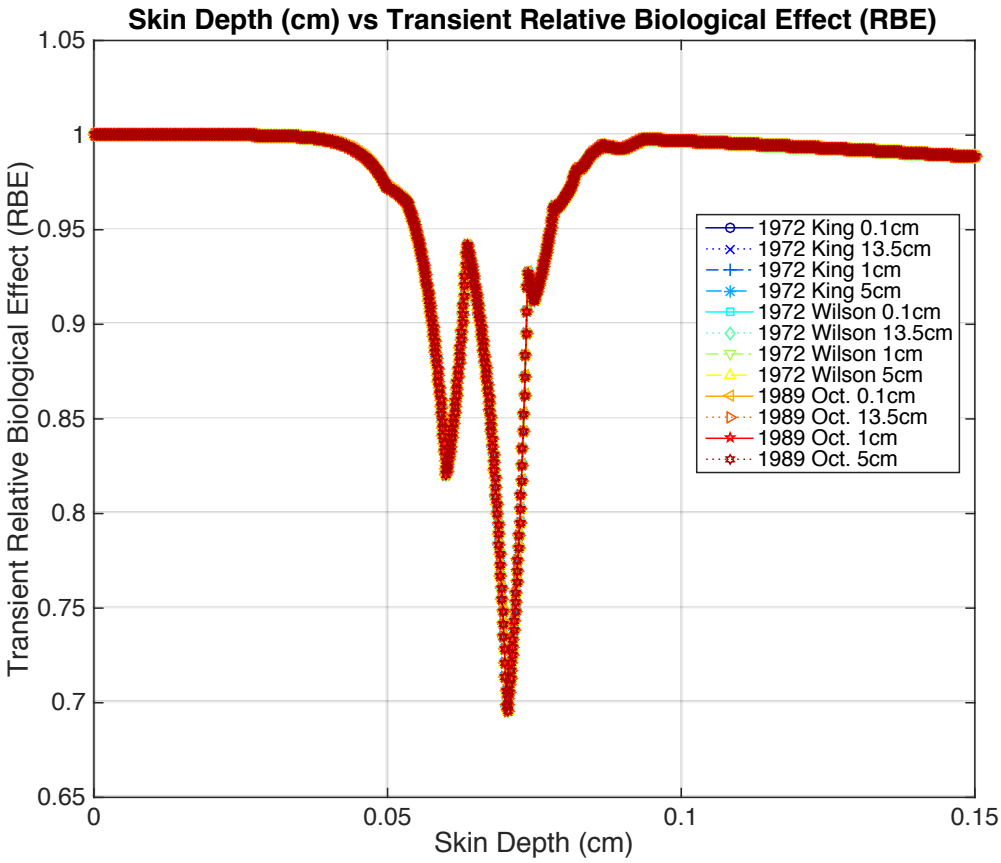

Figure 57. Transient Relative Biological Effect ($RBE_{transient}$) for thick epidermal skin.

The overall results of these simulations indicate that hypoxic areas (relative to in-vitro cell culture) are most affected by oxygen environment transients. However, the

significance of this occurrence is limited primary to the thickest epidermal skin surfaces such as the sole and palm.

4.2 Discussion and Relevance for Space Mission Architecture

The normally prevalent hypoxia in the epidermis results in decreased RBE relative to normoxic tissue, but is modifiable in certain anatomy in this model through oxygen variation in spaceflight. The significance of this modification appears to be limited only to the most hypoxic skin tissues that are the thickest and subsequently have the greatest amounts of diffusion. Consequently, the broad application to skin dosimetry has minimal RBE.

All amounts of spacecraft shielding do not appear to result in significant modification in RBE and oxygen dependence due to shift in spectral LET. Further investigation with high-energy GCR may provide some significance due to a more significant secondary radiation contribution.

Investigation with alternative anatomy may prove significant for space architecture, particularly in tissues with minimal vasculature or have significant variation in hemoglobin content. For example, the cerebral regions of the brain for example are known to contain about 2/3 less hematocrit than the arterial blood supply (Wyatt et al., 1990). This is conjunction with ongoing research about Central Nervous System (CNS) effects from GCR (NCRP, 2006) could prove very significant.

4.3 Future Work and Additional Applications

This model simulates DSB incidence and applies equal significance to all of the skin cell layers presented. However, this is not accurate since it is known rapidly proliferating epidermal stem cells occupy the basal layer, a host of lymphocytes and other immune cells often penetrate the epidermal layers in response to inflammation and serve as significant modifiers of RBE. Modification of this model to produce RBE that utilizes tissue dependent cellular kinetics, inclusive of immune response is a potential pursuit. Numerous studies (Cengel, Diffenderfer, Avery, Kennedy, & McDonough, 2010; Shaowen Hu & Cucinotta, 2012; S. Hu et al., 2009; Jenine K. Sanzari et al., 2015; J. K. Sanzari et al., 2013; J. M. Wilson et al., 2011; Zhou et al., 2014) have already examined the cellular kinetics of SPEs to skin. Due to the presence of immune cells in the epidermis the skin is recognized as a marker for Acute Radiation Syndrome (ARS) particularly where the hematopoietic system is of concern.

In medical applications, this model may serve to predict the appropriateness of dose in radiotherapy where hypoxia is a concern and oxygen prescription is administered. Additionally, it may be utilized as an aid to verification oxygen content with medical imaging modalities such as F-MRI, Blood Oxygen Level Dependent (BOLD) MRI or Dynamic Contrast Enhances (DCE) MRI.

In the low dose application, there is greater difficulty in establishing correlation between stochastic effects to skin and ionizing radiation exposure. A long-term study (Roy E. Shore, Albert, Reed, Harley, & Pasternack, 1984; R. E. Shore et al., 2002)

correlated 100 kVp x-rays to the scalp with increased incidence of basal cell carcinoma (BCC) with minimal correlation to squamous cell carcinoma (SCC) and indistinguishable attribution to melanoma. However, studies from (Fink & Bates, 2005) suggest a positive correlation between ionizing radiation and melanoma risk. The discrepancies in correlation lay in part to the large individual variations in ultraviolet sunlight exposure and melanin content among other radiosensitivity factors and the commonly unreported incidence of the largely non-fatal BCC and SCC. Although melanoma is the least prevalent form of skin originating cancer, it has the highest probability of metastasis and 75% of the attributable fatalities from skin cancer (Jerant, Johnson, Sheridan, & Caffrey, 2000). Reflecting the combined low mortality rate of SCC and BCC the International Council on Radiation Protection (ICRP) publication 60 and 103 (ICRP, 2007) recommend a relatively low normalized radiation-weighting factor of .01 to skin.

REFERENCES

Aghara, S. K., Sriprisan, S. I., Singleterry, R. C., & Sato, T. (2015). Shielding evaluation for solar particle events using MCNPX, PHITS and OLTARIS codes. *Life Sciences in Space Research, 4*(0), 79-91. doi:http://dx.doi.org/10.1016/j.lssr.2014.12.003

Alper, T., & Howard-Flanders, P. (1956). Role of oxygen in modifying the radiosensitivity of E. coli B. *Nature, 178*(4540), 978-979.

Atwell, W., Tylka, A., Dietrich, W., Badavi, F., & Rojdev, K. (2011). Spectral Analyses and Radiation Exposures from Several Ground-Level Enhancement (GLE) Solar Proton Events: A Comparison of Methodologies *41st International Conference on Environmental Systems*: American Institute of Aeronautics and Astronautics.

Atwell, W., Tylka, A. J., Dietrich, W. F., & Badavi, F. (2008). *Radiation exposure estimates from extremely energetic solar proton events*. Paper presented at the COSPAR Scientific Assembly, Montréal, Canada.

Banno, T., Gazel, A., & Blumenberg, M. (2004). Effects of Tumor Necrosis Factor-α (TNFα) in Epidermal Keratinocytes Revealed Using Global Transcriptional Profilin. *Journal of Biological Chemistry, 270*, 32633-32642.

Bassom, A. P., Ilchmann, A., & Voß, H. (1997). Oxygen Diffusion in Tissue Preparations with Michaelis–Menten Kinetics. *Journal of Theoretical Biology*. doi:10.1006/jtbi.1996.0298

Benton, E. R., Benton, E. V., & Frank, A. L. (2001). *Characterization of the Radiation Shielding Properties of US andRussian EVA Suits* (LBNL--48977; R&D Project: 43GU01; TRN: US200713%%339). Retrieved from http://www.osti.gov/bridge/servlets/purl/901218-m5UuJ1/

Billett, H. H. (1990). Hemoglobin and Hematocrit. In H. K. Walker, H. W.D., & J. W. Hurst (Eds.), *Clinical Methods: The History, Physical, and Laboratory Examinations*. (3 ed.).

Bingmann, D., & Kolde, G. (1982). PO2-profiles in hippocampal slices of the guinea pig. *Experimental Brain Research, 48*(1), 89-96. doi:10.1007/BF00239575

Carlson, D. J., Stewart, R. D., Semenenko, V. A., & Sandison, G. A. (2008). Combined use of Monte Carlo DNA damage simulations and deterministic repair models to examine putative mechanisms of cell killing. *Radiat Res, 169*(4), 447-459. doi:10.1667/RR1046.1

Cengel, K. A., Diffenderfer, E. S., Avery, S., Kennedy, A. R., & McDonough, J. (2010). Using electron beam radiation to simulate the dose distribution for whole body solar particle event proton exposure. *Radiation and Environmental Biophysics, 49*(4), 715-721. doi:10.1007/s00411-010-0315-z

Cheng, L., Ivanova, O., Fan, H.-H., & Khoo, M. C. K. (2010). An integrative model of respiratory and cardiovascular control in sleep-disordered breathing. *Respiratory physiology & neurobiology, 174*(1-2), 4-28. doi:10.1016/j.resp.2010.06.001

Costes, S. V., Ponomarev, A., Chen, J. L., Nguyen, D., Cucinotta, F. A., & Barcellos-Hoff, M. H. (2007). Image-Based Modeling Reveals Dynamic Redistribution of DNA Damage into Nuclear Sub-Domains. *PLoS Comput Biol, 3*(8), e155. doi:10.1371/journal.pcbi.0030155

Dorman, L. I., & Venkatesan, D. (1993). Solar cosmic rays. *Space Science Reviews, 64*(3-4), 183-362. doi:10.1007/BF00750737

Evans, N. T., & Naylor, P. F. (1967). The systemic oxygen supply to the surface of human skin. *Respir Physiol, 3*(1), 21-37. doi:10.1016/0034-5687(67)90020-5

FDA. (1994). *Avoidance of Serious X-Ray-Induced Skin Injuries to Patients During Fluoroscopically-guided Procedures*. Retrieved from http://www.fda.gov/downloads/Radiation-EmittingProducts/RadiationEmittingProductsandProcedures/MedicalImaging/MedicalX-Rays/UCM116677.pdf

Fink, C. A., & Bates, M. N. (2005). Melanoma and Ionizing Radiation: Is There a Causal Relationship? *Radiation Research, 164*(5), 701-710.

Fournier, R. L. (2007). *Basic transport phenomena in biomedical engineering*. New York: Taylor & Francis.

Gray, L. H., Conger, A. D., Ebert, M., Hornsey, S., & Scott, O. C. A. (1953). The Concentration of Oxygen Dissolved in Tissues at the Time of Irradiation as a Factor in Radiotherapy. *The British Journal of Radiology, 26*(312), 638-648. doi:10.1259/0007-1285-26-312-638

Grossmann, U. (1982). Simulation of combined transfer of oxygen and heat through the skin using a capillary-loop model. *Mathematical Biosciences, 61*(2), 205-236. doi:http://dx.doi.org/10.1016/0025-5564(82)90004-9

Hall, E. J. (2006). *Radiobiology for the radiologist* (6th ed.). Hagerstown, Md.: Medical Dept., Harper & Row.

Halperin, E. C., Perez, C. A., & Brady, L. W. (2008). *Perez and Brady's principles and practice of radiation oncology*. Philadelphia: Wolters Kluwer Health/Lippincott Williams & Wilkins.

Harada, T., Kubo, H., Mori, T., & Sato, T. (2005). *Pulmonary and cardiovascular integrated model controlled with oxygen consumption* (Vol. 1).

Hauptner, A., Friedland, W., Dietzel, S., Drexler, G. A., Greubel, C., Hable, V., . . . Dollinger, G. (2006). Spatial distribution of DNA double strand breaks from ion tracks. *Mat Fys Medd Dan Vid Selsk, 52*, 59-85.

Heinbockel, J. H., Slaba, T. C., Blattnig, S. R., & Tripathi, R. K. (2010). Comparison of the transport codes HZETRN, HETC and FLUKA for a solar particle event. *Advances in Space Research, 47*(6), 1079-1088.

Hirshfeld, J. W., Jr., Balter, S., Brinker, J. A., Kern, M. J., Klein, L. W., Lindsay, B. D., . . . American College of, P. (2004). ACCF/AHA/HRS/SCAI clinical competence statement on physician knowledge to optimize patient safety and image quality in fluoroscopically guided invasive cardiovascular procedures. A report of the American College of Cardiology Foundation/American Heart Association/American College of Physicians Task Force on Clinical Competence and Training. *J Am Coll Cardiol, 44*(11), 2259-2282. doi:10.1016/j.jacc.2004.10.014

Hsing-Hua, F., & Khoo, M. C. K. (2002, 2002). *PNEUMA - a comprehensive cardiorespiratory model*. Paper presented at the Engineering in Medicine and Biology, 2002. 24th Annual Conference and the Annual Fall Meeting of the Biomedical Engineering Society EMBS/BMES Conference, 2002. Proceedings of the Second Joint.

Hu, S., & Cucinotta, F. A. (2012). A Multiscale Computational Model of the Response of Swine Epidermis after Acute Irradiation. Retrieved from http://ntrs.nasa.gov/archive/nasa/casi.ntrs.nasa.gov/20130000604.pdf

Hu, S., Kim, M. H., McClellan, G. E., & Cucinotta, F. A. (2009). Modeling the acute health effects of astronauts from exposure to large solar particle events. *Health Phys, 96*(4), 465-476. doi:10.1097/01.HP.0000339020.92837.61

Huch, R., & Lubbers, D. (1981). *Transcutaneous PO2*. New York: Thieme-Stratton.

Huntoon, C. S. L. (1996). *Humans in spaceflight*. [S.l.]: [s.n.].

ICRP. (2007). The 2007 Recommendations of the International Commission on Radiological Protection. ICRP publication 103 *Annals of the ICRP* (Vol. 37, pp. 2-4).

ICRP. (2010). *Avoidance of Radiation Injuries from Medical Interventional Procedures, Publication 85*. Retrieved from

Jerant, A. F., Johnson, J. T., Sheridan, C. D., & Caffrey, T. J. (2000). Early detection and treatment of skin cancer. *Am Fam Physician, 62*(2), 357-368, 375-356, 381-352.

Kim, M.-H. Y., De Angelis, G., & Cucinotta, F. A. (2011). Probabilistic assessment of radiation risk for astronauts in space missions. *Acta Astronautica, 68*(7-8), 747-759. doi:10.1016/j.actaastro.2010.08.035

Kim, M.-H. Y., George, K. A., & Cucinotta, F. A. (2006). Evaluation of skin cancer risk for lunar and Mars missions. *Advances in Space Research, 37*(9), 1798-1803. doi:10.1016/j.asr.2006.03.032

King, J. H. (1974). Solar Proton Fluences for 1977-1983 Space Missions. *Journal of Spacecraft and Rockets, 11*(6), 401-408. doi:10.2514/3.62088

Koenig, T. R., Mettler, F. A., & Wagner, L. K. (2001). Skin injuries from fluoroscopically guided procedures: part 2, review of 73 cases and recommendations for minimizing dose delivered to patient. *AJR Am J Roentgenol, 177*(1), 13-20. doi:10.2214/ajr.177.1.1770013

Lin, Z. W., Adams, J. H., Barghouty, A. F., Randeniya, S. D., Tripathi, R. K., Watts, J. W., & Yepes, P. P. (2012). Comparisons of several transport models in their predictions in typical space radiation environments. *Advances in Space Research, 49*(4), 797-806. doi:10.1016/j.asr.2011.11.025

Lundsgaard, C. (1919). STUDIES OF OXYGEN IN THE VENOUS BLOOD : V. DETERMINATIONS ON PATIENTS WITH ANEMIA. *The Journal of Experimental Medicine, 30*(2), 147-158.

Malitson, H., & Webber, W. R. (1963). Characteristics of solar cosmic ray events and correlation with solar flare data: NASA Goddard Space Flight Center.

Mananas, M. A., Hernandez, A. M., Romero, S., Grino, R., Rabinovich, R., Benito, S., & Caminal, P. (2003, 17-21 Sept. 2003). *Analysis of respiratory models at different levels of exercise, hypercapnia and hypoxia*. Paper presented at the Engineering in Medicine and Biology Society, 2003. Proceedings of the 25th Annual International Conference of the IEEE.

Masunaga, S., Hirayama, R., Uzawa, A., Kashino, G., Suzuki, M., Kinashi, Y., . . . Ono, K. (2009). The effect of post-irradiation tumor oxygenation status on recovery from radiation-induced damage in vivo: with reference to that in quiescent cell populations. *J Cancer Res Clin Oncol, 135*(8), 1109-1116. doi:10.1007/s00432-009-0552-1

McGoron, A. J., Nair, P., & Schubert, R. W. (1997). Michaelis-Menten kinetics model of oxygen consumption by rat brain slices following hypoxia. *Annals of Biomedical Engineering, 25*(3), 565-572.

Mewaldt, R. A. (2005). Solar-Particle Energy Spectra during the Large Events of October-November 2003 and January 2005.

Mewaldt, R. A. (2007). Radiation risks from large solar energetic particle events. Retrieved from

Michael, B. D., & Prise, K. M. (1996). A multiple-radical model for radiation action on DNA and the dependence of OER on LET. *Int J Radiat Biol, 69*(3), 351-358.

NCRP. (2006). *Information Needed to Make Radiation Protection Recommendations for Space Missions Beyond Low-Earth Orbit*. Retrieved from Bethesda, Md:

NCRP. (2011). *NCRP Report No. 168, Radiation Dose Management for Fluoroscopically-Guided Interventional Medical Procedures* (9781441686947 1441686940). Retrieved from Bethesda, Md.: http://site.ebrary.com/id/10452175

Oh, J., & Lee, H.-S. (2011). Comparison of the FLUKA, MCNPX, and PHITS Codes in Yield Calculation of Secondary Particles Produced by Intermediate Energy Proton Beam. *Progress in NUCLEAR SCIENCE and TECHNOLOGY, 1*, 85-88.

Ohara, K. (1951). Studies on the oxygen consumption of human skin tissues, with special reference to that of sweat glands. *JAPANESE JOURNAL OF PHYSIOLOGY, 2*(1), 1-8.

Parsons, J. L., & Townsend, L. W. (2000). Interplanetary crew dose rates for the August 1972 solar particle event. *Radiat Res, 153*(6), 729-733.

Peter, R. U. (2005). Cutaneous radiation syndrome in multi-organ failure. *BJR Suppl, 27*(1), 180-184. doi:10.1259/bjr/56925969

Radiation and the International Space Station: Recommendations to Reduce Risk. (2000). Retrieved from http://www.nap.edu/openbook.php?record_id=9725

RD Vann, W. G., MJ Natoli , NW Pollock , BD Butler , CE Fife , E Beltran , RE Nishi , PA Sullivan , AA Pilmanis , J Conkin , PP Foster , D Hamilton , K Acock , KC Loftin , JM Waligora , SM Schneider , CE Ross , MR Powell , JP Dervay, AH Feiveson, ML Gernhardt. DESIGN, TRIALS, AND CONTINGENCY PLANS FOR EXTRAVEHICULAR ACTIVITY FROM THE INTERNATIONAL SPACE STATION. Retrieved from http://www.dsls.usra.edu/meetings/bio2001/pdf/133.pdf

Roszinski, S., & Schmeller, W. (1995). Differences between intracutaneous and transcutaneous skin oxygen tension in chronic venous insufficiency. *Journal of Cardiovascular Surgery, 36*(4), 407-413.

Sanzari, J. K., Diffenderfer, E. S., Hagan, S., Billings, P. C., Gridley, D. S., Seykora, J. T., . . . Cengel, K. A. (2015). Dermatopathology effects of simulated solar particle event radiation exposure in the porcine model. *Life Sciences in Space Research, 6*, 21-28. doi:http://dx.doi.org/10.1016/j.lssr.2015.06.003

Sanzari, J. K., Wan, X. S., Wroe, A. J., Rightnar, S., Cengel, K. A., Diffenderfer, E. S., . . . Kennedy, A. R. (2013). Acute Hematological Effects of Solar Particle Event Proton Radiation in the Porcine Model. *Radiation Research, 180*(1), 7-16. doi:10.1667/RR3027.1

Sato, T., & Niita, K. (2006). Analytical Functions of Predict Cosmic-Ray Neutron Spectra in the Atomsphere. *Radiation Research, 166*(3), 544-555. doi:10.1667

Sato, T., Niita, K., Matsuda, N., Hashimoto, S., Iwamoto, Y., Noda, S., . . . Sihver, L. (2013). Particle and Heavy Ion Transport Code System PHITS, Version 2.52. *J. Nucl. Sci. Technol.*

Sauer, H. H. (1990). *Summary Data for the Solar Energetic Particle Events of August Through December 1989*. Retrieved from

Shmukler, M. (2004). Density of Blood. Retrieved from http://hypertextbook.com/facts/2004/MichaelShmukler.shtml

Shore, R. E., Albert, R. E., Reed, M., Harley, N., & Pasternack, B. S. (1984). Skin Cancer Incidence among Children Irradiated for Ringworm of the Scalp. *Radiation Research, 100*(1), 192-204.

Shore, R. E., Moseson, M., Xue, X., Tse, Y., Harley, N., & Pasternack, B. S. (2002). Skin cancer after X-ray treatment for scalp ringworm. *Radiat Res, 157*(4), 410-418.

Siggaard-Andersen, O., Wimberley, P. D., Göthgen, I., & Siggaard-Andersen, M. (1984). A mathematical model of the hemoglobin-oxygen dissociation curve of human blood and of the oxygen partial pressure as a function of temperature. *Clinical Chemistry, 30*(10), 1646-1651.

Sihver, L., Mancusi, D., Niita, K., Sato, T., Townsend, L., Farmer, C., . . . Gomes, I. (2008). Benchmarking of calculated projectile fragmentation cross-sections using the 3-D, MC codes PHITS, FLUKA, HETC-HEDS, MCNPX_HI, and NUCFRG2. *Acta Astronautica, 63*(7–10), 865-877. doi:http://dx.doi.org/10.1016/j.actaastro.2008.02.012

Sihver, L., Sato, T., Puchalska, M., & Reitz, G. (2010). Simulations of the MATROSHKA experiment at the international space station using PHITS. *Radiation and Environmental Biophysics, 49*(3), 351-357. doi:10.1007/s00411-010-0288-y

Stewart, R. D., Yu, V. K., Georgakilas, A. G., Koumenis, C., Park, J. H., & Carlson, D. J. (2011). Effects of radiation quality and oxygen on clustered DNA lesions and cell death. *Radiat Res, 176*(5), 587-602. doi:10.1667/rr2663.1

Stucker, M., Struk, A., Altmeyer, P., Herde, M., Baumgartl, H., & Lubbers, D. W. (2001). The cutaneous uptake of atmospheric oxygen contributes significantly to the oxygen supply of human dermis and epidermis. *The Journal of Physiology, 538*(3), 985-994. doi:10.1113/jphysiol.2001.013067

Stuglik, Z. (1995). On the "Oxygen in Heavy-Ion Tracks" Hypothesis. *Radiation Research, 143*(3), 343. doi:10.2307/3579223

Talbot, A., Neuman, M., Saidel, G., & Jacobsen, E. (1996). Dynamic model of oxygen transport for transcutaneous PO2 analysis. *Annals of Biomedical Engineering, 24*(2), 294-304. doi:10.1007/BF02667356

Thomas, K. S. (2006). *U.S. Spacesuits* (H. J. McMann Ed.). UK: Praxis Publishing.

Tylka, A., & Dietrich, W. (2008). *Proton Spectra in Ground-Level Enhanced (GLE) Solar Particle Events*. Paper presented at the COSPAR Scientific Assembly, Montréal, Canada.

Valabrègue, R., Aubert, A., Burger, J., Bittoun, J., & Costalat, R. (2003). Relation between Cerebral Blood Flow and Metabolism Explained by a Model of Oxygen Exchange. *Journal of Cerebral Blood Flow & Metabolism, 23*(5), 536-545.

Van Beekvelt, M. C. P., Colier, W. N. J. M., Wevers, R. A., & Van Engelen, B. G. M. (2001). Performance of near-infrared spectroscopy in measuring local O2 consumption and blood flow in skeletal muscle. *Journal of Applied Physiology, 90*(2), 511-519.

van den Brenk, H. A. S., Kerr, R. C., Richter, W., & Papworth, M. P. (1965). Enhancement of Radiosensitivity of Skin of Patients by High Pressure Oxygen. *British Journal of Radiology, 38*(455), 857-864. doi:10.1259/0007-1285-38-455-857

Vasquez, T. E., Pretorius, H. T., & Rimkus, D. S. (1987). Space medicine--a review of current concepts. *West J Med, 147*(3), 292-295.

Wang, W., Winlove, C. P., & Michel, C. C. (2003). Oxygen partial pressure in outer layers of skin of human finger nail folds. *The Journal of Physiology, 549*(Pt 3), 855-863. doi:10.1113/jphysiol.2002.037994

Ward, J. F. (1994). The complexity of DNA damage: relevance to biological consequences. *Int J Radiat Biol, 66*(5), 427-432. doi:doi:10.1080/09553009414551401

Webber, W. R. (1963). *An Evaluation of the Radiation Hazard Due to Solar Particle Events*. Retrieved from

Whaley, J. T., Kirk, M., Cengel, K., McDonough, J., Bekelman, J., & Christodouleas, J. P. (2013). Protective effect of transparent film dressing on proton therapy induced skin reactions. *Radiation Oncology (London, England), 8*, 19-19. doi:10.1186/1748-717X-8-19

Wilson, J. M., Sanzari, J. K., Diffenderfer, E. S., Yee, S. S., Seykora, J. T., Maks, C., . . . Cengel, K. A. (2011). Acute Biological Effects of Simulating the Whole-Body Radiation Dose Distribution from a Solar Particle Event Using a Porcine Model. *Radiation Research, 176*(5), 649-659.

Wilson, J. W. (1976). *Preliminary analysis of the implications of natural radiations on geostationary operations*. Retrieved from

Wilson, J. W. (1978). *Environmental geophysics and SPS shielding*. Retrieved from

Wyatt, J. S., Cope, M., Delpy, D. T., Richardson, C. E., Edwards, A. D., Wray, S., & Reynolds, E. O. (1990). Quantitation of cerebral blood volume in human infants by near-infrared spectroscopy. *Journal of Applied Physiology, 68*(3), 1086-1091.

Xapsos, M. A., Barth, J. L., Stassinopoulos, E. G., Messenger, S. R., Walters, R. J., Summers, G. P., & Burke, E. A. (2000). Characterizing solar proton energy spectra for radiation effects applications. *IEEE Transactions on Nuclear Science, 47*(6), 2218-2223. doi:10.1109/23.903756

Zeitlin, C., Guetersloh, S., Heilbronn, L., & Miller, J. (2005). Shielding and fragmentation studies. *Radiat Prot Dosimetry, 116*(1-4 Pt 2), 123-124.

Zeitlin, C., Heilbronn, L., Miller, J., & Shavers, M. (2001). Radiation tests of the EMU spacesuit for the International Space Station using energetic protons.

Zhou, Y., Ni, H., Balint, K., Sanzari, J. K., Dentchev, T., Diffenderfer, E. S., . . . Weissman, D. (2014). Ionizing Radiation Selectively Reduces Skin Regulatory T Cells and Alters Immune Function. *PLoS ONE, 9*(6), e100800. doi:10.1371/journal.pone.0100800

APPENDIX A. SOLAR PARTICLE EVENT SPECTRA

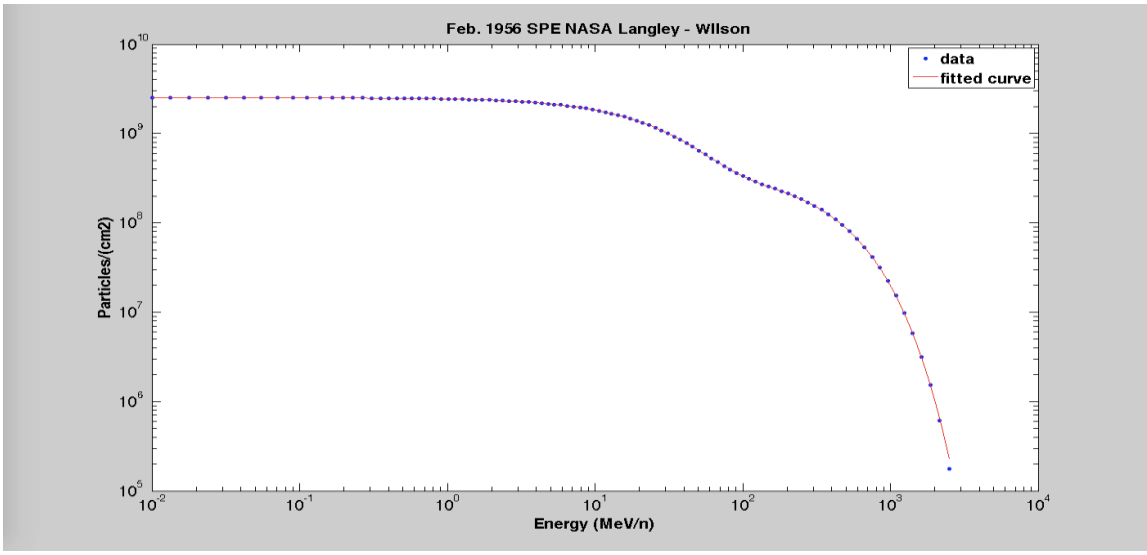

February 1956 SPE Integral Flux. Data obtained from (J. W. Wilson, 1976)

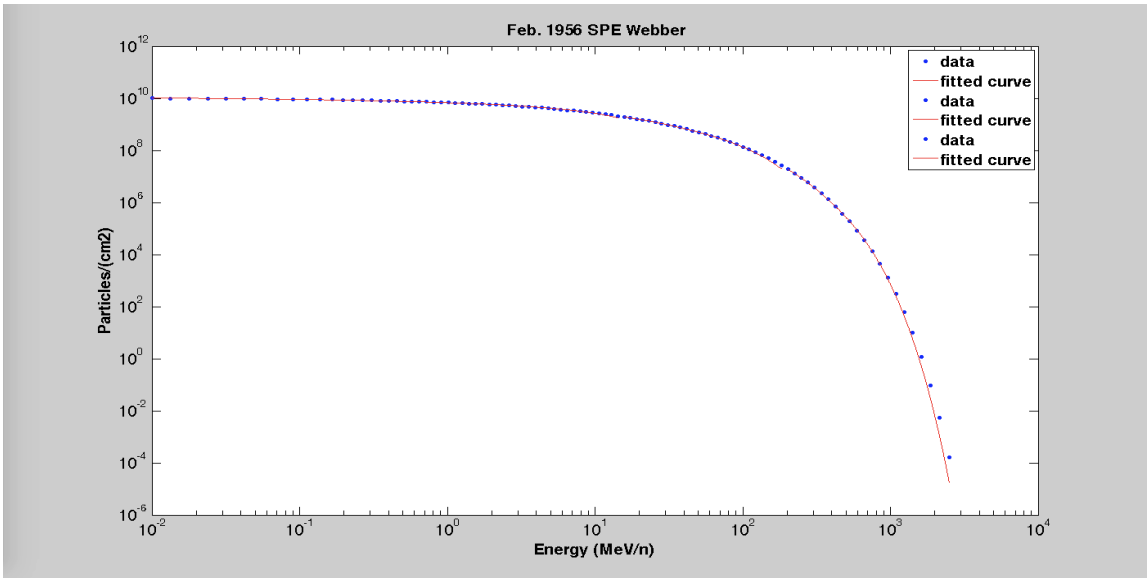

February 1956 SPE Integral Flux. Data obtained from (Webber, 1963)

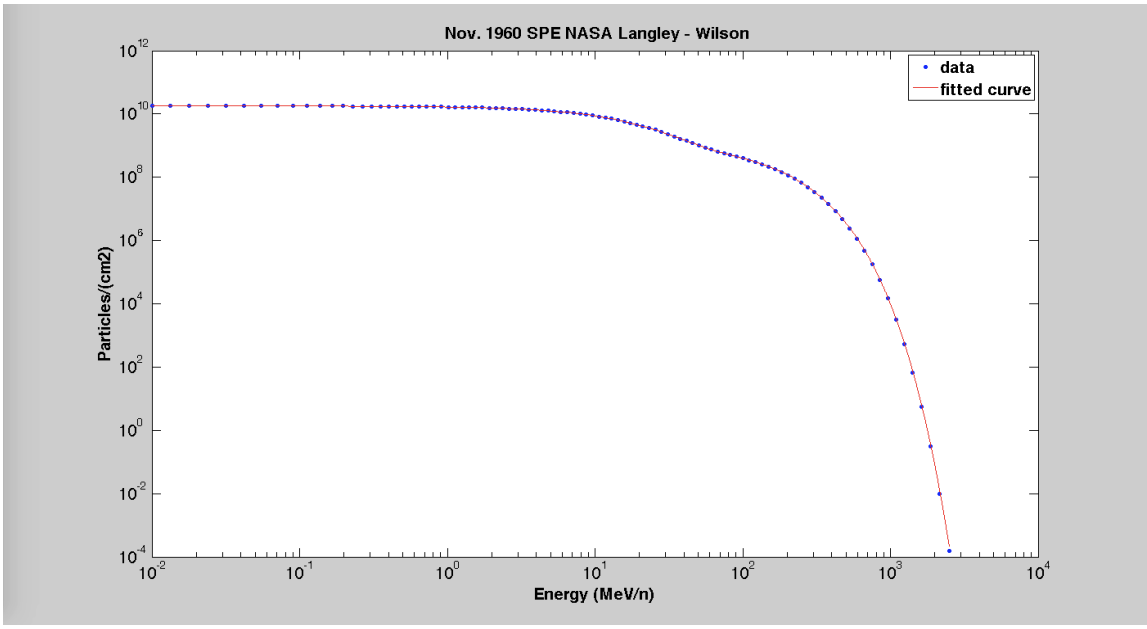

November 1960 SPE Integral Flux. Data obtained from (J. W. Wilson, 1976)

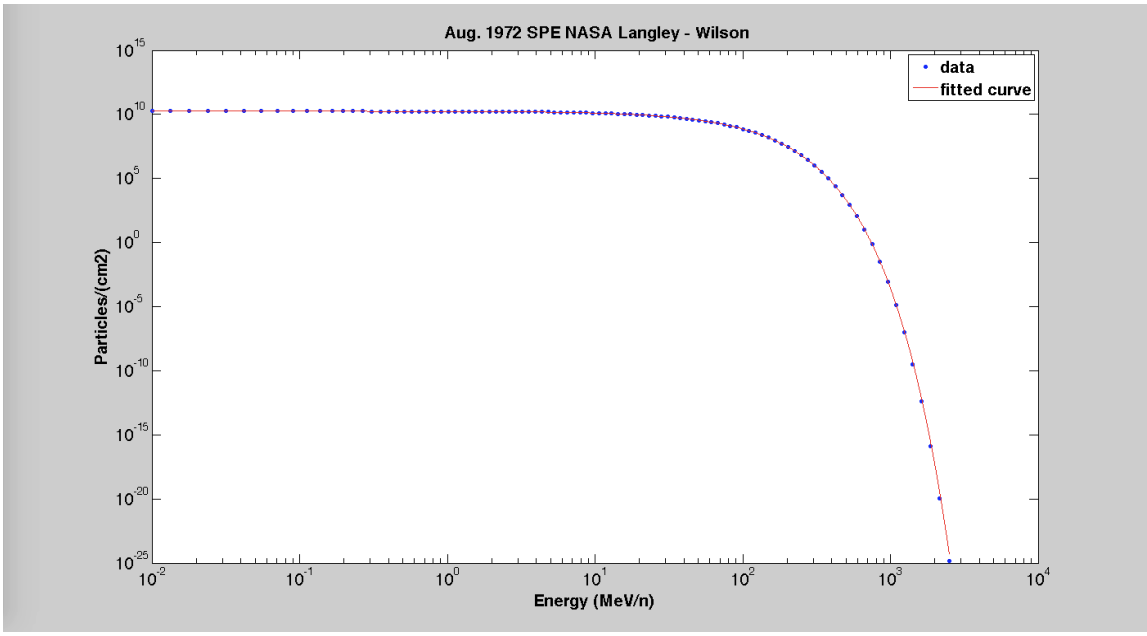

August 1972 SPE Integral Flux. Data obtained from (J. W. Wilson, 1976)

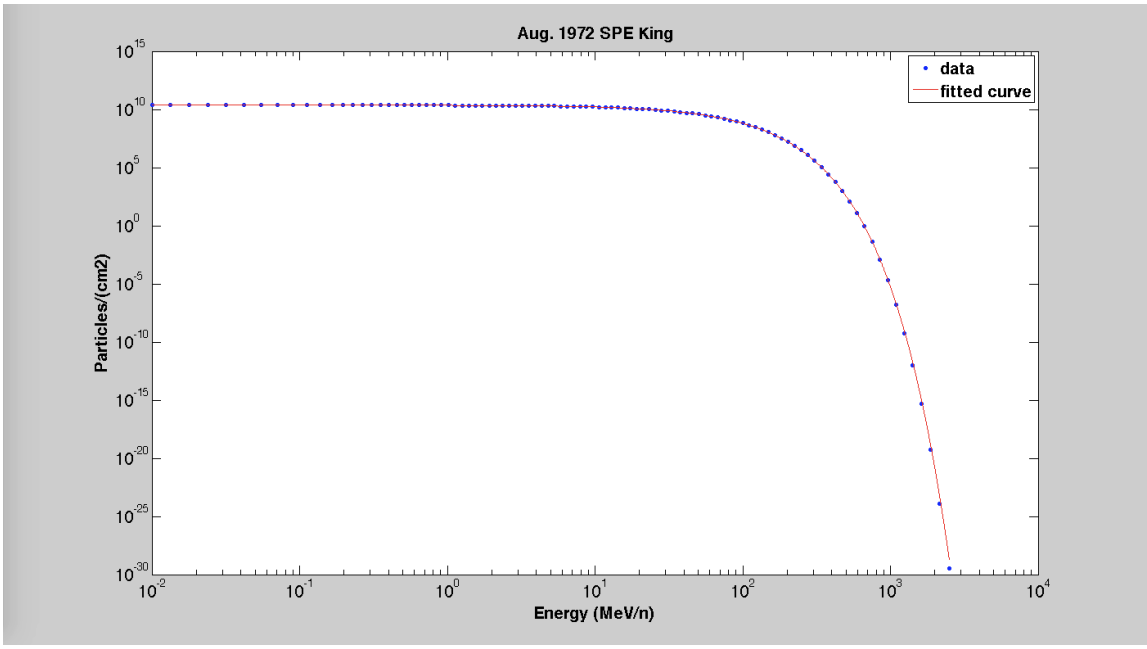

Figure X. August 1972 SPE Integral Flux. Data obtained from (King, 1974)

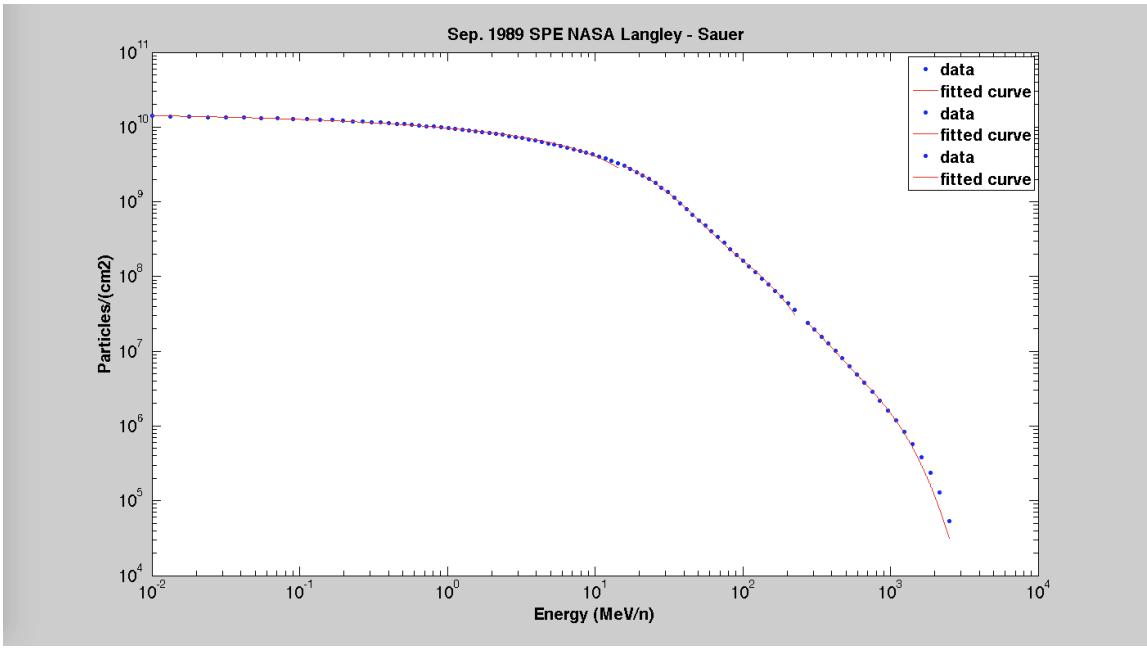

September 1989 SPE Integral Flux. Data obtained from (Sauer, 1990)

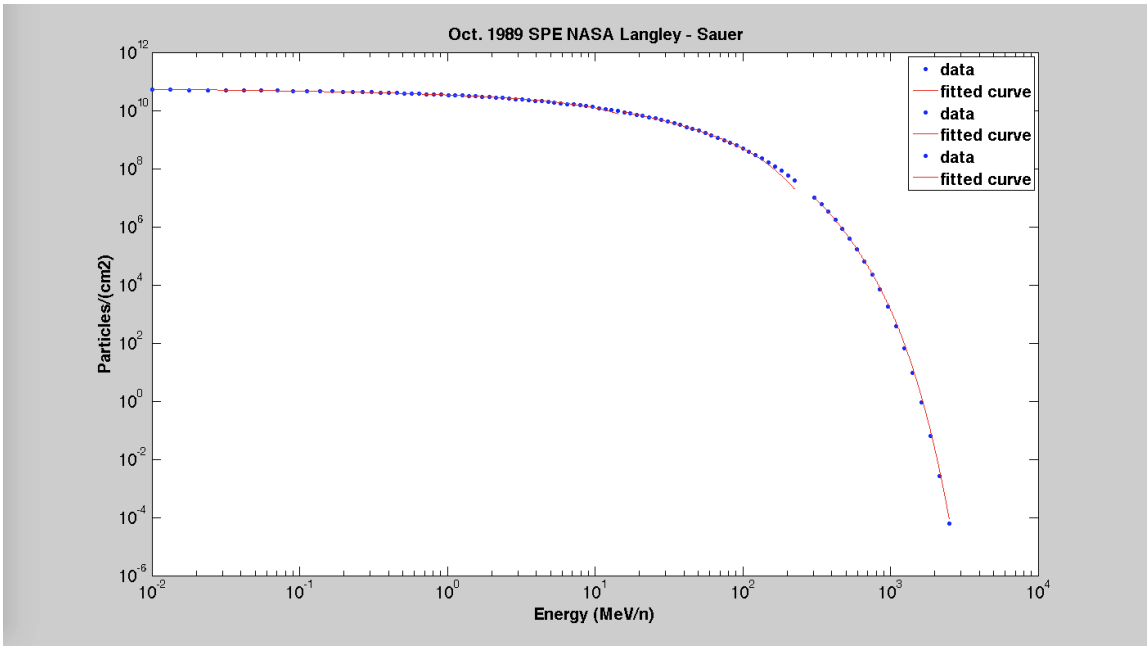

October 1989 SPE Integral Flux. Data obtained from (Sauer, 1990)

APPENDIX B. UTILIZED CODES AND SCRIPTS

B.1 MATLAB Total Flux Scaling Code

```
function fluxsource = sourceselecter(midmid, midmidmid)

fluxsource=0; %% particles/cm2

if strcmp(midmidmid,'1956')
    if strcmp(midmid,'Wilson')
        fluxsource= 2.52E+09   ;
    elseif strcmp(midmid,'Webber')
        fluxsource= 1.01E+10;
    else
        msgbox('error2')
    end
elseif strcmp(midmidmid,'1960')
    if strcmp(midmid,'Wilson')
        fluxsource= 1.79E+10;
    else
        msgbox('error3')
    end
elseif strcmp(midmidmid,'1972')
    if strcmp(midmid,'Wilson')
        fluxsource=  1.76E+10;
    elseif strcmp(midmid,'King')
        fluxsource= 2.33E+10;
    else
        msgbox('error4')
    end
elseif strcmp(midmidmid,'1989')
    if strcmp(midmid,'Sep')
        fluxsource= 1.41E+10;
    elseif strcmp(midmid,'Oct')
        fluxsource= 5.21E+10;
    else
        msgbox('error5')
    end
else
    msgbox('error1')
end
end
```

B.2 MATLAB Script for Import of PHITS Output

```
list = which('dose.out','-all');
```

```
for i=1:size(list,1)

    [pathstr,name,ext] = fileparts(list{i}
q)

    cd(pathstr)

    doseimport('dose.out')

end


list = which('flux.out','-all');
for i=4:size(list,1)

    [pathstr,name,ext] = fileparts(list{i}) ;

    cd(pathstr);

    [earray,bin,headers]=importfluxes('flux.out');
    save flux earray bin headers
    clear earray bin headers
end


function doseimport(fileToReadX)

DELIMITER = ' ';
HEADERLINES = 842;

% Import the file
datastruct = importdata(fileToReadX, DELIMITER, HEADERLINES);

dosearray=datastruct.data;

save dose.mat dosearray

clear datastruct HEADERLINES dosearray

end


function [earray,bin,headers]=importfluxes(fileToRead1)
%IMPORTFILE(FILETOREAD1)
%  Imports data from the specified file
%  FILETOREAD1:  file to read
DELIMITER = ' ';
HEADERLINES = 825;
```

```
% Import the file
datastruct = importdata(fileToRead1, DELIMITER, HEADERLINES);

k=1;
    for i=1:size(datastruct.data,1)

        for j=1:size(datastruct.data,2)


            if  ~isnan(datastruct.data(i,j))

                earray(k)=datastruct.data(i,j);
                k=k+1;
            end
        end
    end
clear datastruct HEADERLINES i j k



%%%%%%%%%
bin={};

for i=1:100
    j=(i-1)*4026+867; %%headerlines
    k=1+i;  %%dataset

    DELIMITER = ' ';
    HEADERLINES = j;

    filenamo=horzcat('newData',num2str(k));
    datanamo=horzcat('data',num2str(k));

    str1=horzcat(filenamo,'=','importdata(fileToRead1, DELIMITER,
HEADERLINES);');

% Import the file
eval(str1);

% Create new variables in the base workspace from those fields.
str2=horzcat('bin{i}=',filenamo,'.data;');
eval(str2);


end


headers.BinIndex1='z-lower';
headers.BinIndex2='z-upper';
headers.BinIndex3='Protons';
```

```
headers.BinIndex4='Protons-Error';
headers.BinIndex5='Alphas';
headers.BinIndex6='Alpha-Error';
headers.BinIndex7='Electrons';
headers.BinIndex8='Electrons-Error';
headers.BinIndex9='O16';
headers.BinIndex10='O16-Error';
headers.BinIndex11='C12';
headers.BinIndex12='C12-Error';
headers.BinIndex13='Fe56';
headers.BinIndex14='Fe56-Error';

end
```

B.3 Mathematica Script for Oxygen Concentration Gradient

```
params = {d0 -> 1*10^-6, d1 -> 1.5*10^-5, V1 -> .059, K1 -> .075,    u0 -> 0, j0 ->
0.18995, j1 -> 10.13} tFinal = 720; lFinal = .15; lstratc = .0015;

pde = D[c[x, t], t] ==    Piecewise[{{d0*D[c[x, t], x, x],       x <= lstratc}, {d1*
D[c[x, t], x, x] - ((V1*c[x, t])/(K1 + c[x, t])), x > lstratc}}]

ic = {c[x, 0] == Piecewise[{{j0, x == 0}, {j1, x == lFinal}}, 0]}

bc1 = c[0, t] == j0 bc2 = c[lFinal, t] == j1 soln = NDSolve[Flatten@{pde, ic, bc1, bc2}
/. params,    c, {t, 0, tFinal}, {x, 0, lFinal /. params},    Method -> {"MethodOfLines",
"SpatialDiscretization" -> {"TensorProductGrid",       "MinPoints" -> 1000}}]
```

```
Plot3D[c[x, t] /. soln, {x, 0, lFinal}, {t, 0, tFinal}, ColorFunction -> Function[{x, y, z},
RGBColor[.5, .8, z]], BoxRatios -> 1, AxesLabel -> {"Depth (cm)", "Time (s)",
"Concentration mM"}, BaseStyle -> {FontWeight -> "Bold", FontSize -> 20}]

Plot3D[c[x, t] /. soln, {x, 0, lFinal/5}, {t, 0, tFinal/2}, ColorFunction -> Function[{x, y,
z}, RGBColor[.5, .8, z]], BoxRatios -> 1, AxesLabel -> {"Depth (cm)", "Time (s)",
"Concentration mM"}, BaseStyle -> {FontWeight -> "Bold", FontSize -> 20}]
ThickSkin = c[x, tFinal] /. soln thick = Plot[ThickSkin, {x, 0.00, lFinal}, AxesLabel ->
{"Depth (cm)", "Concentration mM"}, PlotStyle -> {Blue, Thick}, PlotLegends ->
LineLegend[{Blue}, {"Thick Skin"}]]
```

B.4 Sample PHITS Input Code

```
[ T i t l e ]
proton spectra 1972 KING SPE 1cm thick shield

[ Parameters]
icntl   =          0     # (D=0) 3:ECH 5:NOR 6:SRC 7,8:GSH 11:DSH 12:DUMP
!! 0: normal, 7: 2D-geometry plot, 11: 3D-geometry plot.
!!
!! It requires [t-gshow] section for icntl=7, and
!! [t-3dshow] section for icntl=11
!!
 maxcas   =       1000000 # (D=10) number of particles per one batch
 maxbch   =            10     # (D=10) number of batches
 emin(1) =          1.e-3   # Energy cutoff for proton (MeV) (D=1.0)
 emin(2)  =        1.0E-6  # (D=1.0) cut-off energy of neutron (MeV)
 dmax(2)  =        20.00    # (D=emin(2)) data max. energy of neutron (MeV)
 emin(12) =        1.00E-01 # (D=1.d9) cut-off energy of electron (MeV)
 emin(13) =        1.00E-01 # (D=1.d9) cut-off energy of positron (MeV)
 emin(14) =       1.000E-01 # (D=1.d9) cut-off energy of photon (MeV)
 dmax(12) =  1000.00000     # (D=emin(12)) data max. energy of electron (MeV)
 dmax(13) =  1000.00000     # (D=emin(13)) data max. energy of positron (MeV)
 dmax(14) =  1000.00000     # (D=emin(14)) data max. energy of photon (MeV)
 nlost    =  1000
 igamma   =           1     # (D=0) photon emission from residual nuclei
 e-mode   =           1     # (D=0) 0: Normal, 1: Event generator mode
 nedisp   =           1     # (D=0) 0: no, 1: with e straggling, 10: ATIMA
 nspred   =           1     # (D=0) 0:no, 1:orig. 2:first Moliere, 10: ATIMA
 file(6)  = phits.out       # (D=phits.out) general output file name
 file(7)  = /Applications/phits/data/xsdir.jnd # (D=xdirs) nuclear data input file name
 file(14) = /Applications/phits/data/trxcrd.dat # (D=trxcrd.dat) photon data input file
name

[ S o u r c e ]
s-type = 4          # Cylinder With Energy Distribution
proj = proton
r0 =   0.0000       # radius [cm]
x0 =   0.0000       # (D=0.0) center position of x-axis [cm]
y0 =   0.0000       # (D=0.0) center position of y-axis [cm]
z0 =  -5.000        # minimum position of z-axis [cm]
z1 =  -5.000        # maximum position of z-axis [cm]
dir =   1.0000      # z-direction of beam [cosine]
```

e-type = 21 # energy bins e(i) and probabilities of the particle generation dN/dE(i)
by hand
ne=-100 # (e(i),dN/dE(i),i=1,ne), e(ne+1).
0.001 924070000
0.01 923960000
0.01338088 923800000
0.01790479 923590000
0.02390681 923310000
0.03183221 9.23E+08
4.21E-02 9.23E+08
5.51E-02 9.22E+08
7.11E-02 9.21E+08
9.03E-02 9.21E+08
1.12E-01 9.20E+08
1.38E-01 9.19E+08
1.66E-01 9.18E+08
1.97E-01 9.16E+08
2.30E-01 9.15E+08
2.68E-01 9.14E+08
3.08E-01 9.12E+08
3.53E-01 9.11E+08
4.01E-01 9.09E+08
4.54E-01 9.07E+08
5.13E-01 9.05E+08
5.77E-01 9.02E+08
6.48E-01 8.99E+08
7.26E-01 8.96E+08
8.13E-01 8.93E+08
9.09E-01 889720000
1.014071 885840000
1.129672 881550000
1.258328 876870000
1.399567 871700000
1.556046 866040000
1.728746 859840000
1.919146 853060000
2.129073 845620000
2.36107 8.37E+08
2.62E+00 8.29E+08
2.90E+00 8.19E+08
3.21E+00 8.08E+08
3.55E+00 7.97E+08
3.93E+00 7.84E+08
4.35E+00 7.71E+08

4.81E+00	7.56E+08
5.32E+00	7.41E+08
5.88E+00	7.24E+08
6.49E+00	7.05E+08
7.17E+00	6.86E+08
7.91E+00	6.65E+08
8.74E+00	6.42E+08
9.64E+00	6.19E+08
1.06E+01	5.94E+08
1.17E+01	5.67E+08
1.29E+01	5.39E+08
1.43E+01	5.10E+08
1.57E+01	4.80E+08
1.74E+01	4.49E+08
1.91E+01	4.17E+08
2.11E+01	3.85E+08
2.32E+01	3.52E+08
2.56E+01	3.19E+08
2.82E+01	2.86E+08
3.11E+01	2.54E+08
3.43E+01	2.22E+08
3.78E+01	1.92E+08
4.16E+01	1.64E+08
4.58E+01	1.37E+08
5.05E+01	1.13E+08
5.57E+01	9.12E+07
6.14E+01	7.20E+07
6.77E+01	5.54E+07
7.46E+01	4.15E+07
8.23E+01	3.01E+07
9.07E+01	2.11E+07
1.00E+02	1.43E+07
1.11E+02	9.25E+06
1.22E+02	5.71E+06
1.35E+02	3.35E+06
1.49E+02	1.84E+06
1.65E+02	9.49E+05
1.82E+02	4.55E+05
2.02E+02	1.98E+05
2.24E+02	7.84E+04
2.48E+02	2.81E+04
2.76E+02	8.93E+03
3.06E+02	2.41E+03
3.41E+02	5.60E+02

```
3.79E+02  1.07E+02
4.23E+02  1.65E+01
4.73E+02  1.97E+00
5.29E+02  1.77E-01
5.93E+02  1.10E-02
6.66E+02  4.64E-04
7.51E+02  1.21E-05
8.47E+02  1.79E-07
9.59E+02  1.23E-09
1.09E+03  3.84E-12
1.24E+03  5.37E-15
1.42E+03  2.18E-18
1.62E+03  2.15E-22
1.87E+03  3.97E-27
2.16E+03  9.88E-33
2.50E+03


[ M a t e r i a l ]
MAT[ 1 ]  # ICRU soft tissue
        1H        6.0820000E-02
       12C        5.5700000E-03
       14N        1.1180000E-03
       16O        2.8680000E-02
MAT[ 2 ]
       27Al      1.000

[ C e l l ]
 1        2 -2.7   1 -2 -11  $ Al
 2        1 -1     2 -4 -11  $ tissue
98        0       #1 #2 -999    $ Void
99       -1          999    $ Outer region

[ S u r f a c e ]
 1          pz   0.0
 2          pz   1.0
 4          pz   40.0
 11         cz   100.0
999         so   300.0


[ T -track ]
title = flux distribution
part = proton alpha electron O16 C12 Fe56
```

```
mesh =  r-z          # mesh type is r-z scoring mesh
x0 =   0.000000      # center x-position of r-z mesh
y0 =   0.000000      # center y-position of r-z mesh
r-type =    2        # r-mesh is linear given by rmin, rmax and nr
rmin =   0.000000     # minimum value of r-mesh points
rmax =   25.000000     # maximum value of r-mesh points
nr =    1          # number of r-mesh points
z-type =    2         # z-mesh is linear given by zmin, zmax and nz
zmin =   0.000000     # minimum value of z-mesh points
zmax =   20.00000     # maximum value of z-mesh points
nz =  4000          # number of z-mesh points
e-type = 3          $Energy Mesh - min and max log scale
ne = 100       $ Number of Mesh points
emin = 1.e-2     $ min of Mesh
emax = 5.e3     $ max of mesh
unit =    1          # unit is [1/cm2/source]
axis =     z         # axis of
file = flux.out       # file name of output for the above axis
epsout =    1



[ T - Deposit ]
title = depth-dose distribution
mesh =  r-z          # mesh type is r-z scoring mesh
x0 =   0.000000      # center x-position of r-z mesh
y0 =   0.000000      # center y-position of r-z mesh
r-type =    2        # r-mesh is linear given by rmin, rmax and nr
rmin =   0.000000     # minimum value of r-mesh points
rmax =   25.000000     # maximum value of r-mesh points
nr =    1          # number of r-mesh points
z-type =    2         # z-mesh is linear given by zmin, zmax and nz
zmin =   0.000000     # minimum value of z-mesh points
zmax =   20.00000     # maximum value of z-mesh points
nz =   4000          # number of z-mesh points
unit =    2          # unit is [MeV/source)]
letmat =    0         # (D=0) material id for LET, 0: real material
dedxfnc =    0          # (D=0) user defined multiplier, 0(no), 1, 2
material =  all          # (D=all) number of specific material
output =  dose          # total deposit energy
axis =     z         # axis of output
file = dose.out       # file name of output for the above axis
part =  all
epsout =    1
```

```
[ T -cross]
part = proton alpha neutron electron O16 C12
mesh = reg      $Cell Interface
reg = 1       $Crossing Surfaces
r-in r-out area $Crossing Cells
1 2 .01
e-type = 3      $Energy Mesh - min and max log scale
ne = 100        $ Number of Mesh points
emin = 1.e0     $ min of Mesh
emax = 5.e3     $ max of mesh
unit = 1        $ 1/cm2/source
axis = eng      $ x axis value of output data
file = cross_particle.out
output = flux   $ flux by surface crossing
x-txt = {\it En} (MeV)
y-txt = {\it Flux} (1/cm^2)
epsout = 1  $output written to eps file (plot)


[ delta ray ]
reg del
2 0.1
```

B.5 Sample PHITS Output (Incident Skin Spectra)

```
Filename = cross_particle.out
[ T - C r o s s ]
   title = [t-cross] in region mesh
    mesh =  reg           # mesh type is region-wise
     reg =    1           # number of crossing regions
     non     r-in  r-out    area
       1     1     2     1.0000000E-02
  e-type =    3           # e-mesh is log given by emin, emax and ne
    emin =   1.000000      # minimum value of e-mesh points
    emax =   5000.000      # maximum value of e-mesh points
#    edel =  8.5171932E-02  # mesh width of e-mesh points
      ne =  100           # number of e-mesh points
#    data = ( e(i), i = 1, ne + 1 )
#          1.00000E+00  1.08890E+00  1.18571E+00  1.29113E+00  1.40591E+00
#          1.53091E+00  1.66701E+00  1.81521E+00  1.97659E+00  2.15232E+00
```

```
#          2.34367E+00  2.55204E+00  2.77892E+00  3.02598E+00  3.29500E+00
#          3.58794E+00  3.90693E+00  4.25427E+00  4.63249E+00  5.04434E+00
#          5.49280E+00  5.98114E+00  6.51288E+00  7.09191E+00  7.72241E+00
#          8.40896E+00  9.15656E+00  9.97061E+00  1.08570E+01  1.18223E+01
#          1.28733E+01  1.40178E+01  1.52641E+01  1.66211E+01  1.80988E+01
#          1.97079E+01  2.14600E+01  2.33679E+01  2.54454E+01  2.77076E+01
#          3.01709E+01  3.28532E+01  3.57740E+01  3.89545E+01  4.24177E+01
#          4.61888E+01  5.02952E+01  5.47666E+01  5.96356E+01  6.49375E+01
#          7.07107E+01  7.69972E+01  8.38425E+01  9.12965E+01  9.94131E+01
#          1.08251E+02  1.17875E+02  1.28355E+02  1.39766E+02  1.52192E+02
#          1.65723E+02  1.80456E+02  1.96499E+02  2.13969E+02  2.32992E+02
#          2.53706E+02  2.76261E+02  3.00822E+02  3.27567E+02  3.56689E+02
#          3.88400E+02  4.22930E+02  4.60531E+02  5.01474E+02  5.46057E+02
#          5.94604E+02  6.47466E+02  7.05029E+02  7.67709E+02  8.35962E+02
#          9.10282E+02  9.91210E+02  1.07933E+03  1.17529E+03  1.27978E+03
#          1.39356E+03  1.51745E+03  1.65236E+03  1.79926E+03  1.95922E+03
#          2.13340E+03  2.32307E+03  2.52960E+03  2.75450E+03  2.99938E+03
#          3.26604E+03  3.55640E+03  3.87258E+03  4.21687E+03  4.59177E+03
#          5.00000E+03
    unit =    1          # unit is [1/cm^2/source]
    axis =  eng          # axis of output
    file = cross_particle.out  # file name of output for the above axis
  output = flux          # surface crossing flux
    part =  proton    alpha     neutron   electron   16O       12C
# kf/name :  2212      2000004   2112      11         8000016   6000012
   x-txt = {\it En} (MeV)
   y-txt = {\it Flux} (1/cm^2)
  epsout =    1          # (D=0) generate eps file by ANGEL
#    used :       main (  %)       temp (  %)      total (  %)
#  memory :        114 (  0)          0 (  0)        114 (  0)

#-------------------------------------------------------------------------------
#newpage:
#   no. =    1   reg = 1 - 2

x: {\it En} (MeV)
y: {\it Flux} (1/cm^2)
p: xlog ylog afac(0.8) form(0.9)
h: n          x          y(proton  ),hh01 n  y(alpha   ),hh0dr n  y(neutron ),hh0mb n
y(electron),hh0ug n  y(16O     ),hh0pc n  y(12C     ),hh0q  n
# e-lower    e-upper       flux    r.err      flux    r.err      flux    r.err      flux    r.err
flux    r.err      flux    r.err
  1.0000E+00   1.0889E+00   3.0480E-03  0.0597   0.0000E+00  0.0000   1.2016E-02
0.0478   1.3513E-03  0.2293   0.0000E+00  0.0000   0.0000E+00  0.0000
```

1.0889E+00 1.1857E+00 3.7138E-03 0.0604 0.0000E+00 0.0000 1.2516E-02
0.1045 1.2251E-03 0.1373 0.0000E+00 0.0000 0.0000E+00 0.0000
1.1857E+00 1.2911E+00 3.9047E-03 0.0553 0.0000E+00 0.0000 1.2876E-02
0.0709 1.5241E-03 0.1241 0.0000E+00 0.0000 0.0000E+00 0.0000
1.2911E+00 1.4059E+00 4.9058E-03 0.0419 0.0000E+00 0.0000 1.5707E-02
0.0590 2.0408E-03 0.3049 0.0000E+00 0.0000 0.0000E+00 0.0000
1.4059E+00 1.5309E+00 5.1376E-03 0.0342 0.0000E+00 0.0000 1.4907E-02
0.0817 1.3829E-03 0.1407 0.0000E+00 0.0000 0.0000E+00 0.0000
1.5309E+00 1.6670E+00 5.3888E-03 0.0438 0.0000E+00 0.0000 1.3919E-02
0.0645 1.2993E-03 0.0856 0.0000E+00 0.0000 0.0000E+00 0.0000
1.6670E+00 1.8152E+00 7.0587E-03 0.0332 0.0000E+00 0.0000 1.9108E-02
0.1004 1.5956E-03 0.1680 0.0000E+00 0.0000 0.0000E+00 0.0000
1.8152E+00 1.9766E+00 8.0747E-03 0.0218 0.0000E+00 0.0000 1.9933E-02
0.0433 2.1966E-03 0.2938 0.0000E+00 0.0000 0.0000E+00 0.0000
1.9766E+00 2.1523E+00 9.6994E-03 0.0343 0.0000E+00 0.0000 2.0204E-02
0.0913 1.7952E-03 0.2597 0.0000E+00 0.0000 0.0000E+00 0.0000
2.1523E+00 2.3437E+00 1.0748E-02 0.0349 0.0000E+00 0.0000 1.8968E-02
0.0526 2.5444E-03 0.2918 0.0000E+00 0.0000 0.0000E+00 0.0000
2.3437E+00 2.5520E+00 1.3068E-02 0.0307 0.0000E+00 0.0000 2.1169E-02
0.0546 2.1305E-03 0.3023 0.0000E+00 0.0000 0.0000E+00 0.0000
2.5520E+00 2.7789E+00 1.3635E-02 0.0320 0.0000E+00 0.0000 1.9746E-02
0.0397 2.4817E-03 0.2890 0.0000E+00 0.0000 0.0000E+00 0.0000
2.7789E+00 3.0260E+00 1.5871E-02 0.0321 0.0000E+00 0.0000 2.3111E-02
0.0825 1.7154E-03 0.3315 0.0000E+00 0.0000 0.0000E+00 0.0000
3.0260E+00 3.2950E+00 1.9720E-02 0.0223 0.0000E+00 0.0000 2.2306E-02
0.0523 1.2631E-03 0.1612 0.0000E+00 0.0000 0.0000E+00 0.0000
3.2950E+00 3.5879E+00 2.1977E-02 0.0164 0.0000E+00 0.0000 2.0973E-02
0.0452 1.5193E-03 0.1814 0.0000E+00 0.0000 0.0000E+00 0.0000
3.5879E+00 3.9069E+00 2.4936E-02 0.0189 0.0000E+00 0.0000 2.2378E-02
0.0750 1.4673E-03 0.1109 0.0000E+00 0.0000 0.0000E+00 0.0000
3.9069E+00 4.2543E+00 2.9447E-02 0.0182 0.0000E+00 0.0000 2.3370E-02
0.0546 1.1111E-03 0.2027 0.0000E+00 0.0000 0.0000E+00 0.0000
4.2543E+00 4.6325E+00 3.4586E-02 0.0114 2.5633E-05 1.0000 2.5070E-02
0.0590 1.2807E-03 0.2153 0.0000E+00 0.0000 0.0000E+00 0.0000
4.6325E+00 5.0443E+00 3.9589E-02 0.0148 1.2550E-05 1.0000 2.6226E-02
0.0458 1.2451E-03 0.1531 0.0000E+00 0.0000 0.0000E+00 0.0000
5.0443E+00 5.4928E+00 4.5661E-02 0.0183 2.1414E-05 0.6668 2.2392E-02
0.0459 7.7808E-04 0.2353 0.0000E+00 0.0000 0.0000E+00 0.0000
5.4928E+00 5.9811E+00 5.3350E-02 0.0151 1.2089E-05 1.0000 2.0653E-02
0.0491 1.0682E-03 0.2318 0.0000E+00 0.0000 0.0000E+00 0.0000
5.9811E+00 6.5129E+00 6.1293E-02 0.0139 2.2771E-05 1.0000 1.9696E-02
0.0785 5.8419E-04 0.1197 0.0000E+00 0.0000 0.0000E+00 0.0000
6.5129E+00 7.0919E+00 7.1451E-02 0.0145 2.7051E-05 0.6667 2.0149E-02
0.0531 3.9798E-04 0.1906 0.0000E+00 0.0000 0.0000E+00 0.0000

7.0919E+00 7.7224E+00 8.2501E-02 0.0133 1.3276E-04 1.0000 2.1476E-02
0.0845 4.8237E-04 0.2394 0.0000E+00 0.0000 0.0000E+00 0.0000
7.7224E+00 8.4090E+00 9.4910E-02 0.0118 2.8711E-05 1.0000 1.7819E-02
0.0388 4.6423E-04 0.4994 0.0000E+00 0.0000 0.0000E+00 0.0000
8.4090E+00 9.1566E+00 1.0906E-01 0.0057 3.7653E-05 0.7040 1.7956E-02
0.0451 0.0000E+00 0.0000 0.0000E+00 0.0000 0.0000E+00 0.0000
9.1566E+00 9.9706E+00 1.2596E-01 0.0063 0.0000E+00 0.0000 1.7777E-02
0.0354 4.3955E-05 0.6943 0.0000E+00 0.0000 0.0000E+00 0.0000
9.9706E+00 1.0857E+01 1.4598E-01 0.0103 0.0000E+00 0.0000 1.9476E-02
0.0748 1.3870E-05 1.0000 0.0000E+00 0.0000 0.0000E+00 0.0000
1.0857E+01 1.1822E+01 1.6863E-01 0.0094 0.0000E+00 0.0000 1.6580E-02
0.0844 5.1534E-05 0.7354 0.0000E+00 0.0000 0.0000E+00 0.0000
1.1822E+01 1.2873E+01 1.8756E-01 0.0050 0.0000E+00 0.0000 1.6633E-02
0.0244 0.0000E+00 0.0000 0.0000E+00 0.0000 0.0000E+00 0.0000
1.2873E+01 1.4018E+01 2.0589E-01 0.0095 0.0000E+00 0.0000 1.6684E-02
0.0676 0.0000E+00 0.0000 0.0000E+00 0.0000 0.0000E+00 0.0000
1.4018E+01 1.5264E+01 2.2905E-01 0.0062 0.0000E+00 0.0000 1.5295E-02
0.0504 0.0000E+00 0.0000 0.0000E+00 0.0000 0.0000E+00 0.0000
1.5264E+01 1.6621E+01 2.6127E-01 0.0048 1.0194E-05 1.0000 1.4822E-02
0.0490 0.0000E+00 0.0000 0.0000E+00 0.0000 0.0000E+00 0.0000
1.6621E+01 1.8099E+01 2.9840E-01 0.0047 0.0000E+00 0.0000 1.6364E-02
0.0516 0.0000E+00 0.0000 0.0000E+00 0.0000 0.0000E+00 0.0000
1.8099E+01 1.9708E+01 3.4112E-01 0.0059 1.4365E-05 1.0000 1.3258E-02
0.0619 0.0000E+00 0.0000 0.0000E+00 0.0000 0.0000E+00 0.0000
1.9708E+01 2.1460E+01 3.8507E-01 0.0060 3.2326E-05 0.5098 1.5325E-02
0.0599 0.0000E+00 0.0000 0.0000E+00 0.0000 0.0000E+00 0.0000
2.1460E+01 2.3368E+01 4.3458E-01 0.0043 1.0324E-05 1.0000 1.3635E-02
0.0568 0.0000E+00 0.0000 0.0000E+00 0.0000 0.0000E+00 0.0000
2.3368E+01 2.5445E+01 4.7297E-01 0.0041 0.0000E+00 0.0000 1.4479E-02
0.0774 0.0000E+00 0.0000 0.0000E+00 0.0000 0.0000E+00 0.0000
2.5445E+01 2.7708E+01 4.9455E-01 0.0043 0.0000E+00 0.0000 1.2458E-02
0.0500 0.0000E+00 0.0000 0.0000E+00 0.0000 0.0000E+00 0.0000
2.7708E+01 3.0171E+01 5.5100E-01 0.0046 0.0000E+00 0.0000 1.0902E-02
0.0694 0.0000E+00 0.0000 0.0000E+00 0.0000 0.0000E+00 0.0000
3.0171E+01 3.2853E+01 6.0808E-01 0.0036 0.0000E+00 0.0000 1.0541E-02
0.0567 0.0000E+00 0.0000 0.0000E+00 0.0000 0.0000E+00 0.0000
3.2853E+01 3.5774E+01 6.3245E-01 0.0044 0.0000E+00 0.0000 9.0021E-03
0.0297 0.0000E+00 0.0000 0.0000E+00 0.0000 0.0000E+00 0.0000
3.5774E+01 3.8954E+01 6.4426E-01 0.0040 1.0268E-05 1.0000 8.0306E-03
0.0846 0.0000E+00 0.0000 0.0000E+00 0.0000 0.0000E+00 0.0000
3.8954E+01 4.2418E+01 7.0932E-01 0.0037 0.0000E+00 0.0000 7.6089E-03
0.0634 0.0000E+00 0.0000 0.0000E+00 0.0000 0.0000E+00 0.0000
4.2418E+01 4.6189E+01 6.9267E-01 0.0036 0.0000E+00 0.0000 6.6145E-03
0.1055 0.0000E+00 0.0000 0.0000E+00 0.0000 0.0000E+00 0.0000

4.6189E+01 5.0295E+01 7.0746E-01 0.0037 0.0000E+00 0.0000 5.7536E-03
0.0938 0.0000E+00 0.0000 0.0000E+00 0.0000 0.0000E+00 0.0000
5.0295E+01 5.4767E+01 7.0367E-01 0.0044 0.0000E+00 0.0000 3.9431E-03
0.0528 0.0000E+00 0.0000 0.0000E+00 0.0000 0.0000E+00 0.0000
5.4767E+01 5.9636E+01 6.7305E-01 0.0036 0.0000E+00 0.0000 4.3752E-03
0.1371 0.0000E+00 0.0000 0.0000E+00 0.0000 0.0000E+00 0.0000
5.9636E+01 6.4937E+01 6.5508E-01 0.0039 1.4212E-05 1.0000 3.1221E-03
0.0827 0.0000E+00 0.0000 0.0000E+00 0.0000 0.0000E+00 0.0000
6.4937E+01 7.0711E+01 6.0428E-01 0.0034 0.0000E+00 0.0000 2.4408E-03
0.0748 0.0000E+00 0.0000 0.0000E+00 0.0000 0.0000E+00 0.0000
7.0711E+01 7.6997E+01 5.4160E-01 0.0023 1.0583E-05 1.0000 1.8902E-03
0.0903 0.0000E+00 0.0000 0.0000E+00 0.0000 0.0000E+00 0.0000
7.6997E+01 8.3843E+01 5.0770E-01 0.0030 0.0000E+00 0.0000 1.4997E-03
0.0974 0.0000E+00 0.0000 0.0000E+00 0.0000 0.0000E+00 0.0000
8.3843E+01 9.1296E+01 4.0596E-01 0.0046 0.0000E+00 0.0000 1.2806E-03
0.1255 0.0000E+00 0.0000 0.0000E+00 0.0000 0.0000E+00 0.0000
9.1296E+01 9.9413E+01 3.6938E-01 0.0044 0.0000E+00 0.0000 8.0938E-04
0.1213 0.0000E+00 0.0000 0.0000E+00 0.0000 0.0000E+00 0.0000
9.9413E+01 1.0825E+02 3.0224E-01 0.0058 0.0000E+00 0.0000 4.9967E-04
0.1348 0.0000E+00 0.0000 0.0000E+00 0.0000 0.0000E+00 0.0000
1.0825E+02 1.1788E+02 2.1654E-01 0.0044 0.0000E+00 0.0000 3.8567E-04
0.1622 0.0000E+00 0.0000 0.0000E+00 0.0000 0.0000E+00 0.0000
1.1788E+02 1.2836E+02 1.7707E-01 0.0073 0.0000E+00 0.0000 3.4150E-04
0.2204 0.0000E+00 0.0000 0.0000E+00 0.0000 0.0000E+00 0.0000
1.2836E+02 1.3977E+02 1.3247E-01 0.0069 0.0000E+00 0.0000 1.4538E-04
0.2574 0.0000E+00 0.0000 0.0000E+00 0.0000 0.0000E+00 0.0000
1.3977E+02 1.5219E+02 9.1705E-02 0.0113 0.0000E+00 0.0000 7.7339E-05
0.4758 0.0000E+00 0.0000 0.0000E+00 0.0000 0.0000E+00 0.0000
1.5219E+02 1.6572E+02 5.6479E-02 0.0129 0.0000E+00 0.0000 2.1132E-05
0.6669 0.0000E+00 0.0000 0.0000E+00 0.0000 0.0000E+00 0.0000
1.6572E+02 1.8046E+02 3.9202E-02 0.0205 0.0000E+00 0.0000 0.0000E+00
0.0000 0.0000E+00 0.0000 0.0000E+00 0.0000 0.0000E+00 0.0000
1.8046E+02 1.9650E+02 2.5640E-02 0.0181 0.0000E+00 0.0000 4.2253E-05
0.4086 0.0000E+00 0.0000 0.0000E+00 0.0000 0.0000E+00 0.0000
1.9650E+02 2.1397E+02 1.4186E-02 0.0234 0.0000E+00 0.0000 4.2879E-05
0.4104 0.0000E+00 0.0000 0.0000E+00 0.0000 0.0000E+00 0.0000
2.1397E+02 2.3299E+02 6.4421E-03 0.0298 0.0000E+00 0.0000 1.0429E-05
1.0000 0.0000E+00 0.0000 0.0000E+00 0.0000 0.0000E+00 0.0000
2.3299E+02 2.5371E+02 3.8010E-03 0.0387 0.0000E+00 0.0000 1.1654E-05
1.0000 0.0000E+00 0.0000 0.0000E+00 0.0000 0.0000E+00 0.0000
2.5371E+02 2.7626E+02 1.8502E-03 0.0954 0.0000E+00 0.0000 0.0000E+00
0.0000 0.0000E+00 0.0000 0.0000E+00 0.0000 0.0000E+00 0.0000
2.7626E+02 3.0082E+02 8.8015E-04 0.1068 0.0000E+00 0.0000 0.0000E+00
0.0000 0.0000E+00 0.0000 0.0000E+00 0.0000 0.0000E+00 0.0000

3.0082E+02 3.2757E+02 2.2001E-04 0.2517 0.0000E+00 0.0000 0.0000E+00 0.0000 0.0000E+00 0.0000 0.0000E+00 0.0000 0.0000E+00 0.0000
3.2757E+02 3.5669E+02 1.4000E-04 0.3049 0.0000E+00 0.0000 0.0000E+00 0.0000 0.0000E+00 0.0000 0.0000E+00 0.0000 0.0000E+00 0.0000
3.5669E+02 3.8840E+02 2.0000E-05 0.6667 0.0000E+00 0.0000 0.0000E+00 0.0000 0.0000E+00 0.0000 0.0000E+00 0.0000 0.0000E+00 0.0000
3.8840E+02 4.2293E+02 2.0000E-05 0.6667 0.0000E+00 0.0000 0.0000E+00 0.0000 0.0000E+00 0.0000 0.0000E+00 0.0000 0.0000E+00 0.0000
4.2293E+02 4.6053E+02 0.0000E+00 0.0000 0.0000E+00 0.0000 0.0000E+00 0.0000 0.0000E+00 0.0000 0.0000E+00 0.0000 0.0000E+00 0.0000
4.6053E+02 5.0147E+02 1.0000E-05 1.0000 0.0000E+00 0.0000 0.0000E+00 0.0000 0.0000E+00 0.0000 0.0000E+00 0.0000 0.0000E+00 0.0000
5.0147E+02 5.4606E+02 0.0000E+00 0.0000 0.0000E+00 0.0000 0.0000E+00 0.0000 0.0000E+00 0.0000 0.0000E+00 0.0000 0.0000E+00 0.0000
5.4606E+02 5.9460E+02 0.0000E+00 0.0000 0.0000E+00 0.0000 0.0000E+00 0.0000 0.0000E+00 0.0000 0.0000E+00 0.0000 0.0000E+00 0.0000
5.9460E+02 6.4747E+02 0.0000E+00 0.0000 0.0000E+00 0.0000 0.0000E+00 0.0000 0.0000E+00 0.0000 0.0000E+00 0.0000 0.0000E+00 0.0000
6.4747E+02 7.0503E+02 0.0000E+00 0.0000 0.0000E+00 0.0000 0.0000E+00 0.0000 0.0000E+00 0.0000 0.0000E+00 0.0000 0.0000E+00 0.0000
7.0503E+02 7.6771E+02 0.0000E+00 0.0000 0.0000E+00 0.0000 0.0000E+00 0.0000 0.0000E+00 0.0000 0.0000E+00 0.0000 0.0000E+00 0.0000
7.6771E+02 8.3596E+02 0.0000E+00 0.0000 0.0000E+00 0.0000 0.0000E+00 0.0000 0.0000E+00 0.0000 0.0000E+00 0.0000 0.0000E+00 0.0000
8.3596E+02 9.1028E+02 0.0000E+00 0.0000 0.0000E+00 0.0000 0.0000E+00 0.0000 0.0000E+00 0.0000 0.0000E+00 0.0000 0.0000E+00 0.0000
9.1028E+02 9.9121E+02 0.0000E+00 0.0000 0.0000E+00 0.0000 0.0000E+00 0.0000 0.0000E+00 0.0000 0.0000E+00 0.0000 0.0000E+00 0.0000
9.9121E+02 1.0793E+03 0.0000E+00 0.0000 0.0000E+00 0.0000 0.0000E+00 0.0000 0.0000E+00 0.0000 0.0000E+00 0.0000 0.0000E+00 0.0000
1.0793E+03 1.1753E+03 0.0000E+00 0.0000 0.0000E+00 0.0000 0.0000E+00 0.0000 0.0000E+00 0.0000 0.0000E+00 0.0000 0.0000E+00 0.0000
1.1753E+03 1.2798E+03 0.0000E+00 0.0000 0.0000E+00 0.0000 0.0000E+00 0.0000 0.0000E+00 0.0000 0.0000E+00 0.0000 0.0000E+00 0.0000
1.2798E+03 1.3936E+03 0.0000E+00 0.0000 0.0000E+00 0.0000 0.0000E+00 0.0000 0.0000E+00 0.0000 0.0000E+00 0.0000 0.0000E+00 0.0000
1.3936E+03 1.5174E+03 0.0000E+00 0.0000 0.0000E+00 0.0000 0.0000E+00 0.0000 0.0000E+00 0.0000 0.0000E+00 0.0000 0.0000E+00 0.0000
1.5174E+03 1.6524E+03 0.0000E+00 0.0000 0.0000E+00 0.0000 0.0000E+00 0.0000 0.0000E+00 0.0000 0.0000E+00 0.0000 0.0000E+00 0.0000
1.6524E+03 1.7993E+03 0.0000E+00 0.0000 0.0000E+00 0.0000 0.0000E+00 0.0000 0.0000E+00 0.0000 0.0000E+00 0.0000 0.0000E+00 0.0000
1.7993E+03 1.9592E+03 0.0000E+00 0.0000 0.0000E+00 0.0000 0.0000E+00 0.0000 0.0000E+00 0.0000 0.0000E+00 0.0000 0.0000E+00 0.0000

```
  1.9592E+03   2.1334E+03   0.0000E+00  0.0000   0.0000E+00  0.0000   0.0000E+00
0.0000   0.0000E+00  0.0000   0.0000E+00  0.0000   0.0000E+00  0.0000
  2.1334E+03   2.3231E+03   0.0000E+00  0.0000   0.0000E+00  0.0000   0.0000E+00
0.0000   0.0000E+00  0.0000   0.0000E+00  0.0000   0.0000E+00  0.0000
  2.3231E+03   2.5296E+03   0.0000E+00  0.0000   0.0000E+00  0.0000   0.0000E+00
0.0000   0.0000E+00  0.0000   0.0000E+00  0.0000   0.0000E+00  0.0000
  2.5296E+03   2.7545E+03   0.0000E+00  0.0000   0.0000E+00  0.0000   0.0000E+00
0.0000   0.0000E+00  0.0000   0.0000E+00  0.0000   0.0000E+00  0.0000
  2.7545E+03   2.9994E+03   0.0000E+00  0.0000   0.0000E+00  0.0000   0.0000E+00
0.0000   0.0000E+00  0.0000   0.0000E+00  0.0000   0.0000E+00  0.0000
  2.9994E+03   3.2660E+03   0.0000E+00  0.0000   0.0000E+00  0.0000   0.0000E+00
0.0000   0.0000E+00  0.0000   0.0000E+00  0.0000   0.0000E+00  0.0000
  3.2660E+03   3.5564E+03   0.0000E+00  0.0000   0.0000E+00  0.0000   0.0000E+00
0.0000   0.0000E+00  0.0000   0.0000E+00  0.0000   0.0000E+00  0.0000
  3.5564E+03   3.8726E+03   0.0000E+00  0.0000   0.0000E+00  0.0000   0.0000E+00
0.0000   0.0000E+00  0.0000   0.0000E+00  0.0000   0.0000E+00  0.0000
  3.8726E+03   4.2169E+03   0.0000E+00  0.0000   0.0000E+00  0.0000   0.0000E+00
0.0000   0.0000E+00  0.0000   0.0000E+00  0.0000   0.0000E+00  0.0000
  4.2169E+03   4.5918E+03   0.0000E+00  0.0000   0.0000E+00  0.0000   0.0000E+00
0.0000   0.0000E+00  0.0000   0.0000E+00  0.0000   0.0000E+00  0.0000
  4.5918E+03   5.0000E+03   0.0000E+00  0.0000   0.0000E+00  0.0000   0.0000E+00
0.0000   0.0000E+00  0.0000   0.0000E+00  0.0000   0.0000E+00  0.0000

#   sum over              1.4619E+01         4.2291E-04         7.8682E-01         3.5054E-
02         0.0000E+00         0.0000E+00
'no. =    1   reg = 1 - 2'
msuc: {\huge [t-cross] in region mesh}
msdl: {\it plotted by \ANGEL \version}
msdr: {\it calculated by \PHITS  2.64}
wt: s(0.7)
\vspace{-3}
  region surface crossing
  area  &=&   1.0000E-02 [cm^2]
e:

# Information for Restart Calculation
# This calculation was newly started
# istdev =  1 # 1:Batch variance, 2:History variance
# resc2  = 1.00000000000000000E+01 # Total source weight or Total source weight /
Batch
# resc3  = 1.00000000000000000E+01 # Total history number or Total batch number
# maxcas =     1000000 # History / Batch, only used for istdev=1
# rijklst= 173130845167769.0 # Next initial random number
```

APPENDIX C. PARAMETERS AND INITIAL CONDITIONS FOR PNEUMA

Parameter	Definition	Values	Units
RPA	Pulm. arterial flow res.	0.023	mmHg * s/mL
RPP	Pulm. periph. flow res.	0.0894	mmHg * s/mL
RPV	Pulm. venous flow res.	0.0056	mmHg * s/mL
RSA	Syst. arterial flow res.	0.06	mmHg * s/mL
RSP	Splanchnic periph. flow res.	3.307	mmHg * s/mL
REP	Extra-splanchnic periph. res.	3.52	mmHg * s/mL
RMPN	Skeletal muscle periph. flow res.	4.48	mmHg * s/mL
RBPN	Cerebral periph. flow res.	6.57	mmHg * s/mL
RHPN	Coronary periph. flow res.	19.71	mmHg * s/mL
RSV	Splanchnic venous flow res.	0.038	mmHg * s/mL
REV	Extra-splanchnic venous res.	0.04	mmHg * s/mL
RMV	Skeletal muscle venous flow res.	0.05	mmHg * s/mL
RBV	Cerebral venous flow res.	0.075	mmHg * s/mL
RHV	Coronary venous flow res.	0.224	mmHg * s/mL
RVC_0	Nominal vena cava flow res.	0.025	mmHg * s/mL
RLA	Left at. flow res.	0.0025	mmHg * s/mL
RRA	Right at. flow res.	0.0025	mmHg * s/mL
CPA	Pulm. arterial compliances	0.76	mL/mmHg
CPP	Pulm. periph. compliances	5.8	mL/mmHg

CPV	Pulm. venous compliances	25.37	mL/mmHg
CSA	Syst. arterial compliances	0.28	mL/mmHg
CSP	Splanchnic periph. compliances	2.05	mL/mmHg
CEP	Extra-splanchnic periph. compliances	0.668	mL/mmHg
CMP	Skeletal muscle periph. compliances	0.525	mL/mmHg
CBP	Cerebral periph. compliances	0.358	mL/mmHg
CHP	Coronary periph. compliances	0.119	mL/mmHg
CSV	Syst. venous compliances	61.11	mL/mmHg
CEV	Extra-splanchnic venous compliances	20	mL/mmHg
CMV	Skeletal muscle venous compliances	15.71	mL/mmHg
CBV	Cerebral venous compliances	10.71	mL/mmHg
CHV	Coronary venous compliances	3.57	mL/mmHg
CLA	Left at. compliances	19.23	mL/mmHg
CRA	Right at. compliances	31.25	mL/mmHg
LPA	Pulm. arterial inertance	0.00018	mmHg * s2/mL
LSA	Syst. arterial inertance	0.00022	mmHg * s2/mL
VUPA	Pulm. arterial unstressed vol.	0	mL
VUPP	Pulm. periph. unstressed vol.	123	mL
VUPV	Pulm. venous unstressed vol.	120	mL

VUSA	Syst. arterial unstressed vol.	0	mL
VUSP	Splanchnic periph. unstressed vol.	274.4	mL
VUEP	Extra-splanchnic periph. unstressed vol.	134.64	mL
VUMP	Skeletal muscle periph. unstressed vol.	105.8	mL
VUBP	Cerebral periph. unstressed vol.	72.13	mL
VUHP	Coronary periph. unstressed vol.	24	mL
VUSV	Splanchnic venous unstressed vol.	1121	mL
VUEV	Extra-splanchnic venous unstressed vol.	550	mL
VUMV	Skeletal muscle venous unstressed vol.	432.14	mL
VUBV	Cerebral venous unstressed vol.	294.64	mL
VUHV	Coronary venous unstressed vol.	98.21	mL
VVC_0	Vena cava unstressed vol.	130	mL
VULA	Left at. unstressed vol.	25	mL
VURA	Right at. unstressed vol.	25	mL
VULV	Left vent. unstressed vol.	16.77	mL
VURV	Right vent. unstressed vol.	40.88	mL
Kr_vc	Gain for vena cava flow res.	0.001	mmHg*s/mL
Vvc_max	Maximum vol. of vena cava	350	mL
Vvc_min	Minimum vol. of vena cava	50	mL

D1	Parameter for P–V curve of vena cava	0.3855	mmHg
D2	Parameter for P–V curve of vena cava	−5	mmHg
K1_vc	Parameter for P–V curve of vena cava	0.15	mmHg
K2_vc	Parameter for P–V curve of vena cava	0.4	mmHg
Rcw	Chest wall res.	1.03	cmH2O*s/L
RLT	Lung transmural res.	1.69	cmH2O *s/L
Raw	Airway wall res.	1.016	cmH2O *s/L
Ecw	Chest wall elastance	5	cmH2O /L
ELT	Lung transmural elastance	5	cmH2O /L
k1,aw	Const. for upper airway pressure	1.85	cmH2O *s2/ L2
k2,aw	Const. for upper airway pressure	0.43	cmH2O *s2/ L2
Dead(i),co2IC	Initial cond for ith CO2 dead space	39.562	L
Dead(i),co2IC	Initial cond for ith CO2 dead space	39.674	L
Dead(i),co2IC	Initial cond for ith CO2 dead space	39.813	L
Dead(i),co2IC	Initial cond for ith CO2 dead space	40.006	L
Dead(i),o2IC	Initial cond for ith O2 dead space	104.36	L
Dead(i),o2IC	Initial cond for ith O2 dead space	104.23	L
Dead(i),o2IC	Initial cond for ith O2 dead space	104.05	L
Dead(i),o2IC	Initial cond for ith O2 dead space	103.8	L
Vd(i)	ith dead space vol. (i={1,..4}	0.03	L

PI,co2	Inspiratory CO2 partial pressure	0	Torr
PI,co2	Inspiratory O2 partial pressure	150	Torr
Vt'	Respiratory flow	variable	L/sec
Vt	Tidal Vol.	variable	L
PdO2	Dead space O2 partial pressure	variable	Torr
PdCO2	Dead space CO2 partial pressure	variable	Torr
Vco2, VLco2	Lungs storage vol. for CO2	3	L
Vo2, VLo2	Lungs storage vol. for O2	2.5	L
PAco2IC	Initial cond for Partial CO2 pressure	40.943	Torr
PAo2IC	Initial cond for Partial O2 pressure	102.52	Torr
PAo2IC	Initial cond for Partial O2 pressure	102.52	Torr
PACO2	Alveolar CO2 partial pressure	variable	Torr
PACO2	Alveolar O2 partial pressure	variable	Torr
Palv	Alveolar partial gas pressure	variable	Torr
Q	Blood flow	variable	L/sec
tauchemo	Periph. chemoreceptors delay time const.	2	s
T1	Time const. for cardiovascular mixing	1	s
T2	Time const. for cardiovascular mixing	2	s
Ta	Lung to chemoreceptor circulation delay	variable	s
LCTV0	Lung to chemoreceptor	0.588	liter

	transportation vol. const.		
PaO2firstIC	Initial cond for first order Pao2 system	0.3557	Torr
PaO2secondIC	Initial cond for second order Pao2 system	103.14	Torr
PaCO2firstIC	Initial cond for first order Paco2 system	−0.2465	Torr
PaCO2secondIC	Initial cond for second order Paco2 system	40.393	Torr
PaO2_delayIC	Initial cond for O2 convection	103.12	Torr
Paco2_delayIC	Initial cond for CO2 convection	40.445	Torr
PaCO2	CO2 partial pressure	variable	Torr
PaO2	O2 partial pressure	variable	Torr
C1	Maximum concentration of hemoglobin-bound oxygen	9	mL/mL
C2	Maximum carbon dioxide concentration	87	mL/mL
a1	Parameter in O2 dissociation equation	0.3836	dimensionless
a2	Parameter in CO2 dissociation equation	1.819	dimensionless
alpha1	Parameter in O2 dissociation equation	0.02598	dimensionless
alpha2	Parameter in CO2 dissociation equation	0.05591	dimensionless
K1	Parameter in O2 dissociation equation	13	dimensionless
K2	Parameter in CO2 dissociation equation	194.4	dimensionless
beta1	Parameter in O2 dissociation equation	0.012275	dimensionless
beta2	Parameter in CO2	0.03255	dimensionless

	dissociation equation		
Sao2_delayIC	Initial Cond for Oxygen Saturation Delay	98.92	sec
MRbco2	Metabolic prod rate for CO2 in the brain tissue	0.0517	1/s STPD
Sco2	Dissociation slope for CO2 in the blood	0.0043	mL/(mL*Torr)
Sbco2	Dissociation slope for CO2 in the brain tissue	0.36	mL*100g−1/Torr
Pbco2IC	Initial cond for partial CO2 pressure from the brain	48.538	Torr
Vtco2	Body tissue storage vol. for CO2	6	L
Vto2	Body tissue storage vol. for O2	7.7	L
MRco2	Metabolic prod rate for CO2	0.0033	1/s STPD
MRo2	Metabolic consumption rate for O2	0.0038	1/s STPD
Cvco2IC	Initial cond for mixed venous CO2 concentration	0.5247	mL/mL
Cvo2IC	Initial cond for mixed venous O2 concentration	0.1639	mL/mL
Ruaw	Upper airway wall res.	1000000	cmH2O*s/L
A0ua	Maximum area of opening in upper airway	1	a.u.
Kua	Proportionality coefficient between Aua and Yua;	1	L/(s*cmH2O)
Pcrit_awake	Critical upper airway pressure in wakefulness	−40	cmH2O
Sua	Upper airway sensitivity	0.01	a.u.

	to collapse		
Cua	Upper airway compliance	variable	L/cmH2O
Pua	Upper airway pressure	variable	cmH2O
$\dot{V}ua$	Upper airway flow	variable	cmH2O
$\dot{V}$	Total flow in airways	variable	cmH2O
FlowIC	Initial air flow	0	L/s
VC	Vital Capacity	5	L
Pt_frcIC1	Initial cond for respiratory muscle reaction	0	spikes/s
Pt_frcIC2	Initial cond for respiratory muscle reaction	0	spikes/s
FlowIC	Initial cond for airflow	0	L/s
VtIC	Initial cond for lung vol.	0	L
Pn	Center pressure for sigmoidal function	92	mmHg
Kcs	Parameter for sigmoidal slope control	11.758	mmHg
Pn_sleep	Parameter for sleep effects	0	mmHg
Kcs_sleep	Parameter for sleep effect	0	mmHg
fcs,min	Lower threshold for sigmoidal function	2.52	spikes/s
fcs,max	Upper saturation for sigmoidal function	47.78	spikes/s
τZ	Time const. for baroreflex	6.37	s
τP	Time const. for baroreflex	2.076	s
Ic	Central apneic threshold	45	dimensionless
IpCO2	Periph. apneic threshold for CO2	38	dimensionless
IpO2	Periph. apneic threshold	102.4	dimensionless

	for O2		
Gc	Gain for central chemical drive	0.075	dimensionless
Gp	Gain for periph. chemical drive	0.0063	dimensionless
Swake	Factor of wakefulness to sleep	0.3	dimensionless
Fb	Basal breathing frequency	12.5	Breath /min
Vb	Basal ventilation	6.7	L/min
TD	Chemoreflex drive threshold	1539	mL
TP	Chemoreflex drive threshold	2879	mL
S1F	Scaling factor	0.00518	dimensionless
S1V	Scaling factor	0.024	dimensionless
S2F	Scaling factor	0.0105	dimensionless
S2V	Scaling factor	0.0367	dimensionless
fchemo,max	Upper saturation for the sigmoidal function	12.3	spikes/s
fchemo,min	Lower saturation for the sigmoidal function	0.835	spikes/s
fchemo_control	Basal level for the chemoreflex	1.4	dimensionless
Kchemo	Slope control parameter for the sigmoidal function	29.27	mmHg
KH	Const. value for the static response	3	dimensionless
τchemo	Time const. for the chemoreflex	2	s
Gls	Const. gain	23.29	spikes/sec/liter
τls	Time const.	2	sec
Xsa	Saturation for the offset of α-sympathetic activity on periph. res.	6	Torr

θsan	Nominal level of offset of α-sympathetic activity on periph. res.	13.2	spikes/sec
PO2nsa	Central point for the sigmoidal function	30	Torr
kiscsa	Parameter of α-sympathetic activity on periph. res.	2	dimensionless
Xsb	Saturation for the offset of β sympathetic activity	21.2	Torr
θsbn	Nominal level of offset of β-sympathetic activity	3.6	spikes/sec
PO2nsb	Central point for the sigmoidal function	45	Torr
kiscsb	Parameter of β-sympathetic activity	4	dimensionless
Xsp	Saturation for the offset of α-sympathetic activity on periph. res.	6	dimensionless
θspn	Nominal level of offset of α-sympathetic activity on periph. res.	13.2	spikes/sec
PO2nsp	Central point for the sigmoidal function	30	Torr
kiscsp	Parameter of α-sympathetic activity on unstressed vol. of veins	2	dimensionless
τisc	Time const. for oxygen response	30	s
τcc	Time const. for carbon dioxide response	20	s
fcs,0	Center point for the sigmoidal function for parasympathetic	25	spikes/s
fpara,0	Lower saturation of the parasympathetic	3.2	spikes/s

	exponential decay function		
fpara,∞	Upper limit of the parasympathetic exponential decay function	6.3	spikes/s
kp	Slope control parameter for the sigmoidal function	7.06	dimensionless
G_RSA,p	Central RSA gain for parasympathetic response	0.4	dimensionless
Gchemo,p	Chemoreflex gain for parasympathetic response	0.03	dimensionless
Glung, p	Lung stretch receptor reflex gain for parasympathetic response	0.24	dimensionless
fs,0	Upper limit of the sympathetic exponential decay function	16.11	spikes/s
fs,∞	Lower saturation of the sympathetic exponential decay function	2.1	spikes/s
Ks	Const. for the exponential function	0.07	s
G_RSA,bs	Central RSA gain for β-sympathetic response	0.4	dimensionless
Gchemo,bs	Chemoreflex gain for β-sympathetic response	2.8	dimensionless
Glung,bs	Lung stretch receptor reflex gain for β-sympathetic	0.24	dimensionless
G_RSA,as	Central RSA gain for α-sympathetic response	0.4	dimensionless

Gchemo,as	Chemoreflex gain for α-sympathetic response	4	dimensionless
Glung,as	Lung stretch receptor reflex gain for α-sympathetic	0.34	dimensionless
ftbsIC	β-sympathetic initial output after time delay	3.8576	spikes/s
ftbs_min	Lower limit for the natural log function	2.66	spikes/s
Gbs	β-sympathetic Gain varied with sleep drive	−0.13	dimensionless
Gbs_sleep	β-sympathetic sleep gain factor	0.2	dimensionless
τbs	β-sympathetic time const.	2	s
Dbs	Delay for β-sympathetic time const.	2	s
ftpIC	Para sympathetic initial output after time delay	4.2748	spikes/s
Gpara	Parasympathetic Gain varied with sleep drive	0.09	dimensionless
Gpara_sleep	Parasympathetic sleep gain factor	0.2	dimensionless
τpara	Parasympathetic time const.	1.5	s
Dbs	Delay for parasympathetic time const.	0.2	s
Inhale	Boolean variable for inhalation	1	dimensionless
HPbasal	Basal value for HP for denervated heart	0.58	s
Glv	Elastance gain for lft. vent.	0.475	mmHg /ml/v
Dlv	Delay for elastance of lft. vent.	2	s

τlv	Time const. for elastance of lft. vent.	8	s
Emax0_lv	Basal level of maximum end-systolic elastance of lft. vent.	2.392	mmHg /ml
Grv	Elastance gain for rht. vent.	0.282	mmHg /ml/v
Drv	Delay for elastance of rht. vent.	2	s
τrv	Time const. for elastance of rht. vent.	8	s
Emax0_rv	Basal level of maximum end-systolic elastance of rht. vent.	1.412	mmHg /ml
fasIC	α-sympathetic initial output after time delay	34.793	spikes/s
fas_min	Lower limit for the natural log function	2.66	spikes/s
Gas_sleep	α-sympathetic Gain varied with sleep	0.3	dimensionless
Gas_sp	α-sympathetic Gain for splanchnic periph. res.	0.695	dimensionless
τas_sp	α-sympathetic time const.	2	s
Das_sp	Delay α-sympathetic time const.	2	s
Gas_ep	α-sympathetic Gain for extra-splanchnic periph. res.	1.94	dimensionless
τas_ep	α-sympathetic time const.	2	s
Das_ep	Delay α-sympathetic time const.	2	s
Gas_mp	α-sympathetic Gain for skeletal muscle periph. res.	2.47	dimensionless

τas_mp	α-sympathetic time const.	2	s
Das_mp	Delay α-sympathetic time const.	2	s
Vusv0	Basal level of unstressed vol. of splanchnic venous circulation	1435.4	ml
Gas_usv	α-sympathetic Gain for unstressed vol. of splanchnic venous circulation	−265.4	ml/v
τas_usv	α-sympathetic time const.	20	s
Das_usv	Delay α-sympathetic time const.	5	s
PaCO2_n	Nominal arterial CO2 partial pressure i	40	Torr
CvO2n_b	Nominal venous O2 concentration in cerebral periph. circulation	0.14	dimensionless
CvO2n_m	Nominal venous O2 concentration in skeletal muscle periph. circulation	0.155	dimensionless
CvO2n_h	Nominal venous O2 concentration in coronary periph. circulation	0.11	dimensionless
Tau_CO2	Time const. for periph. CO2 response	20	s
Tau_O2	Time const. for periph. O2 response	10	s
A	Parameter for flow regulation equation	20.9	dimensionless
B	Parameter for flow regulation equation	92.8	dimensionless
C	Parameter for flow	10570	dimensionless

	regulation equation		
GO2_b	Gain of local O2 response on cerebral vascular bed	10	dimensionless
GO2_h	Gain of local O2 response on coronary vascular bed	35	dimensionless
GO2_m	Gain of local O2 response on muscular vascular bed	30	dimensionless
A	Amplitude of the skewed sine function	20.9	dimensionless
XH	Bias of the skewed sine function for process CH	0.9	dimensionless
XL	Bias of the skewed sine function for process CL	0.15	dimensionless
αgc	Const. for sleep decaying	0.2/60	dimensionless
αrc	Rising rate of slow wave activity	0.4/60	dimensionless
αfc	Falling rate of slow wave activity	0.008/60	dimensionless
SWAo	Initial value of sleep wake activity	0.007	dimensionless